Different sliding laws on embedded interfaces using Lagrange multipliers, penalty method and Nitsche's method

Matthias Mayr

Diplomarbeit

Lehrstuhl für Numerische Mechanik
Technische Universität München
85747 Garching b. München
Matrikelnummer: 2979761

29. September 2010

Contents

Preface

The work for this diploma thesis was done during my visit to the *Duke Computational Mechanics Laboratory* at *Duke University* in Durham, NC. I thank Professor Wolfgang A. Wall, Technische Universität München, who introduced me first into the methods of computational engineering. He also managed that it was possible to visit Professor Tod A. Laursen, former Chair of the Department of Mechanical Engineering and Materials Science at Duke University, who is now the new president of Khalifa University of Science, Technology and Research, Abu Dhabi. He came up with the idea for the topic of this thesis. Previous work on modelling polycrystalline material with the extended finite element method was done by Jessica D. Sanders, who introduced me to extended finite elements and who wrote a code, my work is based upon. I also thank Professor John E. Dolbow, Duke University, for discussing my results with me. Special thanks go to Dr. Martin Hautefeuille, who spent much time on discussing my ideas after Professor Laursen left for his new position. I thank Chandrasekhar Annavarapu for answers to several little questions. Finally, I thank Alexander Popp and Christian Cyron, who both encouraged me to do my diploma thesis in a foreign country.
I also greatfully acknowledge the financial support of "Max-Weber-Programm des Freistaates Bayern" and "Prof. Dr.-Ing. Erich-Müller-Stiftung", who both funded my trip to the US and further costs.
A CD-ROM is attached at the end of this thesis, that contains the MATLAB code, some data of the numerical examples, the LaTeX-files for this thesis and the slides of the presentation, that belongs to this thesis.

1 Introduction, motivation and outline

Numerical analysis of heterogeneous structures plays a pivotal role in multiscale approaches where the scales of interest range over several orders of magnitude. In the solid mechanics and materials science community, the micromechanical modelling of polycrystalline materials is an area of long standing interest. At these length scales, plasticity phenomena at the grain boundaries have a significant influence on the macroscopic response of a material. The effect of grain boundaries is considered as the governing deformation mechanism at elevated temperatures [32] or when the grain size approaches the nanometer length scale [43] (see figure 1.1a). At the other end of the spectrum, numerical analysis of the evolution or faulting of tectonic plates also includes frictional sliding between several fault planes [34] (see figure 1.1b).

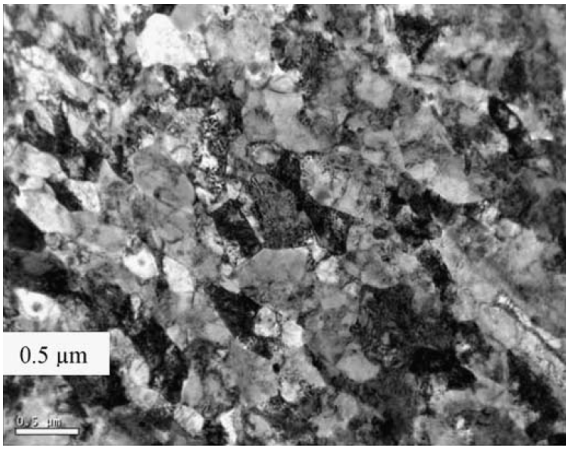

(a) Transmission electron micrograph highlighting the heterogeneous nature of polycrystalline materials at small length scales [25]

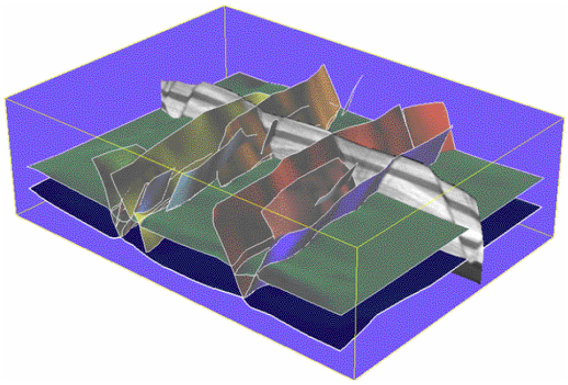

(b) Modell of faulted tectonic plates [34]

FIGURE 1.1: Two possible applications, including sliding effects along the boundaries of subdomains

Solving problems that consist of discontinuous material response is a challenging task within the classical finite element framework. To obtain optimal rates of convergence, the mesh generator has to design a mesh where the element edges or faces align themselves with the embedded lines or surfaces of discontinuity. This preprocessing step makes such investigations prohibitively expensive. The situation gets worse in a three-dimensional configuration, and there are cases, for example when grains are shaped like a wedge, in which it is not even possible to achieve the desired quality [38]. In such cases, the use of the extended finite

element method [28] or the generalized finite element method [12] with embedded interfaces suggests itself, since the mesh is independent of the topology of the subdomains with a discontinuous material response. Only a simple background mesh is needed, on which the topology of the subdomains is superimposed, as schematically depicted in figure 1.2. However, this

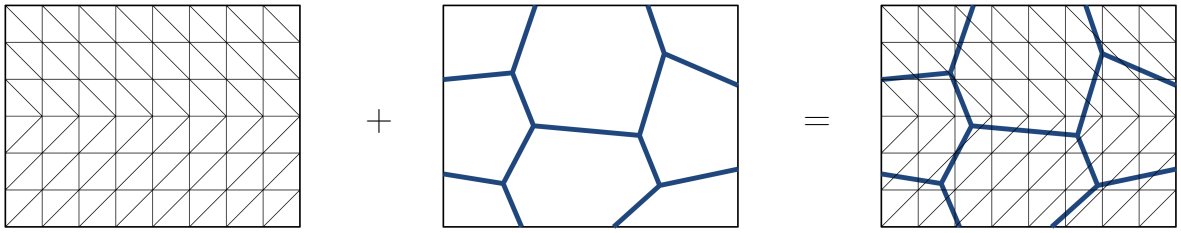

FIGURE 1.2: Background mesh with superposed subdomain topology [38]: The topology of the subdomains does not need to align with the background mesh.

added simplicity affords itself at a cost. In such an embedded approach, stable imposition of constraints on the embedded surface of discontinuity is a non-trivial task. Recently, much work has been done in this regard by several authors to address robustness issues while imposing Dirichlet-type conditions on these interfaces in an XFEM approach. In some of the early work done in this regard, imposing essential boundary conditions in the context of the extended finite element method was examined by [10, 20] where they observed that a convenient choice for the ansatz space of the Lagrange multiplier field results in severe oscillatory behavior of the traction field if the ansatz space for the Lagrange multipliers does not satisfy the *LBB-conditions*. Similar observations were made for the penalty method, where the oscillations in the traction field increase with an increasing penalty parameter [33, 37]. The lack of stability observed in the penalty method stems from its variational inconsistency. The desired result of imposing a Dirichlet constraint is only achieved in the limiting case when the penalty parameter tends to infinity. However, the discrete results suffer due to ill-conditioning of the stiffness matrix for such large values of the penalty parameter and can also be overly sensitive to the chosen value of the penalty parameter [4]. To date, the stability issues have been addressed either through a judicial reconstruction of a stable Lagrange mutiplier space [27, 5] or through a stabilized variationally consistent penalty approach [29, 8]. In this work, the focus is on the latter approach and its extension to nonlinear interfacial response. These approaches derive from the method originally proposed by Nitsche [30] to impose Dirichlet boundary conditions weakly to solve elliptic partial differential equations with the finite element method. The relationship to stabilized finite element

methods was later shown in [39], who suggests its application to contact problems, fictitious domain methods or domain decomposition techniques. The method has been used in different applications in the past ranging from frictionless sliding in contact mechanics [45, 46], embedded interface problems with scalar fields [8, 18] or with vector valued fields as in elasticity problems [33], to imposing constraints between overlapping finite element meshes [17] or to imposing boundary conditions in meshfree methods [14]. Recently, it has also been used to impose general boundary conditions [21]. To the author's best knowledge, it has never been applied to nonlinear interfacial behavior like plasticity or frictional sliding. Thus, the goal of this work is to develope a stabilized method inspired by Nitsche's method in order to enforce frictional sliding on embedded interfaces. Its performance will be compared to two classical approaches, the Lagrange multiplier method and the penalty method and its advantages will be shown.

This work is outlined as follows: In the next section, a generalized description for a problem with two grains is given. The domain and its boundaries as well as the enriched displacement field are defined. The governing equations for the bulk field are presented in the strong form. Interfacial constraints are not considered here, but they are specified for each type of constraints at the beginning of the corresponding sections. Afterwards, an untied problem, where the interface is not subjected to any kinematic constraints, is considered in order to provide the variational form and its discretization for the bulk field which is common for all other sections. In section 4, the generalized problem is specified to a problem with an perfectly bonded interface such that the two grains are kinematically fully tied and the interface is in traction equilibrium. Three methods to enforce the kinematics at the interface are illustrated, namely: Lagrange multiplier method, penalty method and Nitsche's method. For Lagrange multipliers and penalty method, well known potentials are used. The derivation of Nitsche's variational form starts with an augmented Lagrangian potential where the Lagrange multipliers are expressed in terms of the displacement field such that a Nitsche potential can be defined, directly yielding the variational problem. The discretizations are provided where the common parts from section 4 are used. Following an apporach in [8], an estimate for the stabilization parameter α in Nitsche's method for linear triangular elements is derived, which guarantees the coercivity fo the bilinear form and avoids the risk of choosing a "bad" parameter. In section 5, a problem with constraints only in normal direction is considered. There, the variational forms and their discretizations for the three methods are presented for an interface with frictionless sliding. In order to capture a more physical behaviour, a method to model perfect plasticity in tangential direction at the interface is

introduced in section 6. The constraints are enforced, using the penalty method and a stabilized method, which is inspired by Nitsche's method. The return-mapping framework is introduced. The presented methods can be easily extended to problems containig more than two grains and one interface, which is shown in section 7. Some implementational details are provided in section 8. Afterwards, numerical examples are presented in order to show the correctness of the implementation and to demonstrate some properties of the methods developed in the previous sections. The advantages of Nitsche's method and the stabilized method over the other methods are shown. Finally, some concluding remarks are given in section 10. In appendix A, an alternative derivation of Nitsche's method, following [21], is provided which starts with a penalty formulation in opposite to the one in section 4. Appendix B provides some remarks on Young's inequality which is used to derive an estimate for the stabilization parameter for Nitsche's method.

2 Problem description and governing equations in strong form for a generalized two grain problem

First, a problem description for a generalized problem with two grains is given. For illustration, a problem domain which comprises of two grains is considered. Still, the formulation can be easily generalized to account for cases with multiple grains.
The domain Ω is comprised of two subdomains, $\Omega^{(1)}$ and $\Omega^{(2)}$, called *grains*.

$$\Omega = \Omega^{(1)} \cup \Omega^{(2)} \tag{2.1}$$

The boundary of the domain Ω and the boundary of grain $\Omega^{(m)}$ is defined as follows:

$$\begin{aligned} \Gamma_{ext} &= \partial\Omega \\ \Gamma^{(m)} &= \partial\Omega^{(m)} \end{aligned} \tag{2.2}$$

Both grains, $\Omega^{(1)}$ and $\Omega^{(2)}$, share a common internal boundary Γ_*, called *interface*:

$$\Gamma_* = \Gamma^{(1)} \cap \Gamma^{(2)} \tag{2.3}$$

The problem is posed as two grains and one interface, with the possibility of different material properties in each grain $\Omega^{(m)}$, $m \in \{1,2\}$. Problems consisting of multiple grains and interfaces may be treated by looping over interfaces, each only dividing two grains, see section 7. The boundary of each grain $\Omega^{(m)}$ can potentially be divided into three separate parts: $\Gamma_d^{(m)}$, $\Gamma_\sigma^{(m)}$ and Γ_*, where $\Gamma_d^{(m)}$ denotes the Dirichlet boundary, $\Gamma_\sigma^{(m)}$ the Neumann boundary and Γ_* the part of the grain boundary, that divides the domain, Ω, into two grains, $\Omega^{(1)}$ and $\Omega^{(2)}$.

$$\Gamma^{(m)} = \Gamma_d^{(m)} \cup \Gamma_\sigma^{(m)} \cup \Gamma_* \ , \ m \in \{1,2\} \tag{2.4}$$

with

$$\Gamma_d^{(m)} \cap \Gamma_\sigma^{(m)} = \Gamma_d^{(m)} \cap \Gamma_* = \Gamma_\sigma^{(m)} \cap \Gamma_* = \emptyset \ , \ m \in \{1,2\} \tag{2.5}$$

The external boundary of the domain Ω is the combination of all Dirichlet and Neumann boundaries:

$$\Gamma_{ext} = \Gamma_d \cup \Gamma_\sigma = \Gamma_d^{(1)} \cup \Gamma_d^{(2)} \cup \Gamma_\sigma^{(1)} \cup \Gamma_\sigma^{(2)} \tag{2.6}$$

A schematic of the domain is given in figure 2.1. The unit vector $\underline{\boldsymbol{n}}^{(m)}$, that is normal to the

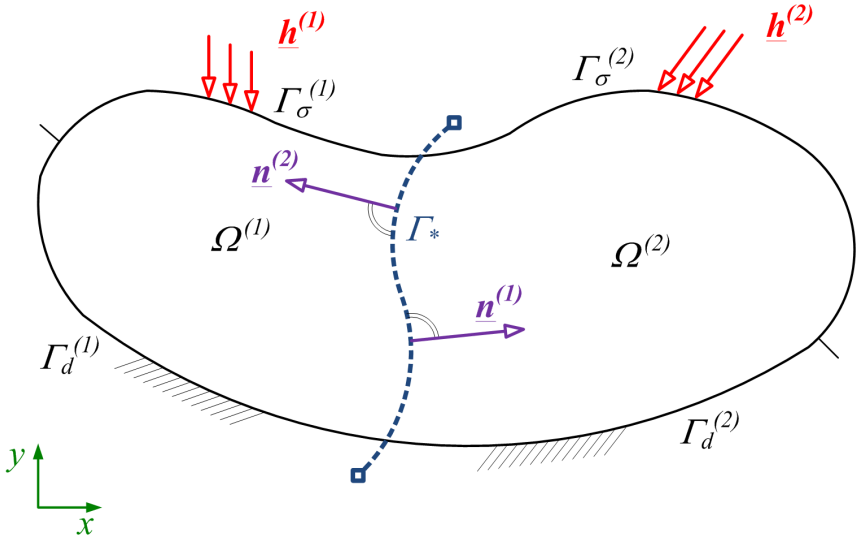

FIGURE 2.1: Domain Ω with two grains $\Omega^{(1)}$ and $\Omega^{(2)}$ divided by an embedded interface Γ_*. The domain is supported along the Dirichlet boundaries $\Gamma_d^{(1)}$ and $\Gamma_d^{(2)}$ and loaded with external tractions on the Neumann boundaries $\Gamma_\sigma^{(1)}$ and $\Gamma_\sigma^{(2)}$.

interface, is defined as positive outwards from grain $\Omega^{(m)}$. The following convention is used:

$$\underline{\boldsymbol{n}} = \underline{\boldsymbol{n}}^{(1)} = -\underline{\boldsymbol{n}}^{(2)} \tag{2.7}$$

The primary unknown is the displacement field $u_i(\boldsymbol{x})$ over Ω, which can be seen as the collection of the displacement fields $u_i^{(1)}(\underline{\boldsymbol{x}})$ and $u_i^{(2)}(\underline{\boldsymbol{x}})$ over each grain $\Omega^{(1)}$ and $\Omega^{(2)}$, where

$$u_i(\underline{\boldsymbol{x}}) = u_i^{(m)}(\underline{\boldsymbol{x}}), \text{ if } \underline{\boldsymbol{x}} \in \Omega^{(m)} \qquad \forall\, i = 1, 2 \tag{2.8}$$

The enriched finite element method, as described in [28, 33, 38] for this problem, departs from the traditional method in the assumed form of the displacement field over the body. Due to the interface Γ_* in the domain Ω, the displacement field has to be treated in a different

way compared to the classical finite element method, after a discretiztation is introduced. In order to prepare this process, it is assumed, that the displacement field can be decomposed into continuous and discontinuous parts, with the latter contributing only in the vicinity of the interface. The addition of a discontinuous function near the interface geometry allows the kinematics to properly capture the form of the solution at the interface. According to [33, 38], the displacement field near the interface is enriched and given by:

$$u_i(\underline{\boldsymbol{x}}) = \hat{u}_i(\underline{\boldsymbol{x}}) + \sum_{m=1}^{2} H^{(m)}(\underline{\boldsymbol{x}})\tilde{u}_i^{(m)}(\underline{\boldsymbol{x}}) \in \mathcal{U} \tag{2.9}$$

Its variation δu_i takes the same form:

$$\delta u_i(\underline{\boldsymbol{x}}) = \delta\hat{u}_i(\underline{\boldsymbol{x}}) + \sum_{m=1}^{2} H^{(m)}(\underline{\boldsymbol{x}})\delta\tilde{u}_i^{(m)}(\underline{\boldsymbol{x}}) \in \mathcal{V} \tag{2.10}$$

where the spaces of the displacements $\mathcal{U}$ and its variations $\mathcal{V}$ are defined as:

$$\mathcal{U} = \{u_i(\underline{\boldsymbol{x}}) | u_i(\underline{\boldsymbol{x}}) \in H^1(\Omega), u_i(\underline{\boldsymbol{x}}) = g_i \text{ on } \Gamma_d, u_i(\underline{\boldsymbol{x}}) \text{ discontinous on } \Gamma_*\} \tag{2.11}$$

$$\mathcal{V} = \{\delta u_i(\underline{\boldsymbol{x}}) | \delta u_i(\underline{\boldsymbol{x}}) \in H^1(\Omega), \delta u_i(\underline{\boldsymbol{x}}) = 0 \text{ on } \Gamma_d, \delta u_i(\underline{\boldsymbol{x}}) \text{ discontinous on } \Gamma_*\} \tag{2.12}$$

As a matter of fact, the displacement field $\hat{u}_i$ can be seen as a coarse-scale field, which is active over the entire domain Ω. The fine-scaled field $\tilde{u}_i$ is a local solution, that exists only near the interface Γ_*. Through multiplication by a characteristic grain function $H(\underline{\boldsymbol{x}})^{(m)}$, it is restricted to an individual grain $\Omega^{(m)}$, where $H(\boldsymbol{x})^{(m)}$ is defined as a Heaviside-function, that is equal to one only in grain $\Omega^{(m)}$ and zero everywhere else [33, 38]:

$$H^{(m)}(\underline{\boldsymbol{x}}) = \begin{cases} 1 & \text{if } \underline{\boldsymbol{x}} \in \Omega^{(m)} \\ 0 & \text{otherwise.} \end{cases}, \; m \in \{1,2\} \tag{2.13}$$

The expression "near the interface" is specified in detail after introducing a discretization (see remark 3.3). Individually, both $\hat{u}_i$ and $\tilde{u}_i$ belong to $H^1(\Omega)$ denoting the *Sobolev* space of functions possessing square integrable derivatives. For convenience, the argument $\underline{\boldsymbol{x}}$ is omitted in the sequel and the shorthand notations $H^{(m)}$, u_i and δu_i are introduced to indicate $H(\underline{\boldsymbol{x}})^{(m)}$, $u_i(\underline{\boldsymbol{x}})$ and $\delta u_i(\underline{\boldsymbol{x}})$, respectively. Since the problem comprises two grains $\Omega^{(m)}$, $m \in \{1,2\}$, the possible values of m will not be mentioned any more.
Using these notations, the governing equations for a small strain, elastic boundary value

problem in a small perturbation setting can be given. Thereby, indicial notation is used, where repeated indices imply a summation over these indices, according to Einstein's convention for summation. For every grain in static equilibrium, the momentum balance equation is given as

$$\sigma_{ij,j}^{(m)} + b_i^{(m)} = 0 \text{ in } \Omega^{(m)} \qquad \forall\, i,j = 1,2 \tag{2.14}$$

On the Dirichlet boundary $\Gamma_d^{(m)}$, displacements g_i are prescribed.

$$u_i^{(m)} = g_i^{(m)} \text{ on } \Gamma_d^{(m)} \tag{2.15}$$

On the Neumann boundary $\Gamma_\sigma^{(m)}$, tractions h_i are prescribed:

$$\sigma_{ij}^{(m)} n_j^{(m)} = h_i^{(m)} \text{ on } \Gamma_\sigma^{(m)} \tag{2.16}$$

where the stresses are computed via the constitutive law:

$$\sigma_{ij}^{(m)} = C_{ijkl}^{(m)} \varepsilon_{kl}^{(m)} \qquad \forall\, i,j,k,l = 1,2 \tag{2.17}$$

with the constitutive tensor $C_{ijkl}^{(m)}$ and the strain tensor $\varepsilon_{ij}^{(m)}$. Here, the material in the interior of the grains is assumed to be linear elastic. For small strains, the strains are related to the displacements by:

$$\varepsilon_{ij}^{(m)} = \frac{1}{2}\left(u_{i,j}^{(m)} + u_{j,i}^{(m)}\right) \tag{2.18}$$

According to (2.9), the strain field and its variation are defined as:

$$\begin{aligned} \varepsilon_{ij}^{(m)} &= \hat{\varepsilon}_{ij} + \sum_{m=1}^{2} H^{(m)}\ \tilde{\varepsilon}_{ij}^{(m)} \\ \delta\varepsilon_{ij}^{(m)} &= \delta\hat{\varepsilon}_{ij} + \sum_{m=1}^{2} H^{(m)} \delta\tilde{\varepsilon}_{ij}^{(m)}. \end{aligned} \tag{2.19}$$

At the internal boundary, Γ_*, the kinematics and tractions are subjected to different laws, depending on the constraints. Four different types of constraints are described in the following sections. The particular law to constrain the kinematics and tractions at the embedded interface is specified separately for each case at the beginning of the corresponding section.

A brief overwiew is given here:

- Section 3: no kinematic constraints, traction-free interface
- Section 4: perfect kinematic bond, tractions in perfect equilibrium
- Section 5: kinematics constrained only in normal direction, no tractions in tangential direction
- Section 6: perfect kinematic bond and traction equilibrium in normal direction, tangential traction limited to a yield value, corresponding tangential kinematic constraints

After introducing some notations and the governing equations for the bulk field, the different types of interfacial constraints will be put into focus.

3 The untied problem

First, an untied problem is investigated in order to derive the variational form and its discretization for the bulk field, since it leads to the common parts for all types of constraints and the three methods of constraint enforcement. After specifying the constraints for kinematics and tractions at the interface, the variational as well as the discrete form are derived. After that, all contributions from the bulk field are known and can be used for the other kinds of constraints and for all three methods of constraint enforcement.

3.1 Constraints for kinematics and tractions

For the untied problem, the embedded interface is traction free:

$$\sigma_{ij}^{(m)} n_i^{(m)} = 0 \text{ on } \Gamma_* \tag{3.1}$$

The kinematics at the interface are not constrained. Hence, a jump in the displacement field is expected after loading the domain with arbitrary tractions or prescribed displacements. The two grains might separate or penetrate each other. The displacement fields do not influence each other.

3.2 Variational form

Using the *principle of minimum of total potential energy* [19], the variational form can be derived as the first variation of the total potential energy due to the stationarity of the potential. This guarantees the symmetry of the bilinear form and hence the symmetry of the tangent stiffness matrix [19, 41]. The potential for the untied problem Π^u is computed as the sum of the internal potential Π^{int}, representing the elastic energy, and the opposite of the external potential Π^{ext}, representing the work contribution of the body forces b_i and the tractions h_i on the Neumann boundary. Π^u depends only on the displacements u_i and is given by

$$\Pi^u = \Pi^{int} - \Pi^{ext} = \frac{1}{2} \int_\Omega \varepsilon_{ij} \sigma_{ij} \, \mathrm{d}\Omega - \int_\Omega u_i b_i \, \mathrm{d}\Omega - \int_{\Gamma_\sigma} u_i h_i \, \mathrm{d}\Gamma \tag{3.2}$$

where the stress tensor σ_{ij} and the strain tensor ε_{ij} are defined in (2.17) and (2.18). The stationarity of Π^u implies that its first variation should be equal to zero:

$$\delta\Pi^u = \int_\Omega \delta\varepsilon_{ij}\sigma_{ij}\,\mathrm{d}\Omega - \int_\Omega \delta u_i b_i\,\mathrm{d}\Omega - \int_{\Gamma_\sigma} \delta u_i h_i\,\mathrm{d}\Gamma = 0 \tag{3.3}$$

Considering the enriched displacement field from (2.9), the variational problem for the untied problem reads as follows:

Find $\boldsymbol{u} \in \mathcal{U}$ for all $\delta\boldsymbol{u} \in \mathcal{V}$ such that

$$\begin{aligned}\delta\Pi^u = &\int_\Omega \delta\hat{\varepsilon}_{ij}\sigma_{ij}\,\mathrm{d}\Omega + \sum_m \int_{\Omega^{(m)}} H^{(m)}\delta\tilde{\varepsilon}_{ij}^{(m)}\sigma_{ij}^{(m)}\,\mathrm{d}\Omega \\ &- \int_\Omega \delta\hat{u}_i b_i\,\mathrm{d}\Omega - \sum_m \int_{\Omega^{(m)}} H^{(m)}\delta\tilde{u}_i^{(m)} b_i^{(m)}\,\mathrm{d}\Omega \\ &- \int_{\Gamma_\sigma} \delta\hat{u}_i h_i\,\mathrm{d}\Gamma_\sigma - \sum_m \int_{\Gamma_\sigma^{(m)}} H^{(m)}\delta\tilde{u}_i^{(m)} h_i^{(m)}\,\mathrm{d}\Gamma = 0\end{aligned} \tag{3.4}$$

Here, m is the global grain numbering index as discussed in section 2. The displacement field u_i has the same structure as indicated in (2.9). For more details on the variational form of an elastic boundary-value problem, see for example [19].

3.3 Discretization

Now, the weak form of the untied problem given in (3.4) can be discretized in order to construct a finite dimensional approximation of the problem. The discretized form yields the formulation of a residual as required for a Newton-Raphson-scheme. Although a Newton scheme is not necessary for the small perturbation problem with linear elastic material as it is considered in this section, it provides a general framework to ease the transition to plastic behavior and thus material nonlinearity at the interface (see section 6). Due to a possible nonlinear behavior, an incremental loading process, referred to as *load stepping scheme*, is applied. More details on the load stepping scheme and the nested Newton-Raphson-scheme are given in section 8.3.

In the following, discretized quantities are denoted with the superscript h. The domain is

partitioned into a set of elements:

$$\Omega = \bigcup_{e=1}^{numele} \Omega^{(e)} \tag{3.5}$$

where *numele* denotes the number of elements. This is done independently of the geometry of any internal interface. Hence, elements may be "cut" by the interface Γ_*, see figure 1.2 or figure 3.1. The interface Γ_* is divided into subsegments $\Gamma_*^{(e)}$:

$$\Gamma_* = \bigcup_{e=1}^{cutnumele} \Gamma_*^{(e)} \tag{3.6}$$

where *cutnumele* denotes the number of subsegments. A subsegment $\Gamma_*^{(e)}$ is that portion of the interface Γ_* that intersects the element e (see figure 3.2. The isoparametric concept is used. A *Bubnov-Galerkin* method is applied, so that the interpolation of the variation of the displacement field, δu_i, uses the same shape functions as the interpolation of the displacement field u_i. According to [9, 33], the displacement field, u_i, and its variation, δu_i, will be discretized in the near field of the interface, whereby the displacement field in an element is interpolated as follows:

$$\underline{\boldsymbol{u}} \approx \quad \boldsymbol{u}^h = \hat{\boldsymbol{N}} \;\; \hat{\boldsymbol{d}} + \sum_m \left(H^{(m)} \tilde{\boldsymbol{N}}^{(m)} \right) \;\; \tilde{\boldsymbol{d}} \in \mathcal{U}^h \subset \mathcal{U} \tag{3.7}$$

$$\delta\underline{\boldsymbol{u}} \approx \delta\boldsymbol{u}^h = \hat{\boldsymbol{N}} \delta\hat{\boldsymbol{d}} + \sum_m \left(H^{(m)} \tilde{\boldsymbol{N}}^{(m)} \right) \delta\tilde{\boldsymbol{d}} \in \mathcal{V}^h \subset \mathcal{V} \tag{3.8}$$

where $\hat{\boldsymbol{N}}$ and $\tilde{\boldsymbol{N}}^{(m)}$ are matrices containing usual finite element shape functions. The nodal displacements in the base and enriched degrees of freedom are denoted with $\hat{\boldsymbol{d}}$ and $\tilde{\boldsymbol{d}}$. Respectively, $\delta\hat{\boldsymbol{d}}$ and $\delta\tilde{\boldsymbol{d}}$ refer to the nodal values of the variation of the displacement field. It is common to use the same shape functions for the base and the enriched degrees of freedom:

$$N_a = \hat{N}_a = \tilde{N}_a \tag{3.9}$$

where a is the index over the nodes of an element. Still there is a difference in the matrices due to the Heaviside functions:

$$\hat{\boldsymbol{N}} = \begin{bmatrix} N_1 & 0 & N_2 & 0 & N_3 & 0 \\ 0 & N_1 & 0 & N_2 & 0 & N_3 \end{bmatrix} \tag{3.10}$$

$$\tilde{\boldsymbol{N}}^{(m)} = \begin{bmatrix} H^{(m)}N_1 & 0 & H^{(m)}N_2 & 0 & H^{(m)}N_3 & 0 \\ 0 & H^{(m)}N_1 & 0 & H^{(m)}N_2 & 0 & H^{(m)}N_3 \end{bmatrix} \tag{3.11}$$

Remark 3.1. *Since the Heaviside function $H^{(m)}$ occurs in the discretization of the displacement field as well as in the shape function matrix for the enriched degrees of freedom, it would be sufficient to drop it in the displacement field. Still, this form keeps the notation consistent with the one employed for the displacement field* (2.9).

The strain field, ε_{ij}, and its variation, $\delta\varepsilon_{ij}$, is discretized, accordingly:

$$\underline{\boldsymbol{\varepsilon}} \approx \ \boldsymbol{\varepsilon}^h = \hat{\boldsymbol{B}} \ \hat{\boldsymbol{d}} + \sum_m \left(H^{(m)} \tilde{\boldsymbol{B}}^{(m)} \right) \ \tilde{\boldsymbol{d}}, \tag{3.12}$$

$$\delta\underline{\boldsymbol{\varepsilon}} \approx \delta\boldsymbol{\varepsilon}^h = \hat{\boldsymbol{B}}\delta\hat{\boldsymbol{d}} + \sum_m \left(H^{(m)} \tilde{\boldsymbol{B}}^{(m)} \right) \delta\tilde{\boldsymbol{d}}, \tag{3.13}$$

where $\hat{\boldsymbol{B}}$ and $\tilde{\boldsymbol{B}}^{(m)}$ are matrices, containing spatial derivatives of the shape functions, where $\tilde{\boldsymbol{B}}^{(m)}$ contains also the Heaviside functions in the same manner as $\tilde{\boldsymbol{N}}^{(m)}$. For example, the scheme for numbering the degrees of freedom for a linear triangular element is given in figure 3.1.

Remark 3.2. *Here, only one set of extra degrees of freedom, $\tilde{\boldsymbol{d}}$, is introduced for all grains, whereas in [38] one set, $\tilde{\boldsymbol{d}}^{(m)}$, for each grain is used. This affects the size of the elementary quantities. Considering linear triangular elements and two grains, the element stiffness matrix in this paper has the size 12×12, whereas the size is 18×18 when using the discretization proposed in [38]. This reduction to only one set of enriched degrees of freedom is admissible since only "active" degrees of freedom have a contribution. "Inactive" degrees of freedom result in zero-contributions which only increase the size of the global system but have no influence on the solution.*

Remark 3.3. *After discretizing, the expression "near the interface", which was used to introduce the enriched displacement field, given in* (2.9)*, can now be specified in more detail: Each element, that is intersected by the interface Γ_*, is referred to as an enriched element*

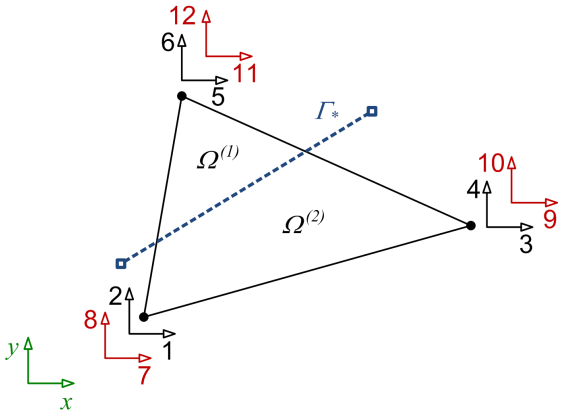

FIGURE 3.1: Numbering scheme for degrees of freedom in an enriched element [33]: The base degrees of freedom comprise numbers 1 to 6, while the enriched degrees of freedom comprise numbers 7 to 12.

and its nodes as enriched nodes. An important aspect of the method is that enrichment is only necessary for nodes whose supports are crossed by an interface [9, 28, 38]. Sufficiently far from an interface, a standard interpolation is used. Thus, the displacement and its variation in unenriched elements are discretized as in the traditional finite element method, see for example [19]. A strategy for enriching the nodes is given in [38] or [28].

Inserting the discretization of the variation of the displacement field into (3.4) leads to the discretized variational problem:

$$\begin{aligned}
&\sum_{e=1}^{numele} \left\{ \delta\hat{\boldsymbol{d}}^T \int_{\Omega^{(e)}} \hat{\boldsymbol{B}}^T \boldsymbol{\sigma}^h \,\mathrm{d}\Omega + \delta\tilde{\boldsymbol{d}}^T \sum_m \int_{\Omega^{(m),(e)}} H^{(m)} \tilde{\boldsymbol{B}}^{(m)^T} \boldsymbol{\sigma}^{h,(m)} \,\mathrm{d}\Omega \right\} \\
&- \sum_{e=1}^{numele} \left\{ \delta\hat{\boldsymbol{d}}^T \int_{\Omega^{(e)}} \hat{\boldsymbol{N}}^T \boldsymbol{b} \,\mathrm{d}\Omega + \delta\tilde{\boldsymbol{d}}^T \sum_m \int_{\Omega^{(m),(e)}} H^{(m)} \tilde{\boldsymbol{N}}^{(m)^T} \boldsymbol{b}^{(m)} \,\mathrm{d}\Omega \right\} \\
&- \sum_{e=1}^{numele} \left\{ \delta\hat{\boldsymbol{d}}^T \int_{\Gamma_\sigma^{(e)}} \hat{\boldsymbol{N}}^T \boldsymbol{h} \,\mathrm{d}\Gamma + \delta\tilde{\boldsymbol{d}}^T \sum_m \int_{\Gamma_\sigma^{(m),(e)}} H^{(m)} \tilde{\boldsymbol{N}}^{(m)^T} \boldsymbol{h}^{(m)} \,\mathrm{d}\Gamma \right\} = 0
\end{aligned} \tag{3.14}$$

with the discrete stress vector $\boldsymbol{\sigma}^h = \begin{bmatrix} \sigma_{xx}^h & \sigma_{yy}^h & \sigma_{xy}^h \end{bmatrix}^T$ in *Voigt* notation. The arbitrariness of the variations of the displacement field allows to formulate an element residual, $\boldsymbol{r}^{u,(e)}$:

$$\boldsymbol{r}^{u,(e)} = \boldsymbol{r}_b^{u,(e)} + \boldsymbol{r}_f^{u,(e)} + \boldsymbol{r}_\sigma^{u,(e)} \tag{3.15}$$

with the contributions from the bulk field, $\boldsymbol{r}_b^{u,(e)}$, the body forces, $\boldsymbol{r}_f^{u,(e)}$, and the external

tractions on the Neumann boundary, $\boldsymbol{r}_{\sigma}^{u,(e)}$:

$$\boldsymbol{r}_{b}^{u,(e)} = \begin{bmatrix} \int_{\Omega^{(e)}} \hat{\boldsymbol{B}}^{T} \boldsymbol{\sigma}^{h} \, \mathrm{d}\Omega \\ \sum_{m} \left\{ \int_{\Omega^{(m)(e)}} H^{(m)} \tilde{\boldsymbol{B}}^{(m)^{T}} \boldsymbol{\sigma}^{h,(m)} \, \mathrm{d}\Omega \right\} \end{bmatrix} \tag{3.16}$$

$$\boldsymbol{r}_{f}^{u,(e)} = - \begin{bmatrix} \int_{\Omega^{(e)}} \hat{\boldsymbol{N}}^{T} \boldsymbol{b} \, \mathrm{d}\Omega \\ \sum_{m} \left\{ \int_{\Omega^{(m)(e)}} H^{(m)} \tilde{\boldsymbol{N}}^{(m)^{T}} \boldsymbol{b}^{(m)} \, \mathrm{d}\Omega \right\} \end{bmatrix} \tag{3.17}$$

$$\boldsymbol{r}_{\sigma}^{u,(e)} = - \begin{bmatrix} \int_{\Gamma_{\sigma}^{(e)}} \hat{\boldsymbol{N}}^{T} \boldsymbol{h} \, \mathrm{d}\Gamma \\ \sum_{m} \left\{ \int_{\Gamma_{\sigma}^{(m)(e)}} H^{(m)} \tilde{\boldsymbol{N}}^{(m)^{T}} \boldsymbol{h}^{(m)} \, \mathrm{d}\Gamma \right\} \end{bmatrix} \tag{3.18}$$

$$\tag{3.19}$$

The global residual can be assembled from the element residuals:

$$\boldsymbol{R}^{u} = \bigmathop{\mathsf{A}}_{e=1}^{numele} \boldsymbol{r}^{u,(e)} \tag{3.20}$$

The global system of equations can be expressed as a residual, $\boldsymbol{R}^{u}$, that has to be equal to zero:

$$\boldsymbol{R}(\boldsymbol{D}) = \boldsymbol{R}^{u}(\boldsymbol{D}) = 0 \tag{3.21}$$

To solve this system of equations, the standard technique of a Newton-Raphson-scheme is applied.

Remark 3.4. *Actually,the residual has to be built in each Newton-Raphson-iteration in each load step, but here the indices for load steps and Newton-Raphson-iterations are omitted in order to avoid confusion through too many indices. For more details on the Newton-Raphson-scheme, see section 8.3.*

In this framework, the solution is computed in an iterative procedure where the residual, $\boldsymbol{R}$, and its linearization is required. Hence, these quantities are presented here without considering the Newton-Raphson-background in detail. Using the linearity of the assembly operator, the linearization of the global residual is computed as the assembly of the linearizations of the element residuals:

$$\Delta \boldsymbol{R} = \frac{\partial \boldsymbol{R}}{\partial \boldsymbol{D}} \Delta \boldsymbol{D} = \frac{\partial \mathsf{A}_{e=1}^{numele} \boldsymbol{r}^{u,(e)}}{\partial \boldsymbol{D}} \Delta \boldsymbol{D} = \bigmathop{\mathsf{A}}_{e=1}^{numele} \left(\frac{\partial \boldsymbol{r}^{u,(e)}}{\partial \boldsymbol{d}} \Delta \boldsymbol{d} \right) = \bigmathop{\mathsf{A}}_{e=1}^{numele} \left(\boldsymbol{k}^{u,(e)} \Delta \boldsymbol{d} \right) \tag{3.22}$$

with the element tangent stiffness matrix $\boldsymbol{k}^{u,(e)}$. The linearization of the element residual is obtained by deriving $\boldsymbol{r}^{u,(e)}$ with respect to the displacements. Since the external forces do not depend on the displacements, only the internal forces yield a contribution to the tangent stiffness matrix:

$$\Delta \boldsymbol{r}^{u,(e)} = \frac{\partial \boldsymbol{r}^{u,(e)}}{\partial \boldsymbol{d}} \Delta \boldsymbol{d} = \boldsymbol{k}^{u,(e)} \Delta \boldsymbol{d} = \begin{bmatrix} \boldsymbol{\kappa}_{11}^{u,(e)} & \boldsymbol{\kappa}_{12}^{u,(e)} \\ \boldsymbol{\kappa}_{21}^{u,(e)} & \boldsymbol{\kappa}_{22}^{u,(e)} \end{bmatrix} \begin{bmatrix} \triangle \hat{\boldsymbol{d}} \\ \triangle \tilde{\boldsymbol{d}} \end{bmatrix} \tag{3.23}$$

Using the discretization of the enriched displacement field, the element stiffness matrix, $\boldsymbol{k}^{u,(e)}$, is built with the following entries:

$$\begin{aligned} \boldsymbol{\kappa}_{11}^{u,(e)} &= \int_{\Omega^{(e)}} \hat{\boldsymbol{B}}^T \frac{\partial \boldsymbol{\sigma}^{\boldsymbol{h}}}{\partial \boldsymbol{\varepsilon}^{\boldsymbol{h}}} \hat{\boldsymbol{B}} \, \mathrm{d}\Omega \\ \boldsymbol{\kappa}_{12}^{u,(e)} &= \sum_m \left\{ \int_{\Omega^{(m)(e)}} \hat{\boldsymbol{B}}^T \frac{\partial \boldsymbol{\sigma}^{\boldsymbol{h}}}{\partial \boldsymbol{\varepsilon}^{\boldsymbol{h}}} H^{(m)} \tilde{\boldsymbol{B}}^{(m)} \, \mathrm{d}\Omega \right\} \\ \boldsymbol{\kappa}_{21}^{u,(e)} &= \sum_m \left\{ \int_{\Omega^{(m)(e)}} H^{(m)} \tilde{\boldsymbol{B}}^{(m)^T} \frac{\partial \boldsymbol{\sigma}^{\boldsymbol{h}}}{\partial \boldsymbol{\varepsilon}^{\boldsymbol{h}}} \hat{\boldsymbol{B}} \, \mathrm{d}\Omega \right\} \\ \boldsymbol{\kappa}_{22}^{u,(e)} &= \sum_m \left\{ \int_{\Omega^{(m)(e)}} H^{(m)} \tilde{\boldsymbol{B}}^{(m)^T} \frac{\partial \boldsymbol{\sigma}^{\boldsymbol{h}}}{\partial \boldsymbol{\varepsilon}^{\boldsymbol{h}}} H^{(m)} \tilde{\boldsymbol{B}}^{(m)} \, \mathrm{d}\Omega \right\} \end{aligned} \tag{3.24}$$

For the linear elastic material, the discrete constitutive matrix $\boldsymbol{C} = \frac{\partial \boldsymbol{\sigma}^{\boldsymbol{h}}}{\partial \boldsymbol{\varepsilon}^{\boldsymbol{h}}}$ is introduced.

Remark 3.5. *Since the developed code is for two-dimensional problems, a dimensional reduction is necessary. In this work, this is done by assuming a plane stress state where the constitutive matrix takes the form:*

$$\boldsymbol{C} = \frac{E}{1-\nu^2} \begin{bmatrix} 1 & \nu & 0 \\ \nu & 1 & 0 \\ 0 & 0 & \frac{1-\nu}{2} \end{bmatrix} \tag{3.25}$$

with Young's modulus E and Poisson's ratio ν as the two independent parameters to characterize the material's behavior. A mapping between the entries in C_{ijkl} and $\boldsymbol{C}$ is given in [19], for example.

Now, the global tangent stiffness matrix can be assembled:

$$\boldsymbol{K}^u = \frac{\partial \boldsymbol{R}^u}{\partial \boldsymbol{D}} = \bigwedge_{e=1}^{numele} \boldsymbol{k}^{u,(e)} \tag{3.26}$$

$\boldsymbol{K}^u$ represents the elastic stiffness of the bulk field. The residual of the bulk field and its linearization will be used in the following sections with constraints at the interface, whereby they are not repeated again.

Remark 3.6. *For elements which are intersected by a segment of the interface, the standard element quadrature routines must be modified to account for bulk terms that are active over only a portion of the domain, i.e.* $\Omega^{(1)}$ *or* $\Omega^{(2)}$*. Following [28], the integration over cut elements is split into two integrations over the two parts of an element,* $\Omega^{(e),(1)}$ *and* $\Omega^{(e),(2)}$ *(see figure 3.2). Reference [38] suggests to divide cut elements into triangular subelements and to perform the quadrature on these subelements. This is also the way it is done here.*

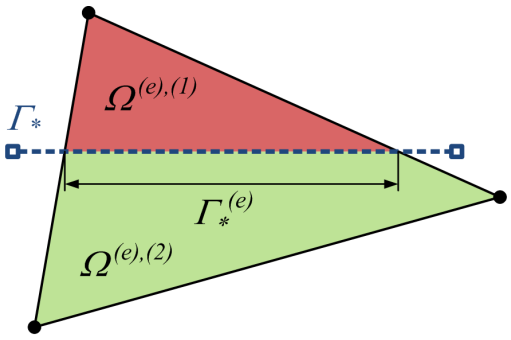

FIGURE 3.2: Integration domains for cut elements

4 The fully tied problem

After deriving the bulk field quantities using an untied problem, three methods to enforce a perfect bond and perfect traction equilibrium at the interface are introduced. Therefor, the kinematics are constrained at the internal interface Γ_* by adding terms to the variational problem (3.4). The additional terms depend on the particular method, chosen to enforce the continuity of the displacement field across the interface. Here, three methods are considered, namely: Lagrange multipliers, penalty method and Nitsche's method. The variational forms are derived as the variation of the potential Π, where Π is different for each method. Finally, the additional contributions to the discrete system are derived. These derivations are done quite extensively, because they are the basis to obtain the variational forms and their discretizations for the frictionless sliding problem presented in section 5.

4.1 Constraints for kinematics and tractions

At a fully tied interface, the two grains are connected with a perfect bond, i.e. the displacement field is perfectly continuous at the interface. The continuity of the displacement field is postulated as:

$$u_i^{(1)} = u_i^{(2)} \text{ on } \Gamma_* \tag{4.1}$$

This can be rewritten as:

$$u_i^{(1)} - u_i^{(2)} = 0 \text{ on } \Gamma_* \tag{4.2}$$

This expression will be used often in the following, so it will be referred to as *gap*-function or *jump*-function $u_i^{(1)} - u_i^{(2)}$. A shorthand notation is introduced which is often used in literature, see for example [33, 38]:

$$[\![u_i]\!] = u_i^{(1)} - u_i^{(2)} = \tilde{u}_i^{(1)} - \tilde{u}_i^{(2)} \tag{4.3}$$

This notation can be introduced for the variation of the displacement field, respectively:

$$[\![\delta u_i]\!] = \delta u_i^{(1)} - \delta u_i^{(2)} = \delta\tilde{u}_i^{(1)} - \delta\tilde{u}_i^{(2)} \tag{4.4}$$

Since the coarse background displacement field $\hat{u}_i$ is continuous at the interface, it occurs in both $u_i^{(1)}$ and $u_i^{(2)}$ and cancels out, so that only the enriched displacement field remains [33, 38]. An equivalent observation can be made for (4.4). For a fully tied problem, the constraint equation enforces the continuity of the displacement field over the interface Γ_*:

$$[\![u_i]\!] \doteq 0 \text{ on } \Gamma_* \tag{4.5}$$

Continuity is enforced in normal and tangential direction with respect to the interface Γ_*. The traction equilibrium is also satisfied:

$$\sigma_{ij}^{(1)} n_j^{(1)} = -\sigma_{ij}^{(2)} n_j^{(2)} \text{ on } \Gamma_* \tag{4.6}$$

To enforce these constraints, three different methods are used whose variational forms are derived now.

4.2 Variational forms

The variational forms for the three methods of constraint enforcement are derived. First, Lagrange multipliers are used which satisfy the continuity of the displacement field perfectly but may result in oscillations in the traction field. Then, a penalty method is considered which cannot give a perfect continuity since it is based on a regularization. Finally, Nitsche's method [30] is used, leading to a stabilized formulation.

4.2.1 Lagrange multipliers

The simplest possibility to tie the two grains together works by introducing a Lagrange multiplier field, λ_i, over the interface which can be physically interpreted as the internal tractions, h_i^*, at the interface. The starting point is the variational form representing the boundary value problem without any tractions at the internal interface as given in (3.4). Now, a Lagrange multiplier field is assumed which is represented by $\lambda_i \in \mathcal{L}$ with:

$$\mathcal{L} = \{\lambda_i(\boldsymbol{x}) | \lambda_i(\boldsymbol{x}) \in H^{-1/2}(\Gamma_*)\} \tag{4.7}$$

It acts over the embedded interface [33]. The traction field along the interface, h_i^*, is represented by the Lagrange multiplier field as follows:

$$h_i^* = -\lambda_i \tag{4.8}$$

Since the Lagrange multipliers are additional unknown variables, one has to solve for them, too. The variation of λ_i is denoted as $\delta\lambda_i$ which is also defined on $\mathcal{L}$. The additional potential of the Lagrange multiplier field, Π^{Lag}, is given as:

$$\Pi^{Lag} = \int_{\Gamma_*} \lambda_i [\![u_i]\!] \,\mathrm{d}\Gamma \tag{4.9}$$

The entire potential for the fully tied case using Lagrange multipliers to enforce the continuity of the displacement field can be written as:

$$\Pi = \Pi^u + \Pi^{Lag} = \Pi^{int} - \Pi^{ext} + \Pi^{Lag} \tag{4.10}$$

Since the variation of $\Pi^u = \Pi^{int} - \Pi^{ext}$ does not change, only the variation of Π^{Lag} is investigated here:

$$\delta\Pi^{Lag} = \int_{\Gamma_*} \lambda_i [\![\delta u_i]\!] \,\mathrm{d}\Gamma + \int_{\Gamma_*} \delta\lambda_i [\![u_i]\!] \,\mathrm{d}\Gamma \tag{4.11}$$

Using the stationarity of Π, (3.4) and (4.11) and considering the enriched displacement field, the variational problem for the fully tied problem using Lagrange multipliers reads as follows:

Find $(\boldsymbol{u}, \boldsymbol{\lambda}) \in \mathcal{U} \times \mathcal{L}$ for all $(\delta\boldsymbol{u}, \delta\boldsymbol{\lambda}) \in \mathcal{V} \times \mathcal{L}$ such that

$$\begin{aligned}
\delta\Pi = &\int_\Omega \delta\hat{\varepsilon}_{ij}\sigma_{ij} \,\mathrm{d}\Omega + \sum_m \int_{\Omega^{(m)}} H^{(m)} \delta\tilde{\varepsilon}_{ij}^{(m)} \sigma_{ij}^{(m)} \,\mathrm{d}\Omega \\
&+ \int_{\Gamma_*} \lambda_i [\![\delta u_i]\!] \,\mathrm{d}\Gamma + \int_{\Gamma_*} \delta\lambda_i [\![u_i]\!] \,\mathrm{d}\Gamma \\
&- \int_\Omega \delta\hat{u}_i b_i \,\mathrm{d}\Omega - \sum_m \int_{\Omega^{(m)}} H^{(m)} \delta\tilde{u}_i^{(m)} b_i^{(m)} \,\mathrm{d}\Omega \\
&- \int_{\Gamma_\sigma} \delta\hat{u}_i h_i \,\mathrm{d}\Gamma - \sum_m \int_{\Gamma_\sigma^{(m)}} H^{(m)} \delta\tilde{u}_i^{(m)} h_i^{(m)} \,\mathrm{d}\Gamma = 0
\end{aligned} \tag{4.12}$$

The continuity of the displacement field is enforced in a weak sense. The constraint is satisfied perfectly. According to [3], the Lagrange multiplier method can be shown to provide optimal convergence rates. Still, one major drawback of mixed methods such as the Lagrange multiplier method is, that when discretized, their performance depends on the finite element subspaces satisfying the *inf-sup conditions*. If the inf-sup conditions are not satisfied, stability problems might occur and manifest themselves as oscillations in the Lagrange multiplier field. Numerical examples in [33] show these oscillations.

4.2.2 Penalty method

To avoid the stability issues, arising with Lagrange multipliers, it is desirable to look at an alternative approach, known as the penalty method. Instead of introducing new unknowns λ_i, the penalty method approximates the Lagrange multipliers via a regularization [33]:

$$\lambda_i = -h_i^* \approx \alpha [\![u_i]\!] \tag{4.13}$$

The tractions at the interface depend on the jump in the displacement field, $[\![u_i]\!]$. The so called *penalty parameter*, α, is some large positive number which can be interpreted either as a gap stiffness or just as a mathematical tool to enforce the constraint. A graphical interpretation of a penalty regularization for a one-dimensional case is shown in figure 4.1. Sometimes, different penalty parameters for normal and tangential direction are used, espe-

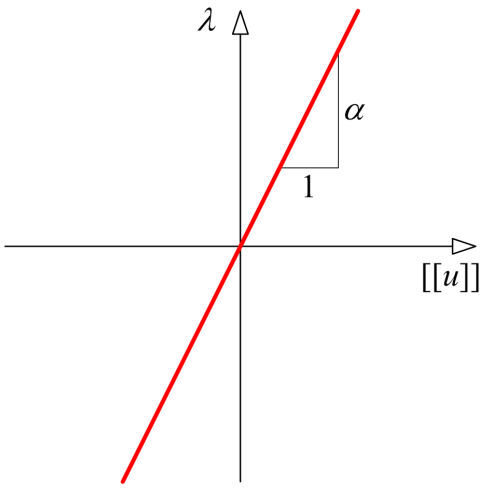

FIGURE 4.1: Penalty regularization for a one-dimensional case

cially in contact mechanics [23, 45]. This might be useful here, too, especially, when other

constitutice laws at the interface are considered. The decomposition of the traction field into a normal and a tangential part is done by using a dyadic product of the normal vector:

$$\begin{aligned} h_i^* &= h_{i,normal}^* + h_{i,tangential}^* = n_j n_i h_i^* + (\delta_{ji} - n_j n_i) h_i^* \\ &\approx -\alpha_n n_j n_i [\![u_i]\!] - \alpha_t (\delta_{ji} - n_j n_i) [\![u_i]\!] \end{aligned} \tag{4.14}$$

where α_n denotes the penalty parameter for the normal direction and α_t the one for the tangential direction. Now, it is possible to use different penalty parameters for normal and tangential direction. This will be used later on, but here — for an perfect bond and an isotropic material — it seems to make sense to use only one penalty parameter $\alpha = \alpha_n = \alpha_t$ working in all directions. It is easy to verify that (4.14) is identical with (4.13) for $\alpha = \alpha_n = \alpha_t$.

Remark 4.1. *In the following, the decomposition into normal and tangential direction is performed several times. In these cases, it is always assumed that $\alpha = \alpha_n = \alpha_t$ in order for the equality to hold. For practical computations, the penalty parameters can be chosen differently, of course.*

The penalty contribution to the potential Π is given by Π^{pen}:

$$\Pi^{pen} = \frac{1}{2} \int_{\Gamma_*} \alpha [\![u_i]\!] [\![u_i]\!] \, \mathrm{d}\Gamma \tag{4.15}$$

Since the penalty parameter α is constant, it can be pulled out of the integral. The entire potential for the fully tied case using a penalty method to enforce the continuity of the displacement field is given by:

$$\Pi = \Pi^u + \Pi^{pen} = \Pi^{int} - \Pi^{ext} + \Pi^{pen} \tag{4.16}$$

Since the variation of $\Pi^u = \Pi^{int} - \Pi^{ext}$ does not change, only the variation of Π^{pen} is investigated here. It reads:

$$\delta\Pi^{pen} = \alpha \int_{\Gamma_*} [\![\delta u_i]\!] [\![u_i]\!] \, \mathrm{d}\Gamma \tag{4.17}$$

Using the stationarity of Π, (3.4) and (4.17) as well as considering the enriched displacement field, the variational problem for the fully tied problem using the penalty method reads:

Find $\boldsymbol{u} \in \mathcal{U}$ for all $\delta\boldsymbol{u} \in \mathcal{V}$ such that

$$\begin{aligned}\delta\Pi = &\int_\Omega \delta\hat{\varepsilon}_{ij}\sigma_{ij}\,\mathrm{d}\Omega + \sum_m \int_{\Omega^{(m)}} H^{(m)}\delta\tilde{\varepsilon}_{ij}^{(m)}\sigma_{ij}^{(m)}\,\mathrm{d}\Omega + \alpha\int_{\Gamma_*}[\![\delta u_i]\!][\![u_i]\!]\,\mathrm{d}\Gamma \\ &- \int_\Omega \delta\hat{u}_i b_i\,\mathrm{d}\Omega - \sum_m \int_{\Omega^{(m)}} H^{(m)}\delta\tilde{u}_i^{(m)} b_i^{(m)}\,\mathrm{d}\Omega \\ &- \int_{\Gamma_\sigma} \delta\hat{u}_i h_i\,\mathrm{d}\Gamma - \sum_m \int_{\Gamma_\sigma^{(m)}} H^{(m)}\delta\tilde{u}_i^{(m)} h_i^{(m)}\,\mathrm{d}\Gamma = 0\end{aligned} \tag{4.18}$$

Considering the possible decomposition into normal and tangential direction (4.14) leads to the following variational problem which has the same meaning as (4.18) but uses a different notation:

Find $\boldsymbol{u} \in \mathcal{U}$ for all $\delta\boldsymbol{u} \in \mathcal{V}$ such that

$$\begin{aligned}\delta\Pi = &\int_\Omega \delta\hat{\varepsilon}_{ij}\sigma_{ij}\,\mathrm{d}\Omega + \sum_m \int_{\Omega^{(m)}} H^{(m)}\delta\tilde{\varepsilon}_{ij}^{(m)}\sigma_{ij}^{(m)}\,\mathrm{d}\Omega \\ &+ \alpha_n\int_{\Gamma_*}[\![\delta u_i]\!] n_i n_j [\![u_j]\!]\,\mathrm{d}\Gamma + \alpha_t\int_{\Gamma_*}[\![\delta u_i]\!]\left(\delta_{ij} - n_i n_j\right)[\![u_j]\!]\,\mathrm{d}\Gamma \\ &- \int_\Omega \delta\hat{u}_i b_i\,\mathrm{d}\Omega - \sum_m \int_{\Omega^{(m)}} H^{(m)}\delta\tilde{u}_i^{(m)} b_i^{(m)}\,\mathrm{d}\Omega \\ &- \int_{\Gamma_\sigma} \delta\hat{u}_i h_i\,\mathrm{d}\Gamma - \sum_m \int_{\Gamma_\sigma^{(m)}} H^{(m)}\delta\tilde{u}_i^{(m)} h_i^{(m)}\,\mathrm{d}\Gamma = 0\end{aligned} \tag{4.19}$$

Of course, this split form has the same meaning as (4.18), but it helps preparing interfacial laws with different behaviour in normal and tangential direction.

The advantage of the penalty method is that no additional unknowns are introduced, since the traction field is regularized with the jump, $[\![u_i]\!]$. The traction field can thus be reconstructed from the displacement solution, using the regularization (4.13) or using (4.14). However, the usual problems of this method cannot be neglected. Some of them will be mentioned here without claiming completeness. The penalty method can be shown as variationally inconsistent (see appendix A or [20]). Due to the regularization, the condition of the continuity of the displacement field at the interface as postulated in (4.5) will always

be violated for finite penalty parameters since the internal traction is propotional to the gap, $[\![u_i]\!]$. The magnitude of this violation depends on the magnitude of the penalty parameter. The higher the penalty parameter is chosen, the less the violation will be. The continuity condition is only perfectly represented as the penalty parameter $\alpha \to \infty$, which is practically impossible in real calculations for several reasons [23]. The most important one is, that a very high penalty parameter results in an ill-conditioned system [23, 45]. Indeed, a very high penalty parameter reduces the gap and hence raises accuracy in the displacement field, but can lead to stability problems. Hence, there is always a trade-off between accuracy and stability. According to [4], the discrete results can be overly sensitive to α.

4.2.3 Nitsche's method

It can be shown, that the Lagrange multiplier method can cause stability problems, depending on the particular choice of the discrete ansatz spaces. The penalty method is variationally inconsistent [20]. Numerical examples showing these stability problems as oscillations in the traction field are given in [33] for the fully tied problem. Hence, an alternative method without these issues is desired.

An alternative method to impose Dirichlet boundary conditions was developed in [30]. [39] shows its consistency as well as stability and recommends it to enforce constraints at interfaces, since it does not have to deal with the stability problems of the other two methods. Since it can be derived by starting with a penalty fomulation, it can be seen as a consistent form of the penalty method [11, 20]. In contrast to the standard penalty method, good convergence behavior can be obtained using a relatively small stabilization parameter [11]. In fact, the original contribution [30] proved that the discrete solution converges towards the exact solution with optimal convergence rates in the error of the displacement field as of the traction field as well, if the parameter α is chosen properly and scaled by $1/h$ with mesh refinement [1]. For a mathematical analysis of Nitsche's method, see [21, 39]. A derivation of Nitsche's method, following [21] and starting with a penalty formulation, is presented in appendix A.

However, here Nitsche's method will be derived starting with an augmented Lagrangian formulation, as suggested by [46] for frictionless contact. Therefor, the distinction between the two displacement fields, $u_i^{(1)}$ and $u_i^{(2)}$, in the two grains, $\Omega^{(1)}$ and $\Omega^{(2)}$, is made since it makes it more obvious. The convention on the normal vectors in (2.7) is recalled, which establishes the opposite signs of the normal vectors $\underline{\boldsymbol{n}}^{(1)}$ and $\underline{\boldsymbol{n}}^{(2)}$. Green's first identity is applied to the first variation of the augmented Lagrangian. The resulting expression is used to write

the Lagrange multipliers in terms of the primal variable, u_i. Finally, a one-field potential is obtained which directly yields Nitsche's variational form.
The augmented Lagrangian potential, Π^{AL}, is introduced as follows:

$$\Pi^{AL} = \int_{\Gamma_*} \left(\lambda_i + \frac{\alpha}{2}[\![u_i]\!]\right) [\![u_i]\!] \,\mathrm{d}\Gamma \tag{4.20}$$

with α being the penalty parameter and λ_i denoting the Lagrange multiplier, defined on $\mathcal{L}$ from (4.7) as well as its variation $\delta\lambda_i$. The entire potential Π is computed as the sum of the potential for the untied problem, Π^u, and the augmented Lagrangian potential, Π^{AL}:

$$\Pi = \frac{1}{2}\int_\Omega \sigma_{ij}\varepsilon_{ij} \,\mathrm{d}\Omega - \int_\Omega b_i u_i \,\mathrm{d}\Omega - \int_{\Gamma_\sigma} h_i u_i \,\mathrm{d}\Gamma + \int_{\Gamma_*} \left(\lambda_i + \frac{\alpha}{2}[\![u_i]\!]\right) [\![u_i]\!] \,\mathrm{d}\Gamma \tag{4.21}$$

The stationarity of Π imposes that its first variation should be equal to zero. This leads to the following variational problem for an augmented Lagrangian method:

Find $(\boldsymbol{u}, \boldsymbol{\lambda}) \in \mathcal{U} \times \mathcal{L}$ for all $(\delta\boldsymbol{u}, \delta\boldsymbol{\lambda}) \in \mathcal{V} \times \mathcal{L}$ such that

$$\begin{aligned} \delta\Pi = &\int_\Omega \delta\varepsilon_{ij}\sigma_{ij} \,\mathrm{d}\Omega - \int_\Omega \delta u_i b_i \,\mathrm{d}\Omega - \int_{\Gamma_\sigma} \delta u_i h_i \,\mathrm{d}\Gamma \\ &+ \int_{\Gamma_*} (\lambda_i + \alpha[\![u_i]\!]) [\![\delta u_i]\!] \,\mathrm{d}\Gamma + \int_{\Gamma_*} \delta\lambda_i [\![u_i]\!] \,\mathrm{d}\Gamma = 0 \end{aligned} \tag{4.22}$$

Since the augmented Lagrangian formulation contains two fields of unknowns, u_i and λ_i, the next step is to express the Lagrange multipliers in terms of displacements. Therefor, Green's first identity is applied to the first variation of the internal potential, $\delta\Pi^{int}$. Using the symmetry of the stress tensor, $\sigma_{ij} = \sigma_{ji}$, the first variation of the internal potential reads:

$$\begin{aligned} \int_{\Omega^{(m)}} \delta\varepsilon_{ij}^{(m)}\sigma_{ij}^{(m)} \,\mathrm{d}\Omega = &\int_{\Gamma_\sigma^{(m)}} \delta u_i^{(m)}\sigma_{ij}^{(m)} n_j^{(m)} \,\mathrm{d}\Gamma + \int_{\Gamma_*} \delta u_i^{(m)}\sigma_{ij}^{(m)} n_j^{(m)} \,\mathrm{d}\Gamma \\ &- \int_{\Omega^{(m)}} \delta u_i^{(m)}\sigma_{ij,j}^{(m)} \mathrm{d}\Omega \end{aligned} \tag{4.23}$$

The boundary integral is split into three integrals over $\Gamma_d^{(m)}$, $\Gamma_\sigma^{(m)}$ and Γ_*. Since $\delta u_i^{(m)}$ belongs to $\mathcal{V}$, the integrals over the Dirichlet boundaries vanish. Replacing (4.23) in the first variation

of Π yields:

$$\begin{aligned}\delta\Pi = &\sum_{m=1}^{2}\int_{\Gamma_\sigma^{(m)}} \delta u_i^{(m)}\left(\sigma_{ij}^{(m)} n_j^{(m)} - h_i^{(m)}\right)\mathrm{d}\Gamma - \sum_{m=1}^{2}\int_{\Omega^{(m)}} \delta u_i^{(m)}\left(b_i^{(m)} + \sigma_{ij,j}^{(m)}\right)\mathrm{d}\Omega \\ &+ \int_{\Gamma_*} \delta u_i^{(1)}\left(\sigma_{ij}^{(1)} n_j^{(1)} + \lambda_i + \alpha[\![u_i]\!]\right) + \delta u_i^{(2)}\left(\sigma_{ij}^{(2)} n_j^{(2)} - \lambda_i - \alpha[\![u_i]\!]\right) + \delta\lambda_i[\![u_i]\!]\,\mathrm{d}\Gamma\end{aligned} \tag{4.24}$$

Due to the Cauchy principle, the first term in (4.24) vanishes along with the second one due to the balance of linear momentum. Since $\delta u_i^{(m)}$ and $\delta\lambda_i$ can be chosen arbitrarily, it falls that

$$[\![u_i]\!] = 0 \text{ on } \Gamma_* \tag{4.25}$$

and thus that:

$$\lambda_i = -\sigma_{ij}^{(1)} n_j^{(1)} = -\sigma_{ij}^{(1)} n_j \tag{4.26}$$

$$\lambda_i = +\sigma_{ij}^{(2)} n_j^{(2)} = -\sigma_{ij}^{(2)} n_j \tag{4.27}$$

Adding (4.26) and (4.27) leads to the following expression for λ_i:

$$\lambda_i = -\frac{1}{2}\sum_{m=1}^{2}\sigma_{ij}^{(m)} n_j = -\langle\sigma_{ij}\rangle n_j \tag{4.28}$$

where $\langle\sigma_{ij}\rangle$ is introduced as the averaged stress over the embedded interface:

$$\langle\sigma_{ij}\rangle = \frac{\sigma_{ij}^{(1)} + \sigma_{ij}^{(2)}}{2} \tag{4.29}$$

By replacing λ_i in the augmented Lagrangian potential, Π^{AL}, with (4.28), a Nitsche potential, Π^{Nit}, which depends only on the displacement field, can be expressed as:

$$\Pi^{Nit} = \int_{\Gamma_*}\left(-\langle\sigma(\boldsymbol{u})_{ij}\rangle n_j + \frac{\alpha}{2}[\![u_i]\!]\right)[\![u_i]\!]\,\mathrm{d}\Gamma \tag{4.30}$$

The quadratic functional introduced in the original contribution [30] can be written as:

$$\Pi = \Pi^{int} - \Pi^{ext} - \int_{\Gamma_*}[\![u_i]\!]\langle\sigma(\boldsymbol{u})_{ij}\rangle n_j\,\mathrm{d}\Gamma + \frac{\alpha}{2}\int_{\Gamma_*}[\![u_i]\!]^2\,\mathrm{d}\Gamma \tag{4.31}$$

Using the stationarity of Π yields:

$$\begin{aligned}\delta\Pi = &\sum_{m=1}^{2}\int_{\Omega^{(m)}}\delta\varepsilon_{ij}^{(m)}\sigma_{ij}^{(m)}\,\mathrm{d}\Omega - \sum_{m=1}^{2}\left(\int_{\Omega^{(m)}}\delta u_i^{(m)}b_i^{(m)}\,\mathrm{d}\Omega + \int_{\Gamma_\sigma^{(m)}}\delta u_i^{(m)}h_i^{(m)}\,\mathrm{d}\Gamma\right)\\ &+\alpha\int_{\Gamma_*}[\![\delta u_i]\!][\![u_i]\!]\,\mathrm{d}\Gamma - \int_{\Gamma_*}\langle\sigma(\boldsymbol{u})_{ij}\rangle n_j[\![\delta u_i]\!]\,\mathrm{d}\Gamma - \int_{\Gamma_*}\langle\sigma(\delta\boldsymbol{u})_{ij}\rangle n_j[\![u_i]\!]\,\mathrm{d}\Gamma = 0\end{aligned} \tag{4.32}$$

Using the enriched displacement field from (2.9), the variational problem for Nitsche's method applied to the fully tied problem can be posed as follows:

Find $\boldsymbol{u}\in\mathcal{U}$ for all $\delta\boldsymbol{u}\in\mathcal{V}$ such that

$$\begin{aligned}\delta\Pi = &\int_\Omega\delta\hat{\varepsilon}_{ij}\sigma_{ij}\,\mathrm{d}\Omega + \sum_m\int_{\Omega^{(m)}}H^{(m)}\delta\tilde{\varepsilon}_{ij}^{(m)}\sigma_{ij}^{(m)}\,\mathrm{d}\Omega + \alpha\int_{\Gamma_*}[\![\delta u_i]\!][\![u_i]\!]\,\mathrm{d}\Gamma\\ &-\int_{\Gamma_*}[\![\delta u_i]\!]\langle\sigma(\boldsymbol{u})_{ij}\rangle n_j\,\mathrm{d}\Gamma - \int_{\Gamma_*}[\![u_i]\!]\langle\sigma(\delta\boldsymbol{u})_{ij}\rangle n_j\,\mathrm{d}\Gamma\\ &-\int_\Omega\delta\hat{u}_i b_i\,\mathrm{d}\Omega - \sum_m\int_{\Omega^{(m)}}H^{(m)}\delta\tilde{u}_i^{(m)}b_i^{(m)}\,\mathrm{d}\Omega\\ &-\int_{\Gamma_\sigma}\delta\hat{u}_i h_i\,\mathrm{d}\Gamma - \sum_m\int_{\Gamma_\sigma^{(m)}}H^{(m)}\delta\tilde{u}_i^{(m)}h_i^{(m)}\,\mathrm{d}\Gamma = 0\end{aligned} \tag{4.33}$$

The fourth term guarantees the consistency of the method. Symmetry is provided by the fifth term. As in the penalty method, α is a free parameter for Nitsche's method. Rather than a penalty parameter, however, it is more properly viewed as a *stabilization parameter* in the context of Nitsche's method. As such, it is expected to be relatively "small", but it should be noted, that for arbitrary values of α there is no guarantee, that the bilinear form will remain coercive. This may be important, since the coercivity of the bilinear form guarantees the positive definiteness of the stiffness matrix. However, the patch test can be passed with an arbitrary choice of $\alpha \geq 0$ [33]. It has been shown in the original contribution [30], that a minimum α_{min} exists, that guarantees the coercivity of the bilinear form associated with Nitsche's method. A method to estimate the minimal stabilization parameter which guarantees the coercivity using linear triangular elements to solve scalar problems is proposed in [8]. Using a similar idea, an estimate for α for linear triangular elements to solve two-dimensional elasticity problems is derived after discretizing Nitsche's variational form in section 4.3.3. For higher order shape functions, a local eigenvalue problem

has to be solved which is explained in detail in [33] and references therein. Similar to the penalty case, the interfacial contributions can be decomposed into normal and tangential direction using the dyadic product $n_i n_j$ which leads to the following variational problem:

Find $\boldsymbol{u} \in \mathcal{U}$ for all $\delta\boldsymbol{u} \in \mathcal{V}$ such that

$$\begin{aligned}
\delta\Pi = &\int_\Omega \delta\hat{\varepsilon}_{ij}\sigma_{ij}\,\mathrm{d}\Omega + \sum_m \int_{\Omega^{(m)}} H^{(m)}\delta\tilde{\varepsilon}_{ij}^{(m)}\sigma_{ij}^{(m)}\,\mathrm{d}\Omega \\
&+ \alpha_n \int_{\Gamma_*} [\![\delta u_i]\!] n_i n_j [\![u_j]\!]\,\mathrm{d}\Gamma + \alpha_t \int_{\Gamma_*} [\![\delta u_i]\!]\left(\delta_{ij} - n_i n_j\right)[\![u_j]\!]\,\mathrm{d}\Gamma \\
&- \int_{\Gamma_*} [\![\delta u_i]\!] n_i n_j \langle\sigma(\boldsymbol{u})_{jk}\rangle n_k\,\mathrm{d}\Gamma - \int_{\Gamma_*} [\![\delta u_i]\!]\left(\delta_{ij} - n_i n_j\right)\langle\sigma(\boldsymbol{u})_{jk}\rangle n_k\,\mathrm{d}\Gamma \\
&- \int_{\Gamma_*} [\![u_i]\!] n_i n_j \langle\sigma(\delta\boldsymbol{u})_{jk}\rangle n_k\,\mathrm{d}\Gamma - \int_{\Gamma_*} [\![u_i]\!]\left(\delta_{ij} - n_i n_j\right)\langle\sigma(\delta\boldsymbol{u})_{jk}\rangle n_k\,\mathrm{d}\Gamma \\
&- \int_\Omega \delta\hat{u}_i b_i\,\mathrm{d}\Omega - \sum_m \int_{\Omega^{(m)}} H^{(m)}\delta\tilde{u}_i^{(m)} b_i^{(m)}\,\mathrm{d}\Omega \\
&- \int_{\Gamma_\sigma} \delta\hat{u}_i h_i\,\mathrm{d}\Gamma - \sum_m \int_{\Gamma_\sigma^{(m)}} H^{(m)}\delta\tilde{u}_i^{(m)} h_i^{(m)}\,\mathrm{d}\Gamma = 0
\end{aligned} \tag{4.34}$$

Of course, this form has the same meaning as (4.33), but it helps preparing interfacial laws with different behavior in normal and tangential direction.
Considering the similarities between Nitsche's method and an augmented Lagrangian formulation, it suggests itself to compute the traction field along the interface as follows:

$$h_i^* = -\alpha[\![u_i]\!] + \langle\sigma_{ij}\rangle n_j \tag{4.35}$$

The contribution from the jump in the displacement field is expected to be very small.

Remark 4.2. *The choice of the signs in* (4.35) *can easily be verified by considering, that Nitsche's method enforces the jump to be zero. Then* (4.35) *corresponds to Cauchy's principle* $\sigma_{ij}n_j = h_i^*$.

4.3 Discretization

Now, these variational forms can be discretized. This leads to the discrete systems of equations that have to be solved. Since the common part has been presented in section 3, here

only the additional terms due to the constraint enforcement are considered.
Since the jump in the dispacement field and in its variation appears quite often, the discretization of the jump will be shown here, since it is common to all three methods of constraint enforcement. Introducing the discretization (3.7) into the definition of the jump (4.3) leads to:

$$[\![\boldsymbol{u}]\!] \approx [\![\boldsymbol{u}^h]\!] = \left(\tilde{\boldsymbol{N}}^{(1)} - \tilde{\boldsymbol{N}}^{(2)}\right) \tilde{\boldsymbol{d}} = [\![\tilde{\boldsymbol{N}}]\!]\tilde{\boldsymbol{d}} \tag{4.36}$$

with $[\![\tilde{\boldsymbol{N}}]\!]$ denoting the jump in shape functions. The jump in the variation of the displacement field is discretized, accordingly:

$$[\![\delta\boldsymbol{u}]\!] \approx [\![\delta\boldsymbol{u}^h]\!] = \left(\tilde{\boldsymbol{N}}^{(1)} - \tilde{\boldsymbol{N}}^{(2)}\right) \delta\tilde{\boldsymbol{d}} = [\![\tilde{\boldsymbol{N}}]\!]\delta\tilde{\boldsymbol{d}} \tag{4.37}$$

Using these shorthand notations, the discrete forms for Lagrange multipliers, penalty method and Nitsche's method can be introduced.

4.3.1 Lagrange multipliers

In order to implement Lagrange multipliers, a choice for the interpolation of the multipliers over the interface has to be made. In this study, the Lagrange multipliers are assumed to be piecewise constant over each $\Gamma_*^{(e)}$ since it is based on [33]. The choice of a piecewise constant subspace is convenient and easy to implement, but is shown to have stability problems [20, 33]. Recent work by [27] or even more recent by [5] demonstrates, that a careful construction of the multiplier space can circumvent the stability problems, introduced by a naive choice of multipliers. The discretization of the Lagrange multipliers λ_i and its variation $\delta\lambda_i$ is achieved via

$$\underline{\boldsymbol{\lambda}} \approx \ \boldsymbol{\lambda}^h = \bar{\boldsymbol{N}} \ \bar{\boldsymbol{\lambda}} \tag{4.38}$$

$$\delta\underline{\boldsymbol{\lambda}} \approx \delta\boldsymbol{\lambda}^h = \bar{\boldsymbol{N}}\delta\bar{\boldsymbol{\lambda}} \tag{4.39}$$

where $\bar{\boldsymbol{N}}$ contains the Lagrange multiplier shape functions which are equal to 1 over the segment k and 0 over all other segments, and k is an index over the segments $\Gamma_*^{(e)}$. $\bar{\boldsymbol{N}}$ has the following structure:

$$\bar{\boldsymbol{N}} = \begin{bmatrix} \bar{N}_k & 0 \\ 0 & \bar{N}_k \end{bmatrix} \tag{4.40}$$

Since the contributions from the bulk field as developed in section 3 do not change, only the additional parts due to the variation of Π^{Lag} have to be investigated. Inserting the discretizations (3.8) and (4.39) into the variation of Π^{Lag} (4.11) yields the discrete form of the Lagrange multiplier contribution:

$$\delta\Pi^{Lag} \approx \sum_{e=1}^{cutnumele} \left\{ \delta\tilde{\boldsymbol{d}}^T \int_{\Gamma_*^{(e)}} [\![\tilde{\boldsymbol{N}}]\!]^T \boldsymbol{\lambda}^h \, \mathrm{d}\Gamma + \delta\bar{\boldsymbol{\lambda}}^T \int_{\Gamma_*^{(e)}} \bar{\boldsymbol{N}}^T [\![\boldsymbol{u}^h]\!] \, \mathrm{d}\Gamma \right\} \tag{4.41}$$

Using the arbitrariness of the nodal variation quantities, $\delta\tilde{\boldsymbol{d}}$ and $\delta\bar{\boldsymbol{\lambda}}$, leads to a Lagrange multiplier contribution to the elementary residual,

$$\boldsymbol{r}^{Lag,(e)} = \begin{bmatrix} \boldsymbol{0}_{6\times 1} \\ \int_{\Gamma_*^{(e)}} [\![\tilde{\boldsymbol{N}}]\!]^T \boldsymbol{\lambda}^h \, \mathrm{d}\Gamma \\ \int_{\Gamma_*^{(e)}} \bar{\boldsymbol{N}}^T [\![\boldsymbol{u}^h]\!] \, \mathrm{d}\Gamma \end{bmatrix} \tag{4.42}$$

which have to be assembled to a global contribution for Lagrange multipliers to the global residual

$$\boldsymbol{R}^{Lag} = \bigwedge_{e=1}^{cutnumele} \boldsymbol{r}^{Lag,(e)} \tag{4.43}$$

such that the global system of equations becomes

$$\boldsymbol{R} = \begin{bmatrix} \boldsymbol{R}^u \\ \boldsymbol{0} \end{bmatrix} + \boldsymbol{R}^{Lag} = 0 \tag{4.44}$$

whereby the residual from the untied case has to be extended with $2 \times cutnumele$ zeros in order to obtain equal dimensions. These additional rows in the residual correspond to the additional primary unknowns, the Lagrange multipliers, with the factor 2 stemming from the two dimensions of the problem.
Since the global residual, $\boldsymbol{R}$, depends on two fields of unknowns, the linearization has to be done with respect to these two fields.

$$\Delta\boldsymbol{R} = \begin{bmatrix} \frac{\partial \boldsymbol{R}}{\partial \boldsymbol{D}} \\ \frac{\partial \boldsymbol{R}}{\partial \boldsymbol{\Lambda}} \end{bmatrix} \begin{bmatrix} \Delta\boldsymbol{D} \\ \Delta\boldsymbol{\Lambda} \end{bmatrix} \tag{4.45}$$

Due to the linearity of the assembly operator, it is sufficient to linearize the elmentary residuals in order to obtain element contributions which can be assembled to the global tangent stiffness matrix.

$$\Delta \boldsymbol{r}^{(e)} = \begin{bmatrix} \frac{\partial \boldsymbol{r}^{(e)}}{\partial \boldsymbol{d}} \\ \frac{\partial \boldsymbol{r}^{(e)}}{\partial \boldsymbol{\lambda}} \end{bmatrix} \begin{bmatrix} \Delta \boldsymbol{d} \\ \Delta \boldsymbol{\lambda} \end{bmatrix} = \begin{bmatrix} \boldsymbol{k}^{u,(e)} & \boldsymbol{g}^{\lambda,(e)} \\ \boldsymbol{g}^{d,(e)} & \boldsymbol{0} \end{bmatrix} \begin{bmatrix} \Delta \boldsymbol{d} \\ \Delta \boldsymbol{\lambda} \end{bmatrix} \tag{4.46}$$

with

$$\begin{aligned} \boldsymbol{g}^{\lambda,(e)} &= \int_{\Gamma_*^{(e)}} [\![\tilde{\boldsymbol{N}}]\!]^T \bar{\boldsymbol{N}} \, \mathrm{d}\Gamma \\ \boldsymbol{g}^{d,(e)} &= \int_{\Gamma_*^{(e)}} \bar{\boldsymbol{N}}^T [\![\tilde{\boldsymbol{N}}]\!] \, \mathrm{d}\Gamma \end{aligned} \tag{4.47}$$

where $\boldsymbol{g}^{d,(e)} = \boldsymbol{g}^{\lambda,(e)^T}$ provides the symmetry of the stiffness matrix. The global tangent stiffness matrix for Lagrange multipliers has a similar structure:

$$\begin{bmatrix} \frac{\partial \boldsymbol{R}}{\partial \boldsymbol{D}} \\ \frac{\partial \boldsymbol{R}}{\partial \boldsymbol{\Lambda}} \end{bmatrix} = \begin{bmatrix} \boldsymbol{K}^u & \boldsymbol{G}^T \\ \boldsymbol{G} & \boldsymbol{0} \end{bmatrix} = \mathop{\mathsf{A}}_{e=1}^{numele} \begin{bmatrix} \boldsymbol{k}^{u,(e)} & \boldsymbol{g}^{\lambda,(e)} \\ \boldsymbol{g}^{d,(e)} & \boldsymbol{0} \end{bmatrix} \tag{4.48}$$

Here, the submatrix $\boldsymbol{K}^u$ represents the stiffness contributions from the bulk field, adopted from the untied problem. The coupling with Lagrange multipliers is done by the submatrix $\boldsymbol{G}$ which occurs twice and is assembled from the element matrices $\boldsymbol{g}^{d,(e)} = \boldsymbol{g}^{\lambda,(e)^T}$.

4.3.2 Penalty method

Inserting the discretizations (3.7) and (3.8) into the penalty terms of the variational problem (4.18) yields:

$$\delta \Pi^{pen} \approx \sum_{e=1}^{cutnumele} \left\{ \delta \tilde{\boldsymbol{d}}^T \alpha \int_{\Gamma_*^{(e)}} [\![\tilde{\boldsymbol{N}}]\!]^T [\![\boldsymbol{u}^h]\!] \, \mathrm{d}\Gamma \right\} \tag{4.49}$$

From the discretized variational problem, the elementary penalty contribution to the residual can be extracted:

$$\begin{aligned} \boldsymbol{r}^{pen,(e)} &= \begin{bmatrix} \mathbf{0}_{6\times 1} \\ \alpha \int_{\Gamma_*^{(e)}} [\![\tilde{\boldsymbol{N}}]\!]^T [\![\boldsymbol{u}^h]\!] \, \mathrm{d}\Gamma \end{bmatrix} \\ &= \begin{bmatrix} \mathbf{0}_{6\times 1} \\ \alpha_n \int_{\Gamma_*^{(e)}} [\![\tilde{\boldsymbol{N}}]\!]^T \boldsymbol{n}\boldsymbol{n}^T [\![\boldsymbol{u}^h]\!] \, \mathrm{d}\Gamma + \alpha_t \int_{\Gamma_*^{(e)}} [\![\tilde{\boldsymbol{N}}]\!]^T \left(\boldsymbol{I} - \boldsymbol{n}\boldsymbol{n}^T\right) [\![\boldsymbol{u}^h]\!] \, \mathrm{d}\Gamma \end{bmatrix} \end{aligned} \tag{4.50}$$

The second part of (4.50) presents the residual for the decomposition into normal and tangential direction. Remember remark 4.1 for the choice of the penalty parameters. The elementary penalty residuals can be assembled to a global penalty contribution to the global residual:

$$\boldsymbol{R}^{pen} = \bigmathop{\mathsf{A}}_{e=1}^{cutnumele} \boldsymbol{r}^{pen,(e)} \tag{4.51}$$

such that the global system of equations that has to be solved is built with the global residual of the untied problem plus the penalty contribution:

$$\boldsymbol{R} = \boldsymbol{R}^u + \boldsymbol{R}^{pen} = 0 \tag{4.52}$$

The penalty contribution to the global tangent stiffness matrix is obtained by deriving the global penalty contribution to the global residual with respect to the displacements. The linearity of the assembly operator is used to define elementary penalty based stiffness contributions

$$\boldsymbol{K}^{pen} = \frac{\partial \boldsymbol{R}^{pen}}{\partial \boldsymbol{D}} = \frac{\partial \mathsf{A}_{e=1}^{cutnumele} \boldsymbol{r}^{pen,(e)}}{\partial \boldsymbol{D}} = \bigmathop{\mathsf{A}}_{e=1}^{cutnumele} \frac{\partial \boldsymbol{r}^{pen,(e)}}{\partial \boldsymbol{d}} = \bigmathop{\mathsf{A}}_{e=1}^{cutnumele} \boldsymbol{k}^{pen,(e)} \tag{4.53}$$

with

$$\boldsymbol{k}^{pen,(e)} = \begin{bmatrix} \mathbf{0}_{6\times 6} & \mathbf{0}_{6\times 6} \\ \mathbf{0}_{6\times 6} & \boldsymbol{\kappa}_{22}^{pen,(e)} \end{bmatrix} \tag{4.54}$$

and

$$\begin{aligned}\boldsymbol{\kappa}_{22}^{pen,(e)} &= \alpha \int_{\Gamma_*^{(e)}} [\![\tilde{\boldsymbol{N}}]\!]^T [\![\tilde{\boldsymbol{N}}]\!] \, \mathrm{d}\Gamma \\ &= \alpha_n \int_{\Gamma_*^{(e)}} [\![\tilde{\boldsymbol{N}}]\!]^T \boldsymbol{n}\boldsymbol{n}^T [\![\tilde{\boldsymbol{N}}]\!] \, \mathrm{d}\Gamma + \alpha_t \int_{\Gamma_*^{(e)}} [\![\tilde{\boldsymbol{N}}]\!]^T \left(\boldsymbol{I} - \boldsymbol{n}\boldsymbol{n}^T\right) [\![\tilde{\boldsymbol{N}}]\!] \, \mathrm{d}\Gamma\end{aligned} \tag{4.55}$$

The second part of (4.55) represents the form for the decomposition into normal and tangential direction. Remember remark 4.1 for the choice of the penalty parameters. Here, it can be seen clearly that for the penalty method the coupling between the two grains happens only in the enriched degrees of freedom. This is based on the definition of the penalty method since it is a regularization, linear in the jump in the displacement field. Since this jump depends only on the enriched degrees of freedom, the element stiffness matrix in (4.54) is mostly populated with zeros.

4.3.3 Nitsche's method

In order to discretize the variational problem for Nitsche's method, some discretization issues of the stress tensor, $\underline{\boldsymbol{\sigma}}$, shall be discussed first. The discrete counterpart to the stress tensor is the discrete stress vector, $\boldsymbol{\sigma}$, in *Voigt* notation. To clarify the difference between the continuous stress tensor and the discrete stress vector, the latter one is denoted with the superscript h in the following. Using the *Voigt* notation, a tensor represented by a 2×2 matrix is approximated by a 3×1 vector. This change in dimensionality requires an adaptaion of the product $\underline{\boldsymbol{\sigma}}\,\underline{\boldsymbol{n}}$ when going from the continuous to the discrete regime where the average operator $\langle \bullet \rangle$ is omitted for now to simplify the notation. In the continuous regime, this product reads:

$$\underline{\boldsymbol{\sigma}}\,\underline{\boldsymbol{n}} = \begin{bmatrix} \sigma_{11} & \sigma_{12} \\ \sigma_{21} & \sigma_{22} \end{bmatrix} \begin{bmatrix} n_1 \\ n_2 \end{bmatrix} = \begin{bmatrix} \sigma_{11} n_1 + \sigma_{12} n_2 \\ \sigma_{21} n_1 + \sigma_{22} n_2 \end{bmatrix} \tag{4.56}$$

The discrete counterpart to $\underline{\boldsymbol{\sigma}}\,\underline{\boldsymbol{n}}$ has to result in the same expression. The normal vector, $\boldsymbol{n}$, has to be replaced by a matrix, $\check{\boldsymbol{n}}$, which leads to the same expression when multiplying with the discrete vector, $\boldsymbol{\sigma}^h$:

$$\check{\boldsymbol{n}}\boldsymbol{\sigma}^h = \begin{bmatrix} n_1 & 0 & n_2 \\ 0 & n_2 & n_1 \end{bmatrix} \begin{bmatrix} \sigma_{11}^h \\ \sigma_{22}^h \\ \sigma_{12}^h \end{bmatrix} = \begin{bmatrix} \sigma_{11}^h n_1 + \sigma_{12}^h n_2 \\ \sigma_{21} h n_1 + \sigma_{22}^h n_2 \end{bmatrix} \approx \begin{bmatrix} \sigma_{11} n_1 + \sigma_{12} n_2 \\ \sigma_{21} n_1 + \sigma_{22} n_2 \end{bmatrix} \tag{4.57}$$

Since the stress is computed as $\underline{\boldsymbol{\sigma}} = \underline{\boldsymbol{C}} : \underline{\boldsymbol{\varepsilon}}$, the enrichments in the strain field yields the following form of the stress tensor:

$$\underline{\boldsymbol{\sigma}}\left(\underline{\boldsymbol{u}}\right) = \underline{\boldsymbol{\sigma}}\left(\hat{\underline{\boldsymbol{u}}} + \sum_m H^{(m)} \tilde{\underline{\boldsymbol{u}}}^{(m)}\right) = \underline{\boldsymbol{\sigma}}\left(\hat{\underline{\boldsymbol{u}}}\right) + \sum_m H^{(m)} \underline{\boldsymbol{\sigma}}\left(\tilde{\underline{\boldsymbol{u}}}^{(m)}\right) \tag{4.58}$$

This is valid in the discrete regime as well where the dependency of the stress vector on the nodal displacements is inserted:

$$\boldsymbol{\sigma}^h = \boldsymbol{C}\boldsymbol{B}\boldsymbol{d} = \boldsymbol{C}\hat{\boldsymbol{B}}\hat{\boldsymbol{d}} + \sum_m \left(H^{(m)} \boldsymbol{C}^{(m)} \tilde{\boldsymbol{B}}^{(m)}\right) \tilde{\boldsymbol{d}} \tag{4.59}$$

Inserting the discretizations into the variation of the Nitsche potential (4.30) yields the following discrete expression:

$$\begin{aligned}
\delta\Pi^{Nit} \approx & \sum_{e=1}^{cutnumele} \left\{ \alpha \int_{\Gamma_*^{(e)}} \left(\llbracket \tilde{\boldsymbol{N}} \rrbracket \delta\tilde{\boldsymbol{d}}\right)^T \llbracket \boldsymbol{u}^h \rrbracket \,\mathrm{d}\Gamma - \int_{\Gamma_*^{(e)}} \left(\llbracket \tilde{\boldsymbol{N}} \rrbracket \delta\tilde{\boldsymbol{d}}\right)^T \check{\boldsymbol{n}} \langle \boldsymbol{\sigma}^h \rangle \,\mathrm{d}\Gamma \right\} \\
& - \sum_{e=1}^{cutnumele} \left\{ \int_{\Gamma_*^{(e)}} \llbracket \boldsymbol{u}^h \rrbracket^T \check{\boldsymbol{n}} \langle \boldsymbol{C}\hat{\boldsymbol{B}}\delta\hat{\boldsymbol{d}} + \sum_m \left(H^{(m)} \boldsymbol{C}^{(m)} \tilde{\boldsymbol{B}}^{(m)} \delta\tilde{\boldsymbol{d}}\right) \rangle \,\mathrm{d}\Gamma \right\} \\
& = \sum_{e=1}^{cutnumele} \left\{ \delta\tilde{\boldsymbol{d}}^T \alpha \int_{\Gamma_*^{(e)}} \llbracket \tilde{\boldsymbol{N}} \rrbracket^T \llbracket \boldsymbol{u}^h \rrbracket \,\mathrm{d}\Gamma - \delta\tilde{\boldsymbol{d}}^T \int_{\Gamma_*^{(e)}} \llbracket \tilde{\boldsymbol{N}} \rrbracket^T \check{\boldsymbol{n}} \langle \boldsymbol{\sigma}^h \rangle \,\mathrm{d}\Gamma \right\} \\
& - \sum_{e=1}^{cutnumele} \left\{ \delta\tilde{\boldsymbol{d}}^T \int_{\Gamma_*^{(e)}} \langle \boldsymbol{C}\hat{\boldsymbol{B}} \rangle^T \check{\boldsymbol{n}}^T \llbracket \boldsymbol{u}^h \rrbracket \,\mathrm{d}\Gamma \right\} \\
& - \sum_{e=1}^{cutnumele} \left\{ \delta\tilde{\boldsymbol{d}}^T \int_{\Gamma_*^{(e)}} \langle \sum_m \left(H^{(m)} \boldsymbol{C}^{(m)} \tilde{\boldsymbol{B}}^{(m)}\right) \rangle^T \check{\boldsymbol{n}}^T \llbracket \boldsymbol{u}^h \rrbracket \,\mathrm{d}\Gamma \right\}
\end{aligned} \tag{4.60}$$

From the discretized variational problem, the elementary Nitsche contribution to the residual can be extracted:

$$\boldsymbol{r}^{Nit,(e)} = \begin{bmatrix} -\int_{\Gamma_*^{(e)}} \langle \boldsymbol{C}\hat{\boldsymbol{B}} \rangle^T \check{\boldsymbol{n}}^T \llbracket \boldsymbol{u}^h \rrbracket \,\mathrm{d}\Gamma \\ \alpha \int_{\Gamma_*^{(e)}} \llbracket \tilde{\boldsymbol{N}} \rrbracket^T \llbracket \boldsymbol{u}^h \rrbracket \,\mathrm{d}\Gamma - \int_{\Gamma_*^{(e)}} \llbracket \tilde{\boldsymbol{N}} \rrbracket^T \check{\boldsymbol{n}} \langle \boldsymbol{\sigma}^{\boldsymbol{h}} \rangle \,\mathrm{d}\Gamma - \int_{\Gamma_*^{(e)}} \langle \boldsymbol{C}\tilde{\boldsymbol{B}} \rangle^T \check{\boldsymbol{n}}^T \llbracket \boldsymbol{u}^h \rrbracket \,\mathrm{d}\Gamma \end{bmatrix} \tag{4.61}$$

where the shorthand notation

$$\langle \boldsymbol{C}\tilde{\boldsymbol{B}} \rangle = \langle \sum_m \left(H^{(m)} \boldsymbol{C}^{(m)} \tilde{\boldsymbol{B}}^{(m)}\right) \rangle \tag{4.62}$$

is introduced. The stabilization term is totally equivalent to the penalty term presented in the previous section. The elementary Nitsche residuals can be assembled to a global Nitsche contribution to the global residual:

$$\boldsymbol{R}^{Nit} = \mathop{\mathsf{A}}_{e=1}^{cutnumele} \boldsymbol{r}^{Nit,(e)} \tag{4.63}$$

such that the global system of equations that has to be solved is built with the global residual of the untied problem plus the Nitsche contribution:

$$\boldsymbol{R} = \boldsymbol{R}^{u} + \boldsymbol{R}^{Nit} = 0 \tag{4.64}$$

The Nitsche contribution to the global tangent stiffness matrix is obtained by deriving the global Nitsche contribution to the global residual with respect to the displacements. The linearity of the assembly operator is used to define elementary Nitsche based stiffness contributions

$$\boldsymbol{K}^{Nit} = \frac{\partial \boldsymbol{R}^{Nit}}{\partial \boldsymbol{D}} = \frac{\partial \mathsf{A}_{e=1}^{cutnumele} \boldsymbol{r}^{Nit,(e)}}{\partial \boldsymbol{D}} = \mathop{\mathsf{A}}_{e=1}^{cutnumele} \frac{\partial \boldsymbol{r}^{Nit,(e)}}{\partial \boldsymbol{d}} = \mathop{\mathsf{A}}_{e=1}^{cutnumele} \boldsymbol{k}^{Nit,(e)} \tag{4.65}$$

with

$$\boldsymbol{k}^{Nit,(e)} = \begin{bmatrix} \boldsymbol{0}_{6\times 6} & \boldsymbol{\kappa}_{12}^{Nit,(e)} \\ \boldsymbol{\kappa}_{21}^{Nit,(e)} & \boldsymbol{\kappa}_{22}^{Nit,(e)} \end{bmatrix} \tag{4.66}$$

and

$$\begin{aligned} \boldsymbol{\kappa}_{12}^{Nit,(e)} &= -\int_{\Gamma_*^{(e)}} \langle \boldsymbol{C}\hat{\boldsymbol{B}} \rangle^T \check{\boldsymbol{n}}^T [\![\tilde{\boldsymbol{N}}]\!] \, \mathrm{d}\Gamma \\ \boldsymbol{\kappa}_{21}^{Nit,(e)} &= -\int_{\Gamma_*^{(e)}} [\![\tilde{\boldsymbol{N}}]\!]^T \check{\boldsymbol{n}} \langle \boldsymbol{C}\hat{\boldsymbol{B}} \rangle \, \mathrm{d}\Gamma \\ \boldsymbol{\kappa}_{22}^{Nit,(e)} &= \alpha \int_{\Gamma_*^{(e)}} [\![\tilde{\boldsymbol{N}}]\!]^T [\![\tilde{\boldsymbol{N}}]\!] \mathrm{d}\Gamma - \int_{\Gamma_*^{(e)}} [\![\tilde{\boldsymbol{N}}]\!]^T \check{\boldsymbol{n}} \langle \boldsymbol{C}\tilde{\boldsymbol{B}} \rangle \, \mathrm{d}\Gamma - \int_{\Gamma_*^{(e)}} \langle \boldsymbol{C}\tilde{\boldsymbol{B}} \rangle^T \check{\boldsymbol{n}}^T [\![\tilde{\boldsymbol{N}}]\!] \, \mathrm{d}\Gamma \end{aligned} \tag{4.67}$$

Due to the symmetry of Nitsche's bilinear form, it is not surprising, that $\boldsymbol{\kappa}_{12}^{Nit,(e)} = \boldsymbol{\kappa}_{21}^{Nit,(e)^T}$ and that also the last two terms in $\boldsymbol{\kappa}_{22}^{Nit,(e)}$ are the transpose of each other. So, the element stiffness contribution for Nitsche's method is symmetric.

Remark 4.3. *The stabilization contribution in $\boldsymbol{k}^{Nit,(e)}$ is the same as in the penalty method.*

It can be seen, that through the entire derivation and discretization, the stabilization terms always equal the penalty terms. This might be helpful for the implementation: In order to obtain a Nitsche implementation, only additional code has to be added to a penalty code.

It has been shown in the original contribution [30] as well as in its analysis [39], that the parameter α has to take at least a minimum value to guarantee the coercivity of the bilinear form. Following [8], where an estimate for α for scalar problems is given, now an estimate for α in a two-dimensional elasticity problem shall be derived. A local approach is used. Following the notation in [8], the variational form for Nitsche's method (4.33) can be rewritten in a general form without considering the paricular form of the enriched displacement field since it is not important for this derivation:

$$a(\underline{\boldsymbol{u}}, \underline{\boldsymbol{w}}) - l(\underline{\boldsymbol{w}}) = 0 \tag{4.68}$$

with the bilinear form, $a(\underline{\boldsymbol{u}}, \underline{\boldsymbol{w}})$, representing the internal contributions from the bulk and the interfacial field

$$\begin{aligned} a(\underline{\boldsymbol{u}}, \underline{\boldsymbol{w}}) = & \int_\Omega w_{i,j} C_{ijkl} \varepsilon_{kl} \, \mathrm{d}\Omega + \alpha \int_{\Gamma_*} [\![w_i]\!] [\![u_i]\!] \, \mathrm{d}\Gamma \\ & - \int_{\Gamma_*} [\![w_i]\!] \langle C_{ijkl} \varepsilon_{kl} \rangle n_j \, \mathrm{d}\Gamma - \int_{\Gamma_*} [\![u_i]\!] \langle C_{ijkl} w_{k,l} \rangle n_j \, \mathrm{d}\Gamma \end{aligned} \tag{4.69}$$

and the linear form, $l(\underline{\boldsymbol{w}})$, representing the external contribution from body forces b_i and external tractions h_i on the Neumann boundary:

$$l(\underline{\boldsymbol{w}}) = \int_\Omega w_i b_i \, \mathrm{d}\Omega + \int_{\Gamma_\sigma} w_i h_i \, \mathrm{d}\Gamma \tag{4.70}$$

Remark 4.4. *In the context of a bilinear form, one usually considers weight functions w_i instead of variations in the displacement field. As a matter of fact, the principle of the minimum of the total potential energy ends up with the same formulation as the method of weighted residuals in a continuum mechanics context. Hence, δu_i can be replaced by a weight function w_i.*

The goal is to provide a rule that helps to choose α such that the bilinear form $a(\underline{\boldsymbol{u}}, \underline{\boldsymbol{w}})$ is coercive regardless of the values of $\underline{\boldsymbol{u}}$ and $\underline{\boldsymbol{w}}$:

$$a(\underline{\boldsymbol{u}}, \underline{\boldsymbol{w}}) \geq 0 \qquad \forall \, (\underline{\boldsymbol{u}}, \underline{\boldsymbol{w}}) \tag{4.71}$$

First, an "energy" norm is defined for the sake of convenience:

$$\|u_i\|^2_{\Omega,\underline{\boldsymbol{C}}} = (\varepsilon_{ij}, C_{ijkl}\varepsilon_{kl}) = \int_\Omega \varepsilon_{ij} C_{ijkl} \varepsilon_{kl} \,\mathrm{d}\Omega \tag{4.72}$$

where $(\cdot,\cdot)$ denotes the $\mathbb{L}_2$ inner product. The duality pairing $\left\langle \cdot, \cdot \right\rangle$ denotes integration along the interface.

Remark 4.5. *These notations are adopted from [8]. Unfortunately, the expressions* $\left\langle \cdot, \cdot \right\rangle$ *and* $\langle \bullet \rangle$ *seem to be very similar, but they are not. The first one with the comma in between symbolizes an integration whereas the second one without a comma denotes the average operator introduced in* (4.29)*. The difference is also emphasized in the size of the operator. Despite this clash of notations, they are used here, since they commonly appear in literature. Similar notations are introduced in [4, 8, 39].*

Following [8], there is a configuration-dependent constant $C_I > 0$ such that:

$$\|\langle C_{ijkl}\varepsilon_{kl}\rangle n_j\|_{\Gamma_*} \leq C_I \|u_i\|_{\Omega,\underline{\boldsymbol{C}}} \tag{4.73}$$

with

$$\|\langle C_{ijkl}\varepsilon_{kl}\rangle n_j\|^2_{\Gamma_*} = \int_{\Gamma_*} \left(\langle C_{ijkl}\varepsilon_{kl}\rangle n_j\right) \left(\langle C_{ijkl}\varepsilon_{kl}\rangle n_j\right) \,\mathrm{d}\Gamma \tag{4.74}$$

Considering $a(\underline{\boldsymbol{w}}, \underline{\boldsymbol{w}})$ and rewriting it, using the shorthand notations, yields:

$$a(\underline{\boldsymbol{w}}, \underline{\boldsymbol{w}}) = \|w_i\|^2_{\Omega,\underline{\boldsymbol{C}}} + \alpha \|[\![w_i]\!]\|^2_{\Gamma_*} - 2\left\langle [\![w_i]\!], \langle C_{ijkl} w_{k,l}\rangle n_j \right\rangle \tag{4.75}$$

The *Cauchy-Schwarz inequality* can be applied to the last term:

$$\left\langle [\![w_i]\!], \langle C_{ijkl} w_{k,l}\rangle n_j \right\rangle \leq \|[\![w_i]\!]\|_{\Gamma_*} \|\langle C_{ijkl} w_{k,l}\rangle n_j\|_{\Gamma_*} \tag{4.76}$$

Inserting this into (4.75) yields a lower bound for the bilinear form:

$$a(\underline{\boldsymbol{w}}, \underline{\boldsymbol{w}}) \geq \|w_i\|^2_{\Omega,\underline{\boldsymbol{C}}} + \alpha \|[\![w_i]\!]\|^2_{\Gamma_*} - 2\|[\![w_i]\!]\|_{\Gamma_*} \|\langle C_{ijkl} w_{k,l}\rangle n_j\|_{\Gamma_*} \tag{4.77}$$

Using (4.73) and adding and subtracting $C_I^2 \|[\![w_i]\!]\|_{\Gamma_*}^2$ yields:

$$\begin{aligned} a(\underline{\boldsymbol{w}}, \underline{\boldsymbol{w}}) \geq \|w_i\|_{\Omega,\underline{\boldsymbol{C}}}^2 - 2C_I \|[\![w_i]\!]\|_{\Gamma_*} \|w_i\|_{\Omega,\underline{\boldsymbol{C}}} + C_I^2 \|[\![w_i]\!]\|_{\Gamma_*}^2 \\ + \alpha \|[\![w_i]\!]\|_{\Gamma_*}^2 - C_I^2 \|[\![w_i]\!]\|_{\Gamma_*}^2 \end{aligned} \tag{4.78}$$

Now, the binomial theorem can be applied leading to:

$$a(\underline{\boldsymbol{w}}, \underline{\boldsymbol{w}}) \geq \overbrace{\left(\|w_i\|_{\Omega,\underline{\boldsymbol{C}}} - C_I^2 \|[\![w_i]\!]\|_{\Gamma_*}\right)^2}^{\geq 0} + \left(\alpha - C_I^2\right) \|[\![w_i]\!]\|_{\Gamma_*}^2 \tag{4.79}$$

In (4.79), it can easily be seen that the coercivity of the bilinear form depends only on a relation between α and C_I since the first term on the right hand side is always greater or equal to zero. The condition for coercivity can be formulated as:

$$\alpha \geq C_I^2 \tag{4.80}$$

As mentioned above, a local approach is considered here. If (4.71) is satisfied in every element, then it is also satisfied globally. Hence, all further investigations are done in a discrete space, using the discretizations introduced so far. Therefor, linear shape functions are assumed such that the strain and the gradient of the weight function in an element are constant. This implies that the derivation is only valid for triangular elements, since it is the only element type with a constant gradient in the entire element. It is also assumed, that the constitutive tensor is constant within one element as well as its discrete counterpart. (4.71) holds only if (4.73) holds, too. A deeper look at (4.73) leads to a relation between α and C_I such that (4.73) and hence (4.71) holds. In the following, this rule for matrix norms will be applied [31]:

$$|\boldsymbol{A}\boldsymbol{B}| \leq |\boldsymbol{A}||\boldsymbol{B}| \tag{4.81}$$

where $|\boldsymbol{A}|$ denotes the 2-norm of matrix $\boldsymbol{A}$. Investigating the right hand side of (4.73) and

using the discrete counterpart of the "energy" norm (4.72) yields:

$$\begin{aligned}\|\boldsymbol{w}\|^2_{\Omega,\boldsymbol{C}} &= \int_{\Omega^{(e)}} \nabla\boldsymbol{w}^T \boldsymbol{C} \nabla\boldsymbol{w} \,\mathrm{d}\Omega \\ &= \int_{\Omega^{(1),(e)}} \nabla\boldsymbol{w}^{(1)^T} \boldsymbol{C}^{(1)} \nabla\boldsymbol{w}^{(1)} \,\mathrm{d}\Omega + \int_{\Omega^{(2),(e)}} \nabla\boldsymbol{w}^{(2)^T} \boldsymbol{C}^{(2)} \nabla\boldsymbol{w}^{(2)} \,\mathrm{d}\Omega \\ &= |\nabla\boldsymbol{w}^{(1)^T} \boldsymbol{C}^{(1)} \nabla\boldsymbol{w}^{(1)}| A^{(1)} + |\nabla\boldsymbol{w}^{(2)^T} \boldsymbol{C}^{(2)} \nabla\boldsymbol{w}^{(2)}| A^{(2)} \\ &\leq |\boldsymbol{C}^{(1)}||\nabla\boldsymbol{w}^{(1)}|^2 A^{(1)} + |\boldsymbol{C}^{(2)}||\nabla\boldsymbol{w}^{(2)}|^2 A^{(2)}\end{aligned} \tag{4.82}$$

with the measures of the area, $A^{(1)} = meas\left(\Omega^{(1),(e)}\right)$ and $A^{(2)} = meas\left(\Omega^{(2),(e)}\right)$, as depicted in figure 4.2. Looking at the left hand side of (4.73) yields:

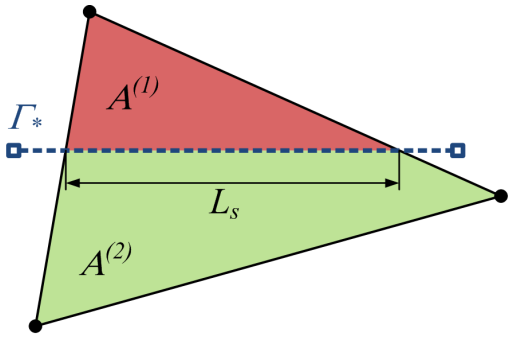

FIGURE 4.2: Geometric quantities to calculate the stabilization parameter α for Nitsche's method in a linear triangular element: The area of the element is divided into two subareas, $A^{(1)}$ and $A^{(2)}$, by a subsegment of Γ_* with the length L_s.

$$\|\langle \boldsymbol{C}\nabla\boldsymbol{w}\rangle\boldsymbol{n}\|_{\Gamma_*^{(e)}} = |\langle \boldsymbol{C}\nabla\boldsymbol{w}\rangle\boldsymbol{n}|^2 \cdot L_s \tag{4.83}$$

where $L_s = meas\left(\Gamma_*^{(e)}\right)$ denotes a measured length of the subsegment of the interface intersecting with the element, see figure 4.2. For the following transformations, the results from appendix B regarding *Young's inequality with* ϵ are used. Identifiying $c = \boldsymbol{C}^{(2)}\nabla\boldsymbol{w}^{(2)}$

and $d = \boldsymbol{C}^{(1)}\nabla\boldsymbol{w}^{(1)}$, the first term on the right hand side in (4.83) reads:

$$\begin{aligned}|\langle \boldsymbol{C}\nabla\boldsymbol{w}\rangle\boldsymbol{n}|^2 &\leq |\langle \boldsymbol{C}\nabla\boldsymbol{w}\rangle|^2 \overbrace{|\boldsymbol{n}|^2}^{=1} = \frac{1}{4}|\boldsymbol{C}^{(1)}\nabla\boldsymbol{w}^{(1)} + \boldsymbol{C}^{(2)}\nabla\boldsymbol{w}^{(2)}|^2 \\ &\leq \frac{1}{4}(1+\epsilon)|\boldsymbol{C}^{(1)}\nabla\boldsymbol{w}^{(1)}|^2 + \frac{1}{4}(1+\frac{1}{\epsilon})|\boldsymbol{C}^{(2)}\nabla\boldsymbol{w}^{(2)}|^2 \\ &\leq \frac{1}{4}(1+\epsilon)|\boldsymbol{C}^{(1)}|^2|\nabla\boldsymbol{w}^{(1)}|^2 + \frac{1}{4}(1+\frac{1}{\epsilon})|\boldsymbol{C}^{(2)}|^2|\nabla\boldsymbol{w}^{(2)}|^2\end{aligned} \tag{4.84}$$

Selecting ϵ as

$$\epsilon = \frac{|\boldsymbol{C}^{(2)}|A^{(1)}}{|\boldsymbol{C}^{(1)}|A^{(2)}} \tag{4.85}$$

yields:

$$\begin{aligned}|\langle \boldsymbol{C}\nabla\boldsymbol{w}\rangle\boldsymbol{n}|^2 &\leq \frac{1}{4}\left(1 + \frac{|\boldsymbol{C}^{(2)}|A^{(1)}}{|\boldsymbol{C}^{(1)}|A^{(2)}}\right)|\boldsymbol{C}^{(1)}|^2|\nabla\boldsymbol{w}^{(1)}|^2 \\ &\quad + \frac{1}{4}\left(1 + \frac{|\boldsymbol{C}^{(1)}|A^{(2)}}{|\boldsymbol{C}^{(2)}|A^{(1)}}\right)|\boldsymbol{C}^{(2)}|^2|\nabla\boldsymbol{w}^{(2)}|^2 \\ &= \frac{1}{4}\left(\frac{|\boldsymbol{C}^{(1)}|}{A^{(1)}} + \frac{|\boldsymbol{C}^{(2)}|}{A^{(2)}}\right)\left(A^{(1)}|\boldsymbol{C}^{(1)}||\nabla\boldsymbol{w}^{(1)}|^2 + A^{(2)}|\boldsymbol{C}^{(2)}||\nabla\boldsymbol{w}^{(2)}|^2\right)\end{aligned} \tag{4.86}$$

Inserting the results of (4.82) and (4.86) into (4.73) yields a lower bound for C_I^2:

$$C_I^2 \geq \frac{L_s}{4}\left(\frac{|\boldsymbol{C}^{(1)}|}{A^{(1)}} + \frac{|\boldsymbol{C}^{(2)}|}{A^{(2)}}\right) \tag{4.87}$$

Following the local approach, the stabilization parameter $\alpha = \alpha_e$ has to be computed for each element separately. According to (4.80), it is suffucient to choose $\alpha_e = C_I^2$ to guarantee coercivity of the bilinear form, but following [8], the choice

$$\alpha_e = 2C_I^2 \tag{4.88}$$

is recommended since it assures the coercivity of the bilinear form as well as provides good performance in computation. In general, the solution is not as sensitive to the choice of α, if $\alpha > \alpha_{min}$, as for the penalty method. Though, it is not recommended to choose the

stabilization parameter much higher than necessary since then the stabilization term would outpace the other terms in the stiffness matrix. A sensitivity analysis is performed in [13]. Since L_s as well as $A^{(m)}$ in (4.87) depend on the mesh size h, it can be seen easily that the stabilization parameter scales $1/h$.

Remark 4.6. *The reader may be informed that neither a plain stress nor a plain strain state was assumed to develop this estimate of the stabilization parameter. It thus can be used for both types equally.*

5 The frictionless sliding problem

In this section, frictionless sliding at the interface is introduced. The same methods as for the fully tied problem are used to constrain the interface, but they have to be modified. First, the constraints at the interface are shown. Afterwards, the variational forms and the discretization for Lagrange multipliers, penalty method and Nitsche's method are presented for the frictionless sliding problem.

5.1 Constraints for kinematics and tractions

For the frictionless sliding problem, the continuity of the displacement field is only required in normal direction with respect to the interface Γ_*. Hence, (4.5) has to be modified:

$$[\![u_i]\!] n_i \doteq 0 \text{ on } \Gamma_* \tag{5.1}$$

where n_i denotes the normal vector, as it was introduced in section 2. Similar modifications have to be done for every appearance of the variation of the displacement field. The definition of the *gap*-function in contact mechanics which measures the gap in normal direction is done in a similar way, see for example [23, 45]. Due to frictionless sliding, only normal tractions can be assigned across the embedded interface:

$$n_i \sigma_{ij}^{(1)} n_j^{(1)} + n_i \sigma_{ij}^{(2)} n_j^{(2)} = 0 \text{ on } \Gamma_* \tag{5.2}$$

The tangential direction is not constrained. This might result in problems with rigid body modes which have to be constrained properly using Dirichlet boundary conditions.

5.2 Variational forms

The variational forms for frictionless sliding for Lagrange multipliers, penalty method and Nitsche's method are introduced by modifying the potentials of the fully tied problem and building their first variations.

5.2.1 Lagrange multipliers

Since tractions in the interface occur only in normal direction, the Lagrange multiplier field has to be projected onto the normal direction, too. The potential for Lagrange multipliers

with frictionless sliding reads:

$$\Pi^{Lag} = \int_{\Gamma_*} \lambda_i n_i n_j [\![u_j]\!] \, \mathrm{d}\Gamma \tag{5.3}$$

Here, also the dyadic product of the normal vector, $n_i n_j$, occurs which was introduced when the decomposition into a normal and a tangential traction was shown in (4.14).

Remark 5.1. *The potential for Lagrange multipliers for the fully tied problem was denoted by Π^{Lag}, too, as well as it is done here for the frictionless sliding problem. It is obvious that these two potentials are different, but in order to keep the number of indices and superscripts small, the same notation is used. This clash of notations happens not only for Lagrange multipliers but will occur several times in the following sections. Though, it will be totally obvious from the context which type of problem is considered.*

Building the first variation, $\delta\Pi^{Lag}$, yields:

$$\delta\Pi^{Lag} = \int_{\Gamma_*} \lambda_i n_i n_j [\![\delta u_j]\!] \, \mathrm{d}\Gamma + \int_{\Gamma_*} \delta\lambda_i n_i n_j [\![u_j]\!] \, \mathrm{d}\Gamma \tag{5.4}$$

Using the same arguments as in section 4.2.1 yields the variational problem for frictionless sliding at the interface with Lagrange multipliers:

Find $(\boldsymbol{u}, \boldsymbol{\lambda}) \in \mathcal{U} \times \mathcal{L}$ for all $(\delta\boldsymbol{u}, \delta\boldsymbol{\lambda}) \in \mathcal{V} \times \mathcal{L}$ such that

$$\begin{aligned}
\delta\Pi = &\int_\Omega \delta\hat{\varepsilon}_{ij}\sigma_{ij} \, \mathrm{d}\Omega + \sum_m \int_{\Omega^{(m)}} H^{(m)} \delta\tilde{\varepsilon}_{ij}^{(m)} \sigma_{ij}^{(m)} \, \mathrm{d}\Omega \\
&+ \int_{\Gamma_*} [\![\delta u_i]\!] n_i n_j \lambda_j \, \mathrm{d}\Gamma + \int_{\Gamma_*} \delta\lambda_i n_i n_j [\![u_j]\!] \, \mathrm{d}\Gamma \\
&- \int_\Omega \delta\hat{u}_i b_i \, \mathrm{d}\Omega - \sum_m \int_{\Omega^{(m)}} H^{(m)} \delta\tilde{u}_i^{(m)} b_i^{(m)} \, \mathrm{d}\Omega \\
&- \int_{\Gamma_\sigma} \delta\hat{u}_i h_i \, \mathrm{d}\Gamma - \sum_m \int_{\Gamma_\sigma^{(m)}} H^{(m)} \delta\tilde{u}_i^{(m)} h_i^{(m)} \, \mathrm{d}\Gamma = 0
\end{aligned} \tag{5.5}$$

The stability problems, mentioned in section 4.2.1, occur here, too. A numerical example showing the oscillations in the traction field is provided in section 9.2.2.

5.2.2 Penalty method

The approximation of the Lagrange multiplier, as given in (4.13), has to be modified. Pluging in (5.1) results in

$$\lambda \approx \alpha [\![u_i]\!] n_i. \tag{5.6}$$

These modifications affect the potential, Π^{pen}:

$$\Pi^{pen} = \frac{1}{2} \int_{\Gamma_*} \alpha [\![u_i]\!] n_i n_j [\![u_j]\!] \, \mathrm{d}\Gamma \tag{5.7}$$

Comparing to contact mechanics, this is similar to the penalty potential for frictionless contact. Here, also the dyadic product of the normal vector, $n_i n_j$, is introduced to account for the decomposition into a normal and a tangential traction as shown in (4.14). The entire potential is built from the potential of the untied problem and the new penalty potential. Building the first variation, $\delta \left(\Pi^u + \Pi^{pen} \right)$, and using the same arguments as in section 4.2.2 yields the variational problem for frictionless sliding at the interface with the penalty method:

Find $\boldsymbol{u} \in \mathcal{U}$ for all $\delta \boldsymbol{u} \in \mathcal{V}$ such that

$$\begin{aligned} \delta\Pi = & \int_\Omega \delta\hat{\varepsilon}_{ij} \sigma_{ij} \, \mathrm{d}\Omega + \sum_m \int_{\Omega^{(m)}} H^{(m)} \delta\tilde{\varepsilon}_{ij}^{(m)} \sigma_{ij}^{(m)} \, \mathrm{d}\Omega + \alpha \int_{\Gamma_*} [\![\delta u_i]\!] n_i n_j [\![u_j]\!] \, \mathrm{d}\Gamma \\ & - \int_\Omega \delta\hat{u}_i b_i \, \mathrm{d}\Omega - \sum_m \int_{\Omega^{(m)}} H^{(m)} \delta\tilde{u}_i^{(m)} b_i^{(m)} \, \mathrm{d}\Omega \\ & - \int_{\Gamma_\sigma} \delta\hat{u}_i h_i \, \mathrm{d}\Gamma - \sum_m \int_{\Gamma_\sigma^{(m)}} H^{(m)} \delta\tilde{u}_i^{(m)} h_i^{(m)} \, \mathrm{d}\Gamma = 0 \end{aligned} \tag{5.8}$$

Another way to obtain this variational problem is to use the one with splitted normal and tangential parts of the fully tied case (4.19) and choosing the tangential penalty parameter as zero: $\alpha_t = 0$. This equals the removal of all tangential stiffness at the interface and results in frictionless sliding, too. The properties of the penalty method are preserved, of course. Numerical examples and convergence rates are shown in section 9.2.

5.2.3 Nitsche's method

The modifications in the interfacial constraints yield a modified Nitsche potential:

$$\Pi^{Nit} = \int_{\Gamma_*} \left(-\langle \sigma(\boldsymbol{u})_{jk} \rangle n_k + \frac{\alpha}{2} [\![u_j]\!] \right) n_j n_i [\![u_i]\!] \, \mathrm{d}\Gamma \tag{5.9}$$

Using the same arguments as in section 4.2.3, the first variation of the entire potential yields the variational problem for frictionless sliding at the interface with Nitsche's method:

Find $\boldsymbol{u} \in \mathcal{U}$ for all $\delta\boldsymbol{u} \in \mathcal{V}$ such that

$$\begin{aligned}
\delta\Pi = & \int_\Omega \delta\hat{\varepsilon}_{ij} \sigma_{ij} \, \mathrm{d}\Omega + \sum_m \int_{\Omega^{(m)}} H^{(m)} \delta\tilde{\varepsilon}_{ij}^{(m)} \sigma_{ij}^{(m)} \, \mathrm{d}\Omega + \alpha \int_{\Gamma_*} [\![\delta u_i]\!] n_i n_j [\![u_j]\!] \, \mathrm{d}\Gamma \\
& - \int_{\Gamma_*} [\![\delta u_i]\!] n_i n_j \langle \sigma(\boldsymbol{u})_{jk} \rangle n_k \, \mathrm{d}\Gamma - \int_{\Gamma_*} [\![u_i]\!] n_i n_j \langle \sigma(\delta\boldsymbol{u})_{jk} \rangle n_k \, \mathrm{d}\Gamma \\
& - \int_\Omega \delta\hat{u}_i b_i \, \mathrm{d}\Omega - \sum_m \int_{\Omega^{(m)}} H^{(m)} \delta\tilde{u}_i^{(m)} b_i^{(m)} \, \mathrm{d}\Omega \\
& - \int_{\Gamma_\sigma} \delta\hat{u}_i h_i \, \mathrm{d}\Gamma - \sum_m \int_{\Gamma_\sigma^{(m)}} H^{(m)} \delta\tilde{u}_i^{(m)} h_i^{(m)} \, \mathrm{d}\Gamma = 0
\end{aligned} \tag{5.10}$$

The stability properties and the remarks regarding the choice of the stabilization parameter stay the same as for the fully tied problem.

5.3 Discretization

The discretizations for the frictionless sliding problem can be derived in a similar manner, but it is not done as extensively as it has been done for the fully tied problem since the principles remain the same. The discrete representation of the bulk field is again adopted from the untied problem. So, only the contributions due to the interfacial constraints are considered here. The approximations (3.7), (3.8), (4.38) and (4.39) are used again. It has been shown in the previous sections that it is sufficient to provide expressions for element residuals and their linearizations since the global quantities are obtained obtained via an assembly process which is not affected by the interfacial constraints. The element residuals and their linearizations for the frictionless sliding problem will be presented for Lagrange mulitpliers, penalty method and Nitsche's method in the following subsections.

5.3.1 Lagrange multipliers

Discretizing the first variation of the potential (5.4) leads to:

$$\delta\Pi^{Lag} \approx \sum_{e=1}^{cutnumele} \left\{ \delta\tilde{\boldsymbol{d}}^T \int_{\Gamma_*^{(e)}} [\![\tilde{\boldsymbol{N}}]\!]^T \boldsymbol{n}\boldsymbol{n}^T \boldsymbol{\lambda}^h \,\mathrm{d}\Gamma + \delta\bar{\boldsymbol{\lambda}}^T \int_{\Gamma_*^{(e)}} \bar{\boldsymbol{N}}^T \boldsymbol{n}\boldsymbol{n}^T [\![\boldsymbol{u}^h]\!] \,\mathrm{d}\Gamma \right\} \tag{5.11}$$

Using the arbitrariness of the variations and considering the assembly process, a Lagrange multiplier contribution to the elementary residual, $\boldsymbol{r}^{Lag,(e)}$, can be expressed:

$$\boldsymbol{r}^{Lag,(e)} = \begin{bmatrix} \boldsymbol{0}_{6\times 1} \\ \int_{\Gamma_*^{(e)}} [\![\tilde{\boldsymbol{N}}]\!]^T \boldsymbol{n}\boldsymbol{n}^T \boldsymbol{\lambda}^h \,\mathrm{d}\Gamma \\ \int_{\Gamma_*^{(e)}} \bar{\boldsymbol{N}}^T \boldsymbol{n}\boldsymbol{n}^T [\![\boldsymbol{u}^h]\!] \,\mathrm{d}\Gamma \end{bmatrix} \tag{5.12}$$

The global contribution to the global residual can be assembled following (4.43). The linearization of the element residual leads to an expression similar to (4.46):

$$\Delta\boldsymbol{r}^{(e)} = \begin{bmatrix} \frac{\partial \boldsymbol{r}^{(e)}}{\partial \boldsymbol{d}} \\ \frac{\partial \boldsymbol{r}^{(e)}}{\partial \boldsymbol{\lambda}} \end{bmatrix} \begin{bmatrix} \Delta\boldsymbol{d} \\ \Delta\boldsymbol{\lambda} \end{bmatrix} = \begin{bmatrix} \boldsymbol{k}^{u,(e)} & \boldsymbol{g}^{\lambda,(e)} \\ \boldsymbol{g}^{d} & \boldsymbol{0} \end{bmatrix} \begin{bmatrix} \Delta\boldsymbol{d}, (\boldsymbol{e}) \\ \Delta\boldsymbol{\lambda} \end{bmatrix} \tag{5.13}$$

with the submatrices

$$\begin{aligned} \boldsymbol{g}^{\lambda,(e)} &= \int_{\Gamma_*^{(e)}} [\![\tilde{\boldsymbol{N}}]\!]^T \boldsymbol{n}\boldsymbol{n}^T \bar{\boldsymbol{N}} \,\mathrm{d}\Gamma \\ \boldsymbol{g}^{d,(e)} &= \int_{\Gamma_*^{(e)}} \bar{\boldsymbol{N}}^T \boldsymbol{n}\boldsymbol{n}^T [\![\tilde{\boldsymbol{N}}]\!] \,\mathrm{d}\Gamma \end{aligned} \tag{5.14}$$

where $\boldsymbol{g}^{d,(e)} = \boldsymbol{g}^{\lambda,(e)^T}$ provides the symmetry of the stiffness matrix. The typical structure of the tangent stiffness matrix as indicated in (4.48) is preserved, of course.

5.3.2 Penalty method

Inserting the discretizations (3.7) and (3.8) into the variation of the penalty potential for frictionless sliding (5.7) yields:

$$\delta\Pi^{pen} \approx \sum_{e=1}^{cutnumele} \delta\tilde{\boldsymbol{d}}^T \alpha \int_{\Gamma_*^{(e)}} [\![\tilde{\boldsymbol{N}}]\!]^T \boldsymbol{n}\boldsymbol{n}^T [\![\boldsymbol{u}^h]\!] \,\mathrm{d}\Gamma \tag{5.15}$$

From the discretized variational problem, the elementary penalty contribution to the residual can be extracted:

$$\boldsymbol{r}^{pen,(e)} = \begin{bmatrix} \mathbf{0}_{6\times 1} \\ \alpha \int_{\Gamma_*^{(e)}} [\![\tilde{\boldsymbol{N}}]\!]^T \boldsymbol{n}\boldsymbol{n}^T [\![\boldsymbol{u}^h]\!] \,\mathrm{d}\Gamma \end{bmatrix} \tag{5.16}$$

This residual is equal to the normal counterpart in (4.50) of the fully tied problem after introducing the decomposition into normal and tangential direction. A global contribution to the global residual can be assembled following (4.51). Using the linearity of the assembly operator and considering (4.53), element stiffness contributions with the same structure as for the fully tied problem can be defined:

$$\boldsymbol{k}^{pen,(e)} = \begin{bmatrix} \mathbf{0}_{6\times 6} & \mathbf{0}_{6\times 6} \\ \mathbf{0}_{6\times 6} & \boldsymbol{\kappa}_{22}^{pen,(e)} \end{bmatrix} \tag{5.17}$$

For the frictionless sliding problem, the submatrix, $\boldsymbol{\kappa}_{22}^{pen,(e)}$, takes the form:

$$\boldsymbol{\kappa}_{22}^{pen,(e)} = \alpha \int_{\Gamma_*^{(e)}} [\![\tilde{\boldsymbol{N}}]\!]^T \boldsymbol{n}\boldsymbol{n}^T [\![\tilde{\boldsymbol{N}}]\!] \mathrm{d}\Gamma \tag{5.18}$$

Again, this equals the normal counterpart in (4.55) after introducing the decomposition into normal and tangential direction.

5.3.3 Nitsche's method

As seen in the two previous sections, the discretization for the frictionless sliding problem results in very similar expressions as the one of the fully tied problem. The same is valid for Nitsche's method. The matrix $\check{\boldsymbol{n}}$ from (4.57) is used here, too. Inserting the discretization into the variation of the Nitsche potential for frictionless sliding (5.9) yields:

$$\begin{aligned} \delta\Pi^{Nit} \approx & \sum_{e=1}^{cutnumele} \left\{ \delta\tilde{\boldsymbol{d}}^T \alpha \int_{\Gamma_*^{(e)}} [\![\tilde{\boldsymbol{N}}]\!]^T \boldsymbol{n}\boldsymbol{n}^T [\![\boldsymbol{u}^h]\!] \,\mathrm{d}\Gamma - \delta\tilde{\boldsymbol{d}}^T \int_{\Gamma_*^{(e)}} [\![\tilde{\boldsymbol{N}}]\!]^T \boldsymbol{n}\boldsymbol{n}^T \check{\boldsymbol{n}} \langle \boldsymbol{\sigma}^h \rangle \,\mathrm{d}\Gamma \right\} \\ & - \sum_{e=1}^{cutnumele} \left\{ \delta\hat{\tilde{\boldsymbol{d}}}^T \int_{\Gamma_*^{(e)}} \langle \boldsymbol{C}\hat{\boldsymbol{B}} \rangle^T \check{\boldsymbol{n}}^T \boldsymbol{n}\boldsymbol{n}^T [\![\boldsymbol{u}^h]\!] \,\mathrm{d}\Gamma \right\} \\ & - \sum_{e=1}^{cutnumele} \left\{ \delta\tilde{\boldsymbol{d}}^T \int_{\Gamma_*^{(e)}} \langle \boldsymbol{C}\tilde{\boldsymbol{B}} \rangle^T \check{\boldsymbol{n}}^T \boldsymbol{n}\boldsymbol{n}^T [\![\boldsymbol{u}^h]\!] \,\mathrm{d}\Gamma \right\} \end{aligned} \tag{5.19}$$

where the shorthand notation (4.62) is used again. From the discretized variational problem, the elementary Nitsche contribution to the residual is extracted:

$$\boldsymbol{r}^{Nit,(e)} = \begin{bmatrix} -\int_{\Gamma_*^{(e)}} \langle \boldsymbol{C}\hat{\boldsymbol{B}} \rangle^T \check{\boldsymbol{n}}^T \boldsymbol{n}\boldsymbol{n}^T [\![\boldsymbol{u}^h]\!] \, \mathrm{d}\Gamma \\ \int_{\Gamma_*^{(e)}} \alpha [\![\tilde{\boldsymbol{N}}]\!]^T \boldsymbol{n}\boldsymbol{n}^T [\![\boldsymbol{u}^h]\!] - [\![\tilde{\boldsymbol{N}}]\!]^T \boldsymbol{n}\boldsymbol{n}^T \check{\boldsymbol{n}} \langle \boldsymbol{\sigma}^{\boldsymbol{h}} \rangle - \langle \boldsymbol{C}\tilde{\boldsymbol{B}} \rangle^T \check{\boldsymbol{n}}^T \boldsymbol{n}\boldsymbol{n}^T [\![\boldsymbol{u}^h]\!] \, \mathrm{d}\Gamma \end{bmatrix} \tag{5.20}$$

A global contribution to the global residual can be assembled following (4.63). Using the linearity of the assembly operator and considering (4.65), element stiffness contributions with the same structure as for the fully tied problem are defined:

$$\boldsymbol{k}^{Nit,(e)} = \begin{bmatrix} \boldsymbol{0}_{6\times 6} & \boldsymbol{\kappa}_{12}^{Nit,(e)} \\ \boldsymbol{\kappa}_{21}^{Nit,(e)} & \boldsymbol{\kappa}_{22}^{Nit,(e)} \end{bmatrix} \tag{5.21}$$

with the submatrices

$$\begin{aligned} \boldsymbol{\kappa}_{12}^{Nit,(e)} &= -\int_{\Gamma_*^{(e)}} \langle \boldsymbol{C}\hat{\boldsymbol{B}} \rangle^T \check{\boldsymbol{n}}^T \boldsymbol{n}\boldsymbol{n}^T [\![\tilde{\boldsymbol{N}}]\!] \, \mathrm{d}\Gamma \\ \boldsymbol{\kappa}_{21}^{Nit,(e)} &= -\int_{\Gamma_*^{(e)}} [\![\tilde{\boldsymbol{N}}]\!]^T \boldsymbol{n}\boldsymbol{n}^T \check{\boldsymbol{n}} \langle \boldsymbol{C}\hat{\boldsymbol{B}} \rangle \, \mathrm{d}\Gamma \\ \boldsymbol{\kappa}_{22}^{Nit,(e)} &= \alpha \int_{\Gamma_*^{(e)}} [\![\tilde{\boldsymbol{N}}]\!]^T \boldsymbol{n}\boldsymbol{n}^T [\![\tilde{\boldsymbol{N}}]\!] \mathrm{d}\Gamma - \int_{\Gamma_*^{(e)}} [\![\tilde{\boldsymbol{N}}]\!]^T \boldsymbol{n}\boldsymbol{n}^T \check{\boldsymbol{n}} \langle \boldsymbol{C}\tilde{\boldsymbol{B}} \rangle \, \mathrm{d}\Gamma \\ &\quad - \int_{\Gamma_*^{(e)}} \langle \boldsymbol{C}\tilde{\boldsymbol{B}} \rangle^T \check{\boldsymbol{n}}^T \boldsymbol{n}\boldsymbol{n}^T [\![\tilde{\boldsymbol{N}}]\!] \, \mathrm{d}\Gamma \end{aligned} \tag{5.22}$$

As in the fully tied problem, the last two terms in $\boldsymbol{\kappa}_{22}^{Nit,(e)}$ are the transpose of each other as well as $\boldsymbol{\kappa}_{12}^{Nit,(e)} = \boldsymbol{\kappa}_{21}^{Nit,(e)^T}$.

6 Perfect plasticity in tangential direction

In order to be able to model real physics better than with no or frictionless sliding, a combination of a linear elastic bulk field with an embedded interface that is governed by a plasticity law is introduced, following [44]. The interface is subjected to a rate-independent perfect plasticity law in tangential direction, whereby the behavior in normal direction is adopted from the previous cases. Now it is obvious, why the nonlinear framework and the decomposition into normal and tangential direction was used also for the purely elastic problems. The integration of the rate-indepentent elasto-plastic model uses a *return-mapping algorithm* proposed in [35]. First of all, the admissible kinematics and tractions at the interface are described. Then, the equations used in the return-mapping algorithm are developed for the penalty method and a stabilized method, inspired by Nitsche's method. Afterwards, the weak forms are presented, which finally are discretized, leading to expressions for the residual and stiffness contributions. The return-mapping algorithm itself is shown in section 8.4.

6.1 Constraints for kinematics and tractions

Here, the behavior in normal and tangential direction of the interface is decoupled. The kinematics in normal direction are governed by the same constraint (5.1) as in the frictionless sliding problem:

$$[\![u_i]\!] n_i \doteq 0 \text{ on } \Gamma_* \tag{6.1}$$

The tractions in normal direction can be assigned from one grain to the other as in the frictionless sliding problem:

$$n_i \sigma_{ij}^{(1)} n_j^{(1)} + n_i \sigma_{ij}^{(2)} n_j^{(2)} = 0 \text{ on } \Gamma_* \tag{6.2}$$

The kinematics in tangential direction are not constrained primarily, but they have to be determined by the traction law in tangential direction. The equations for perfect plasticity at the interface can be presented on the basis of either a plasticity background [35] or a frictional contact background [24].

Remark 6.1. *The fact, that the normal constraints are the same as in the frictionless sliding problem from section 5 implies, that all equations from the frictionless sliding problem hold*

here, too. From an implementational perspective, the normal constraints can be applied using the methods for frictionless sliding. The tangential constraints have to be treated separetely, of course.

Remark 6.2. *The problem considered in this work has two dimensions. Though, plastic behavior occurs only in the tangential direction of the interface. Hence, a one-dimensional plasticity law is sufficient. The adaptation in dimensionality can be done by introducing a reference frame which is attached to the interface. A similar procedure is used in a frictional contact context [24], which is also based on [35].*

It has been shown in [26], that perfect plasticity and frictional contact are described by a similar set of equations. Following the theory of rate-independent plasticity [35] as well as of frictional contact [23], the model is governed by so-called *loading/unloading conditions* which can be expressed as *Kuhn-Tucker conditions*. According to [35], the constitutive model for perfect plasticity can be summarized with the following five equations:

$$
\begin{aligned}
&\text{Traction law:} && \underline{\boldsymbol{h}}_t^* = f(\underline{\boldsymbol{u}}) \\
&\text{Flow rule:} && [\![\dot{\underline{\boldsymbol{u}}}]\!]_t^{pl} = -\gamma \frac{\underline{\boldsymbol{h}}_t^*}{\|\underline{\boldsymbol{h}}_t^*\|} \\
&\text{Yield condition:} && \Phi = \|\underline{\boldsymbol{h}}_t^*\| - h_t^y \leq 0 \\
&\text{Kuhn-Tucker complementarity condition:} && \Phi \leq 0,\ \gamma \geq 0,\ \gamma\Phi = 0 \\
&\text{Consistency condition:} && \gamma\dot{\Phi} = 0 \,(\text{if } \Phi = 0)
\end{aligned}
\tag{6.3}
$$

The traction law has to be specified for each method and gives a rule how to compute the tangential traction based on the displacement field. The flow rule claims that slip occurs in the same direction as the applied traction with γ being the absolute value of the slip rate. Due to the existence of a yield traction, h_t^y, which can be seen as an equivalent to a yield stress, the absolute value of the tangential traction cannot be greater than the yield traction. This fact is expressed by the yield condition. The Kuhn-Tucker conditions state, that either the yield condition or the consistency parameter, γ, has to be zero, which means, that plastic slip can only occur if the absolute value of the tangential traction is greater than the yield traction, h_t^y. Otherwise, there cannot be plastic slip, if the absolute value of the tangential traction is less or equal than the yield traction. Finally, the consistency condition corresponds to the physical requirement that for a non-zero slip rate $\gamma > 0$ the traction is limited to the yield traction such that $\dot{\Phi} = 0$.

Remark 6.3. *As stated above, the following equations can be derived from a plasticity point of view [35] or a frictional contact point of view [23]. When considering the plasticity context, the yield traction equals the yield stress. In a frictional contact context, the tangential yield "traction" depends on the normal pressure and the Coulomb friction coefficent [23].*

Remark 6.4. *A closer look at the yield condition shows, that the fully tied problem is covered by the perfect plasticity case, if the yield stress is high enough, such that no part of the interface gets into slip. The frictionless sliding problem is covered, if the yield traction is chosen as zero. This is also shown in the numerical examples in section 9.3. This relationship between the method is summarized in figure 6.1*

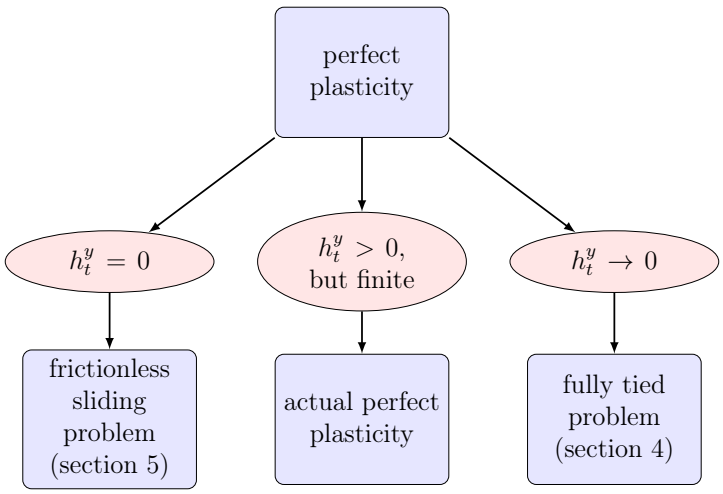

FIGURE 6.1: Relationship between the fully tied problem, the frictionless sliding problem and perfect plasticity

6.2 Return-mapping equations

The traction laws for perfect plasticity in tangential direction are now presented for the penalty method and the stabilized method. The rate equations are integrated using a backward Euler scheme leading to the classical return-mapping algorithm [35]. Here, only the equations for the return-mapping algorithm are presented. The algorithmic framework itself is presented in section 8.4. For the penalty method, the developement of the equations for the return-mapping algorithm is explained in detail, whereas for the stabilized method only the equations are given since the steps and applied transformations are the same. Also, the linearizations are given in order to prepare the derivation of the stiffnes contributions.

6.2.1 Penalty method

For the penalty method, the traction in tangential direction is computed using the tangential penalty parameter, α_t:

$$\underline{\boldsymbol{h}}_t^* = -\alpha_t [\![\underline{\boldsymbol{u}}]\!]_t^{el} = -\alpha_t \left([\![\underline{\boldsymbol{u}}]\!]_t - [\![\underline{\boldsymbol{u}}]\!]_t^{pl} \right) \tag{6.4}$$

where the index t denotes the projection onto the tangential direction. Applying a backward Euler scheme to the flow rule in (6.3) yields an update formula to compute the plastic part of the tangential jump at the pseudo-time step $k+1$. It is based on the known plastic part of the tangential jump at pseudo-time step k and its derivative which has to be evaluated at the new pseudo-time step:

$$[\![\underline{\boldsymbol{u}}]\!]_{t,k+1}^{pl} - [\![\underline{\boldsymbol{u}}]\!]_{t,k}^{pl} = -\xi \frac{\underline{\boldsymbol{h}}_{t,k+1}^*}{\|\underline{\boldsymbol{h}}_{t,k+1}^*\|} \tag{6.5}$$

Here, $\xi \geq 0$ denotes the product of γ with an increment in pseudo-time, $\xi = \gamma \, \Delta t$. It can be seen as a Lagrange multiplier [35] and represents the algorithmic counterpart of the consistency parameter $\gamma \geq 0$. The traction at the new pseudo-time step is computed as:

$$\underline{\boldsymbol{h}}_{t,k+1}^* = -\alpha_t \left([\![\underline{\boldsymbol{u}}]\!]_{t,k+1} - [\![\underline{\boldsymbol{u}}]\!]_{t,k+1}^{pl} \right) \tag{6.6}$$

It is constrained by the following discrete version of the Kuhn-Tucker conditions:

$$\begin{aligned} &\Phi_{k+1} = \|\underline{\boldsymbol{h}}_{t,k+1}^*\| - h_t^y \leq 0 \\ &\xi \geq 0 \\ &\xi \Phi_{k+1} = 0 \end{aligned} \tag{6.7}$$

Following the procedure in [35], first an auxiliary state is considered, which does not need to correspond to an actual state as shown below, and is obtained by freezing the plastic flow. It means, that a purely elastic step is assumed which leads to the so-called *trial state*:

$$\underline{\boldsymbol{h}}_{t,k+1}^{*,trial} = -\alpha_t \left([\![\underline{\boldsymbol{u}}]\!]_{t,k+1} - [\![\underline{\boldsymbol{u}}]\!]_{t,k}^{pl} \right) \equiv \underline{\boldsymbol{h}}_{t,k}^* - \alpha_t \left([\![\underline{\boldsymbol{u}}]\!]_{t,k+1} - [\![\underline{\boldsymbol{u}}]\!]_{t,k} \right) \tag{6.8}$$

The second equivalence in (6.8) is obtained by adding and subtracting $[\![\underline{\boldsymbol{u}}]\!]_{t,k}$ and identifying the known traction at the end of the previous pseudo-time step. The trial state is thus determined solely in terms of the known state and a given displacement incre-

ment, $[\![\underline{\boldsymbol{u}}]\!]_{t,k+1} - [\![\underline{\boldsymbol{u}}]\!]_{t,k}$. The reader may observe that the plastic part of the tangential jump from the previous pseudo-time step is used, i.e. it is assumed that this step produces no additional plastic deformation. It follows that the plastic part of the tangential jump for the trial state is adopted from the previous pseudo-time step:

$$[\![\underline{\boldsymbol{u}}]\!]^{pl,trial}_{t,k+1} = [\![\underline{\boldsymbol{u}}]\!]^{pl}_{t,k} \tag{6.9}$$

The yield condition can be evaluated for the trial state, too:

$$\Phi\left(\underline{\boldsymbol{h}}^{*,trial}_{t,k+1}\right) = \Phi^{trial}_{k+1} = \|\underline{\boldsymbol{h}}^{*,trial}_{t,k+1}\| - h^y_t \tag{6.10}$$

As mentioned above, the trial state does not need to correspond to an actual state, although it is possible. This depends on the loading conditions. First, the case with $\Phi^{trial}_{k+1} \leq 0$ is considered. It follows that the trial state is an admissible state and the trial quantities are the actual quantities:

$$\begin{aligned} \underline{\boldsymbol{h}}^{*}_{t,k+1} &= \underline{\boldsymbol{h}}^{*,trial}_{t,k+1} \\ [\![\underline{\boldsymbol{u}}]\!]^{pl}_{t,k+1} &= [\![\underline{\boldsymbol{u}}]\!]^{pl,trial}_{t,k+1} \end{aligned} \tag{6.11}$$

Now, the case with $\Phi^{trial}_{k+1} > 0$ is investigated. Clearly, the trial state cannot be an actual state since it violates the constraint condition $\Phi \leq 0$. Thus, it is required that $\xi > 0$ such that $[\![\underline{\boldsymbol{u}}]\!]^{pl}_{t,k+1} \neq [\![\underline{\boldsymbol{u}}]\!]^{pl}_{t,k}$ and $\underline{\boldsymbol{h}}^{*}_{t,k+1} \neq \underline{\boldsymbol{h}}^{*,trial}_{t,k+1}$. The algorithmic consistency parameter $\xi > 0$ assures that the yield condition holds since, according to (6.7), Φ has to be zero if ξ is unequal to zero. This process is thus incrementally plastic. The distinction between an elastic and a plastic step can be summarized as:

$$\Phi^{trial}_{k+1} \begin{cases} \leq 0 & \Rightarrow \text{ elastic step:} \quad \xi = 0 \\ > 0 & \Rightarrow \text{ plastic step:} \quad \xi > 0 \end{cases} \tag{6.12}$$

The next step is to examine the algorithmic problem for an incrementally plastic step. Therefor, the final traction, $\underline{\boldsymbol{h}}^{*}_{t,k+1}$, can be expressed in terms of the trial state, $\underline{\boldsymbol{h}}^{*,trial}_{t,k+1}$, and

the algorithmic consistency parameter, ξ:

$$\begin{aligned}\underline{\boldsymbol{h}}^{*}_{t,k+1} &= -\alpha_t \left([\![\underline{\boldsymbol{u}}]\!]_{t,k+1} - [\![\underline{\boldsymbol{u}}]\!]^{pl}_{t,k+1} \right) \\ &= -\alpha_t \left([\![\underline{\boldsymbol{u}}]\!]_{t,k+1} - [\![\underline{\boldsymbol{u}}]\!]^{pl}_{t,k} \right) - \alpha_t \left([\![\underline{\boldsymbol{u}}]\!]^{pl}_{t,k} - [\![\underline{\boldsymbol{u}}]\!]^{pl}_{t,k+1} \right) \\ &= \underline{\boldsymbol{h}}^{*,trial}_{t,k+1} - \alpha_t \, \xi \frac{\underline{\boldsymbol{h}}^{*}_{t,k+1}}{\| \underline{\boldsymbol{h}}^{*}_{t,k+1} \|}\end{aligned} \tag{6.13}$$

Here, $[\![\underline{\boldsymbol{u}}]\!]^{pl}_{t,k}$ was added and subtracted and (6.8) as well as (6.5) were used. From the result of (6.13) follows:

$$\| \underline{\boldsymbol{h}}^{*}_{t,k+1} \| \frac{\underline{\boldsymbol{h}}^{*}_{t,k+1}}{\| \underline{\boldsymbol{h}}^{*}_{t,k+1} \|} = \| \underline{\boldsymbol{h}}^{*,trial}_{t,k+1} \| \frac{\underline{\boldsymbol{h}}^{*,trial}_{t,k+1}}{\| \underline{\boldsymbol{h}}^{*,trial}_{t,k+1} \|} - \alpha_t \, \xi \frac{\underline{\boldsymbol{h}}^{*}_{t,k+1}}{\| \underline{\boldsymbol{h}}^{*}_{t,k+1} \|} \tag{6.14}$$

which can be rewritten as:

$$\left(\| \underline{\boldsymbol{h}}^{*}_{t,k+1} \| + \alpha_t \, \xi \right) \frac{\underline{\boldsymbol{h}}^{*}_{t,k+1}}{\| \underline{\boldsymbol{h}}^{*}_{t,k+1} \|} = \| \underline{\boldsymbol{h}}^{*,trial}_{t,k+1} \| \frac{\underline{\boldsymbol{h}}^{*,trial}_{t,k+1}}{\| \underline{\boldsymbol{h}}^{*,trial}_{t,k+1} \|} \tag{6.15}$$

Since $\alpha_t > 0$ as well as $\xi > 0$, it holds that:

$$\frac{\underline{\boldsymbol{h}}^{*}_{t,k+1}}{\| \underline{\boldsymbol{h}}^{*}_{t,k+1} \|} = \frac{\underline{\boldsymbol{h}}^{*,trial}_{t,k+1}}{\| \underline{\boldsymbol{h}}^{*,trial}_{t,k+1} \|} \tag{6.16}$$

along with the condition:

$$\| \underline{\boldsymbol{h}}^{*}_{t,k+1} \| + \alpha_t \, \xi = \| \underline{\boldsymbol{h}}^{*,trial}_{t,k+1} \| \tag{6.17}$$

So far, the value of the algorithmic consistency parameter, ξ, is not determined, yet. This can be done by looking at the discrete consistency condition. Using (6.17) yields:

$$\Phi_{k+1} = \| \underline{\boldsymbol{h}}^{*}_{t,k+1} \| - h^{y}_{t} = \| \underline{\boldsymbol{h}}^{*,trial}_{t,k+1} \| - \alpha_t \, \xi - h^{y}_{t} = \Phi^{trial}_{k+1} - \alpha_t \, \xi \doteq 0 \tag{6.18}$$

Hence, the algorithmic consistency parameter can be computed as:

$$\xi = \frac{\Phi^{trial}_{k+1}}{\alpha_t} \tag{6.19}$$

Finally, the actual state for an incrementally plastic step can be computed via:

$$\begin{aligned} \underline{\boldsymbol{h}}^{*}_{t,k+1} &= \left(1 - \frac{\alpha_t \, \xi}{\|\underline{\boldsymbol{h}}^{*,trial}_{t,k+1}\|}\right) \underline{\boldsymbol{h}}^{*,trial}_{t,k+1} \\ [\![\underline{\boldsymbol{u}}]\!]^{pl}_{t,k+1} &= [\![\underline{\boldsymbol{u}}]\!]^{pl}_{t,k} - \xi \frac{\underline{\boldsymbol{h}}^{*,trial}_{t,k+1}}{\|\underline{\boldsymbol{h}}^{*,trial}_{t,k+1}\|} \end{aligned} \tag{6.20}$$

where (6.16) is used. Now, all equations are known which are needed to apply the return-mapping algorithm. Here, a brief summary is given in order to prepare the presentation of the algorithm in section 8.4: A trial state, which is assumed to be purely elastic, can be computed using (6.8) and (6.9). The evalutation of the yield condition for the trial state determines whether the step is elastic or plastic, see (6.12). For an elastic step, the trial state is the actual state. For a plastic step, the trial state has to be corrected using (6.19) and (6.20) in order to satisfy the consistency condition $\Phi \leq 0$.
The expression for the tangential traction is now linearized in order to prepare the derivation of the stiffness contributions in section 6.4.1. The linearization of the trial state is denoted with $\Delta \boldsymbol{h}^{*,trial}_{t,k+1}$. A second expression, which will be needed later, is the linearization of the algorithmic consistency parameter, $\Delta\xi$:

$$\Delta\xi = \Delta \frac{\Phi^{trial}_{k+1}}{\alpha_t} = \frac{1}{\alpha_t} \Delta \|\underline{\boldsymbol{h}}^{*,trial}_{t,k+1}\| = \frac{1}{\alpha_t} \frac{\underline{\boldsymbol{h}}^{*,trial}_{t,k+1}}{\|\underline{\boldsymbol{h}}^{*,trial}_{t,k+1}\|} \Delta \underline{\boldsymbol{h}}^{*,trial}_{t,k+1} \tag{6.21}$$

The linearization of the tangential traction can then be given, depending whether $\Phi^{trial}_{k+1} \leq 0$ or $\Phi^{trial}_{k+1} > 0$. If $\Phi^{trial}_{k+1} \leq 0$, then the linearization of the tangential traction is equal to the linearization of the tangential traction in the trial state:

$$\Delta \boldsymbol{h}^{*}_{t,k+1} = \Delta \boldsymbol{h}^{*,trial}_{t,k+1} \tag{6.22}$$

But if $\Phi_{k+1}^{trial} > 0$, the linearization of the tangential traction can be obtained by linearizing $\boldsymbol{h}_{t,k+1}^{*}$ in (6.20):

$$\begin{aligned}
\Delta\underline{\boldsymbol{h}}_{t,k+1}^{*} &= \Delta\left(1-\frac{\alpha_t\,\xi}{\|\underline{\boldsymbol{h}}_{t,k+1}^{*,trial}\|}\right)\underline{\boldsymbol{h}}_{t,k+1}^{*,trial} + \left(1-\frac{\alpha_t\,\xi}{\|\underline{\boldsymbol{h}}_{t,k+1}^{*,trial}\|}\right)\Delta\underline{\boldsymbol{h}}_{t,k+1}^{*,trial} \\
&= \quad -\Delta\left(\frac{\alpha_t\,\xi}{\|\underline{\boldsymbol{h}}_{t,k+1}^{*,trial}\|}\right)\underline{\boldsymbol{h}}_{t,k+1}^{*,trial} + \left(1-\frac{\alpha_t\,\xi}{\|\underline{\boldsymbol{h}}_{t,k+1}^{*,trial}\|}\right)\Delta\underline{\boldsymbol{h}}_{t,k+1}^{*,trial} \\
&= -\alpha_t\frac{\underline{\boldsymbol{h}}_{t,k+1}^{*,trial}}{\|\underline{\boldsymbol{h}}_{t,k+1}^{*,trial}\|}\Delta\xi + \frac{\alpha_t\,\xi}{\|\underline{\boldsymbol{h}}_{t,k+1}^{*,trial}\|}\Delta\underline{\boldsymbol{h}}_{t,k+1}^{*,trial} + \Delta\underline{\boldsymbol{h}}_{t,k+1}^{*,trial} - \frac{\alpha_t\,\xi}{\|\underline{\boldsymbol{h}}_{t,k+1}^{*,trial}\|}\Delta\underline{\boldsymbol{h}}_{t,k+1}^{*,trial} \\
&= 0
\end{aligned} \tag{6.23}$$

The first line follows from the product rule, the third line from the quotient rule. Inserting (6.21) into the third line yields, that the linearization for a plastic step is equal to zero. The linearization can be summarized as follows:

$$\Delta\underline{\boldsymbol{h}}_{t,k+1}^{*} = \begin{cases} \Delta\underline{\boldsymbol{h}}_{t,k+1}^{*,trial} & \text{if } \Phi_{k+1}^{trial} \leq 0 \\ 0 & \text{if } \Phi_{k+1}^{trial} > 0 \end{cases} \tag{6.24}$$

$\Delta\underline{\boldsymbol{h}}_{t,k+1}^{*,trial}$ will be specified after introducing the discretization.

6.2.2 Stabilized method inspired by Nitsche's method

For the stabilized method, the reconstruction of the traction field along the interface is inspired by Nitsche's method and is adopted from (4.35):

$$\underline{\boldsymbol{h}}_{t}^{*} = -\alpha_t[\![\underline{\boldsymbol{u}}]\!]_t^{el} + [\langle\underline{\boldsymbol{\sigma}}\rangle\underline{\boldsymbol{n}}]_t = -\left(\underline{\boldsymbol{I}}_{2\times2} - \underline{\boldsymbol{n}}\otimes\underline{\boldsymbol{n}}\right)\left(\alpha_t[\![\underline{\boldsymbol{u}}]\!]^{el} - \langle\underline{\boldsymbol{\sigma}}\rangle\underline{\boldsymbol{n}}\right) \tag{6.25}$$

with the identity matrix $\underline{\boldsymbol{I}}_{2\times2}$. Applying the backward Euler scheme yields the same results as for the penalty metod:

$$[\![\underline{\boldsymbol{u}}]\!]_{t,k+1}^{pl} - [\![\underline{\boldsymbol{u}}]\!]_{t,k}^{pl} = -\xi\frac{\underline{\boldsymbol{h}}_{t,k+1}^{*}}{\|\underline{\boldsymbol{h}}_{t,k+1}^{*}\|} \tag{6.26}$$

The traction at the new pseudo-time step is computed as:

$$\underline{\boldsymbol{h}}_{t,k+1}^{*} = -\alpha_t\left([\![\underline{\boldsymbol{u}}]\!]_{t,k+1} - [\![\underline{\boldsymbol{u}}]\!]_{t,k+1}^{pl}\right) + [\langle\underline{\boldsymbol{\sigma}}\rangle\underline{\boldsymbol{n}}]_{t,k+1} \tag{6.27}$$

It is constrained by the following discrete version of the Kuhn-Tucker conditions:

$$\begin{aligned} &\Phi_{k+1} = \|\underline{\boldsymbol{h}}^*_{t,k+1}\| - h^y_t \leq 0 \\ &\xi \geq 0 \\ &\xi \Phi_{k+1} = 0 \end{aligned} \tag{6.28}$$

Assuming an purely elastic step, the trial state is computed as:

$$\begin{aligned} \underline{\boldsymbol{h}}^{*,trial}_{t,k+1} &= -\alpha_t \left([\![\underline{\boldsymbol{u}}]\!]_{t,k+1} - [\![\underline{\boldsymbol{u}}]\!]^{pl}_{t,k} \right) + [\langle \underline{\boldsymbol{\sigma}} \rangle \underline{\boldsymbol{n}}]_{t,k+1} \\ &\equiv \underline{\boldsymbol{h}}^*_{t,k} - \alpha_t \left([\![\underline{\boldsymbol{u}}]\!]_{t,k+1} - [\![\underline{\boldsymbol{u}}]\!]_{t,k} \right) + \left([\langle \underline{\boldsymbol{\sigma}} \rangle \underline{\boldsymbol{n}}]_{t,k+1} - [\langle \underline{\boldsymbol{\sigma}} \rangle \underline{\boldsymbol{n}}]_{t,k} \right) \end{aligned} \tag{6.29}$$

The contribution of the averaged stress stems from the bulk field and hence is not influenced by the plastic contribution to the tangential jump in the displacement field. The plastic contribution to the tangential jump in the displacement field for the trial state can be adopted from (6.9). The evaluation of the yield condition for the trial state is done as in (6.10) for the penalty method as well as the distinction between an elastic and a plastic step (6.12), since these steps are independent from the method since they are given by the return-mapping framework. If the current step is an elastic step in the sense of (6.12), the trial quantities are adopted for the actual state as in (6.11). If the step is a plastic step in the sense of (6.12), the actual state can be computed as a correction of the trial state. A similar observation as in (6.13) can also be made for the stabilized method such that the traction at the new pseudo-time step is expressed in terms of the trial state, $\underline{\boldsymbol{h}}^{*,trial}_{t,k+1}$, and the algorithmic consistency parameter, ξ:

$$\begin{aligned} \underline{\boldsymbol{h}}^*_{t,k+1} &= -\alpha_t \left([\![\underline{\boldsymbol{u}}]\!]_{t,k+1} - [\![\underline{\boldsymbol{u}}]\!]^{pl}_{t,k+1} \right) + [\langle \underline{\boldsymbol{\sigma}} \rangle \underline{\boldsymbol{n}}]_{t,k+1} \\ &= -\alpha_t \left([\![\underline{\boldsymbol{u}}]\!]_{t,k+1} - [\![\underline{\boldsymbol{u}}]\!]^{pl}_{t,k} \right) + [\langle \underline{\boldsymbol{\sigma}} \rangle \underline{\boldsymbol{n}}]_{t,k+1} - \alpha_t \left([\![\underline{\boldsymbol{u}}]\!]^{pl}_{t,k} - [\![\underline{\boldsymbol{u}}]\!]^{pl}_{t,k+1} \right) \\ &= \underline{\boldsymbol{h}}^{*,trial}_{t,k+1} - \alpha_t \, \xi \frac{\underline{\boldsymbol{h}}^*_{t,k+1}}{\|\underline{\boldsymbol{h}}^*_{t,k+1}\|} \end{aligned} \tag{6.30}$$

Following the procedure as shown for the penalty method, (6.14), (6.15), (6.16) and (6.17) can be applied here, too. Then, the algorithmic consistency parameter can be computed by looking at the discrete consistency condition. Using (6.17) yields:

$$\Phi_{k+1} = \|\underline{\boldsymbol{h}}^*_{t,k+1}\| - h^y_t = \|\underline{\boldsymbol{h}}^{*,trial}_{t,k+1}\| - \alpha_t \, \xi - h^y_t = \Phi^{trial}_{k+1} - \alpha_t \, \xi \doteq 0 \tag{6.31}$$

The algorithmic consistency parameter can thus be computed as:

$$\xi = \frac{\Phi_{k+1}^{trial}}{\alpha_t} \tag{6.32}$$

Finally, the actual state for an incrementally plastic step can be computed via:

$$\begin{aligned} \underline{\boldsymbol{h}}_{t,k+1}^{*} &= \left(1 - \frac{\alpha_t \, \xi}{\|\underline{\boldsymbol{h}}_{t,k+1}^{*,trial}\|}\right) \underline{\boldsymbol{h}}_{t,k+1}^{*,trial} \\ [\![\underline{\boldsymbol{u}}]\!]_{t,k+1}^{pl} &= [\![\underline{\boldsymbol{u}}]\!]_{t,k}^{pl} - \xi \frac{\underline{\boldsymbol{h}}_{t,k+1}^{*,trial}}{\|\underline{\boldsymbol{h}}_{t,k+1}^{*,trial}\|} \end{aligned} \tag{6.33}$$

where (6.16) is used. A comparison bewteen the equations for the penalty method and the stabilized method concludes that differences arise only in the traction law and in the computation of the trial state. Also here, a brief summary is given in order to prepare the presentation of the algorithm in section 8.4: A trial state, which is assumed to be purely elastic, can be computed using (6.29) and (6.9). The evalutation of the yield condition for the trial state determines whether the step is elastic or plastic, see (6.12). For an elastic step, the trial state is the actual state. For a plastic step, the trial state has to be corrected using (6.32) and (6.33) in order to satisfy the consistency condition $\Phi \leq 0$.
The linearization of the tangential traction has to be computed for the stabilized method as well. As mentioned above, the traction for the stabilized method is computed using the same formula as in the penalty case after expressing everything in terms of the trial state. The linearization of the traction is hence not presented in detail since it is exactly the same as for the penalty method. The result can be summarized as:

$$\Delta\underline{\boldsymbol{h}}_{t,k+1}^{*} = \begin{cases} \Delta\underline{\boldsymbol{h}}_{t,k+1}^{*,trial} & \text{if } \Phi_{k+1}^{trial} \leq 0 \\ 0 & \text{if } \Phi_{k+1}^{trial} > 0 \end{cases} \tag{6.34}$$

$\Delta\underline{\boldsymbol{h}}_{t,k+1}^{*,trial}$ will be specified after introducing the discretization.

Remark 6.5. *As seen during the derivation of the variational form for the fully tied problem, there are some similiarities and links between Nitsche's method and augmented Lagrangian formulations. Similarities between the stabilized method, presented here, and an augmented Lagrangian regularization for frictional contact [36] can also be found. An advantage of the Nitsche-like formulation over the pure augmented Lagrangian one is, that no additional*

update of the Lagrange multiplier is needed, since the Lagrange mulitplier is replaced by the averaged stress, that depends only on the displcament field. Hence no additional iterations have to be carried out.

6.3 Weak forms

Since the problem contains plastic contributions, it is not conservative anymore. Thus, a potential cannot be formulated and be used to state a variational problem. Hence, the *principle of the minimum of the total potential energy* cannot be applied anymore. However, since the bulk field is still assumed to behave following a linear elastic constitutive model and only the interfacial contributions are not conservative, the derivations done for the untied problem are still valid. Also the contributions from interfacial constraints in normal direction are not influenced by the plasticity law. Thus, they are still valid. Using the well known fact, that the principle of the minimum of the total potential energy ends up with an equivalent problem as the *method of weighted residuals* using *test functions*, allows to use the variational problem from the purely elastic problems and rewrite them, using a test function, w_i. The test function, w_i, takes a similar form as the enriched displacement field [33]:

$$w_i(\boldsymbol{x}) = \hat{w}_i(\boldsymbol{x}) + \sum_{m=1}^{2} H^{(m)}(\boldsymbol{x}) \tilde{w}_i^{(m)}(\boldsymbol{x}) \in \mathcal{W} \tag{6.35}$$

with $\mathcal{W}$ defined similar to (2.12):

$$\mathcal{W} = \{w_i(\boldsymbol{x}) | w_i(\boldsymbol{x}) \in H^1(\Omega), w_i(\boldsymbol{x}) = 0 \text{ on } \Gamma_d, w_i(\boldsymbol{x}) \text{ discontinous on } \Gamma_*\} \tag{6.36}$$

A closer look shows, that the parts, that can be adopted form the purely elastic cases, correspond to the frictionless sliding problem. Now, the variational problem for penalty method and Nitsche's method from the frictionless sliding problem can be rewritten using the test function, w_i. Finally, only the contributions for the tangential direction have to be derived again.

6.3.1 Penalty method

The weak form for the contributions from the bulk field and the normal constraints at the interface takes can be obtained by replacing the variation of the displacement field, δu_i, with the test function, w_i, in (5.8). The tangential contributions can be obtained by multiplying

the tangential tracion law (6.4) with a test function, w_i, followed by the integration over the embedded interface. Then, the weak form reads:

$$\begin{aligned}
&\int_\Omega \hat{w}_{i,j}\sigma_{ij}\,\mathrm{d}\Omega + \sum_m \int_{\Omega^{(m)}} H^{(m)}\tilde{w}_{i,j}^{(m)}\sigma_{ij}^{(m)}\,\mathrm{d}\Omega \\
&+ \alpha\int_{\Gamma_*} [\![w_i]\!] n_i n_j [\![u_j]\!]\,\mathrm{d}\Gamma - \int_{\Gamma_*} [\![w_i]\!] h_{t,i}^*\,\mathrm{d}\Gamma \\
&= \int_\Omega \hat{w}_i b_i\,\mathrm{d}\Omega + \sum_m \int_{\Omega^{(m)}} H^{(m)}\tilde{w}_i^{(m)} b_i^{(m)}\,\mathrm{d}\Omega \\
&+ \int_{\Gamma_\sigma} \hat{w}_i h_i\,\mathrm{d}\Gamma + \sum_m \int_{\Gamma_\sigma^{(m)}} H^{(m)}\tilde{w}_i^{(m)} h_i^{(m)}\,\mathrm{d}\Gamma
\end{aligned} \tag{6.37}$$

where the tangential traction, $h_{t,i}^*$, is subjected to the set of constraints in (6.3).

6.3.2 Stabilized method inspired by Nitsche's method

A similar procedure can be applied for the stabilized method. To enforce the constraints in normal direction, Nitsche's method is used. The tangential contributions can be obtained by multiplying the tangential traction law (6.25) with a test function, w_i, followed by the integration over the embedded interface. Then, the weak form reads:

$$\begin{aligned}
&\int_\Omega \hat{w}_{i,j}\sigma_{ij}\,\mathrm{d}\Omega + \sum_m \int_{\Omega^{(m)}} H^{(m)}\tilde{w}_{i,j}^{(m)}\sigma_{ij}^{(m)}\,\mathrm{d}\Omega + \alpha\int_{\Gamma_*} [\![w_i]\!] n_i n_j [\![u_j]\!]\,\mathrm{d}\Gamma \\
&- \int_{\Gamma_*} [\![w_i]\!] n_i n_j \langle\sigma(\boldsymbol{u})_{jk}\rangle n_k\,\mathrm{d}\Gamma - \int_{\Gamma_*} [\![u_i]\!] n_i n_j \langle\sigma(\boldsymbol{w})_{jk}\rangle n_k\,\mathrm{d}\Gamma \\
&- \int_{\Gamma_*} [\![w_i]\!] h_{t,i}^*\,\mathrm{d}\Gamma \\
&= \int_\Omega \hat{w}_i b_i\,\mathrm{d}\Omega + \sum_m \int_{\Omega^{(m)}} H^{(m)}\tilde{w}_i^{(m)} b_i^{(m)}\,\mathrm{d}\Omega \\
&+ \int_{\Gamma_\sigma} \hat{w}_i h_i\,\mathrm{d}\Gamma + \sum_m \int_{\Gamma_\sigma^{(m)}} H^{(m)}\tilde{w}_i^{(m)} h_i^{(m)}\,\mathrm{d}\Gamma
\end{aligned} \tag{6.38}$$

where the tangential traction, $h_{t,i}^*$, is subjected to the set of constraints in (6.3). When comparing the weak form to the variational problem (4.33), one can see, that the term responsible for the symmetry in the tangential contributions is absent. Hence, the formulation is not symmetric anymore.

6.4 Discretization

As indicated above, the equations for the bulk field and the normal constraints do not change. The residual, $\boldsymbol{R}^u$, and its linearization can be adopted from the untied problem in section 3. As also mentioned above, the normal behavior at the interface is the same as in the frictionless sliding problem. The contributions to the residual and its linearization due to normal constraints are adopted from the frictionless sliding problem in section 5. They are not derived again. Nevertheless, the contributions to the global residual and its linearization due to the tangential constraints at the interface have to be derived again by discretizing the additional contributions to the weak forms presented in sections 6.3.1 and 6.3.2 for the penalty method and the stabilized method. The discretization of the test function takes the same form as the one of the variation of the displacement field (3.8):

$$\underline{\boldsymbol{w}} \approx \boldsymbol{w}^h = \hat{\boldsymbol{N}}\hat{\boldsymbol{c}} + \sum_m \left(H^{(m)} \tilde{\boldsymbol{N}}^{(m)} \right) \tilde{\boldsymbol{c}} \in \mathcal{W}^h \subset \mathcal{W} \tag{6.39}$$

with $\hat{\boldsymbol{c}}$ and $\tilde{\boldsymbol{c}}$ denoting the nodal values of the test function.

6.4.1 Penalty method

Inserting the discretization of the test function and of the displacement field and using the arbitrariness of the test function leads to an expression for the elementary contribution to the residual for the constraints in tangential direction:

$$\boldsymbol{r}_t^{pen,(e)} = \begin{bmatrix} \boldsymbol{0}_{6\times 1} \\ -\int_{\Gamma_*^{(e)}} [\![\tilde{\boldsymbol{N}}]\!]^T \boldsymbol{h}_t^* \, \mathrm{d}\Gamma \end{bmatrix} \tag{6.40}$$

where the tangential traction $\boldsymbol{h}_t^*$ has to be determined at every Gauß point using the return-mapping framework presented in section 6.2.1. These elementary contributions can be assembled to a global contribution such that the global residual is computed as the sum of the residual contributions of the bulk field, the normal and the tangential constraints.
The global linearization of the residual can be assembled from element contributions, since the assembly operator is linear. The residual given in (6.40) has to be linearized:

$$\Delta \boldsymbol{r}_t^{pen,(e)} = \boldsymbol{k}_t^{pen,(e)} \Delta \boldsymbol{d} = \begin{bmatrix} \boldsymbol{0}_{6\times 6} & \boldsymbol{0}_{6\times 6} \\ \boldsymbol{0}_{6\times 6} & \boldsymbol{\kappa}_{22}^{pen,(e)} \end{bmatrix} \tag{6.41}$$

with

$$\begin{aligned}\boldsymbol{\kappa}_{22}^{pen,(e)} &= \int_{\Gamma_*^{(e)}} [\![\tilde{\boldsymbol{N}}]\!]^T \frac{\partial \boldsymbol{h}_t^*}{\partial \tilde{\boldsymbol{d}}} \, \mathrm{d}\Gamma \\ &= \begin{cases} -\alpha_T \int_{\Gamma_*^{(e)}} [\![\tilde{\boldsymbol{N}}]\!]^T \left(\boldsymbol{I}_{2\times 2} - \boldsymbol{n}\boldsymbol{n}^T \right) [\![\tilde{\boldsymbol{N}}]\!] \, \mathrm{d}\Gamma & \text{if } \Phi^{trial} \leq 0 \\ \boldsymbol{0}_{6\times 6} & \text{if } \Phi^{trial} > 0 \end{cases} \end{aligned} \tag{6.42}$$

Here, the results from (6.24) in conjunction with (6.8) are used. The integration along the interface is done by Gauß quadrature. As for the integration process for the residual, the distinction bewteen stick and slip has to be made at every Gauß point. Before looking at the stabilized method, it should be noted that the stiffness matrix for the penalty method with perfect plasticity is symmetric.

6.4.2 Stabilized method inspired by Nitsche's method

Inserting the discretization of the test function and of the displacement field and using the arbitrariness of the test function leads to an expression for the elementary contribution to the residual for the constraints in tangential direction:

$$\boldsymbol{r}_t^{stab,(e)} = \begin{bmatrix} \boldsymbol{0}_{6\times 1} \\ -\int_{\Gamma_*^{(e)}} [\![\tilde{\boldsymbol{N}}]\!]^T \boldsymbol{h}_t^* \, \mathrm{d}\Gamma \end{bmatrix} \tag{6.43}$$

where the tangential traction $\boldsymbol{h}_t^*$ has to be determined using the return-mapping framework presented in section 6.2.2. These elementary contributions can be assembled to a global contribution such that the global residual is computed as the sum of the residual contributions of the bulk field, the normal and the tangential constraints.
The global linearization of the residual can be assembled from element contributions, since the assembly operator is linear. The residual given in (6.43) has to be linearized:

$$\Delta \boldsymbol{r}_t^{pen,(e)} = \boldsymbol{k}_t^{pen,(e)} \Delta \boldsymbol{d} = \begin{bmatrix} \boldsymbol{0}_{6\times 6} & \boldsymbol{0}_{6\times 6} \\ \boldsymbol{\kappa}_{21}^{stab,(e)} & \boldsymbol{\kappa}_{22}^{stab,(e)} \end{bmatrix} \tag{6.44}$$

with the submatrices

$$\begin{aligned}
\boldsymbol{\kappa}_{21}^{stab,(e)} &= \begin{cases} \int_{\Gamma_*^{(e)}} [\![\tilde{\boldsymbol{N}}]\!]^T \left(\boldsymbol{I}_{2\times 2} - \boldsymbol{n}\boldsymbol{n}^T\right) \check{\boldsymbol{n}} \langle \boldsymbol{C}\hat{\boldsymbol{B}} \rangle \, \mathrm{d}\Gamma & \text{if } \Phi^{trial} \leq 0 \\ \boldsymbol{0}_{6\times 6} & \text{if } \Phi^{trial} > 0 \end{cases} \\
\boldsymbol{\kappa}_{22}^{stab,(e)} &= \begin{cases} -\int_{\Gamma_*^{(e)}} [\![\tilde{\boldsymbol{N}}]\!]^T \left(\boldsymbol{I}_{2\times 2} - \boldsymbol{n}\boldsymbol{n}^T\right) \left(\alpha_t [\![\tilde{\boldsymbol{N}}]\!] - \check{\boldsymbol{n}} \langle \boldsymbol{C}\tilde{\boldsymbol{B}} \rangle\right) \mathrm{d}\Gamma & \text{if } \Phi^{trial} \leq 0 \\ \boldsymbol{0}_{6\times 6} & \text{if } \Phi^{trial} > 0 \end{cases}
\end{aligned} \tag{6.45}$$

As seen in the weak form (6.38), the element stiffness matrix for the tangential constraints is not symmetric anymore.

7 Domains with more than one interface

Since the presented formulations are not restricted to a domain comprising only two grains with one interface, some remarks on the handling of more grains and interfaces have to be given. Basically, only the notation is a bit more complicated because some additional indices are necessary. The basic equations presented so far are still valid and can easily be extended to an arbitrary number of interfaces. This results only in a more complicated implementation and additional effort on "bookkeeping" but not in conceptual difficulties. First of all, some general remarks are made. Afterwards, special properties of two types of interface topologies are shown. A possibility for an algorithmic treatment is given in section 8.5.

7.1 General remarks

Basically, two cases can be considered when more than one interface is located in the domain: These interfaces intersect each other (see figure 7.1b), or not (see figure 7.1a). To be

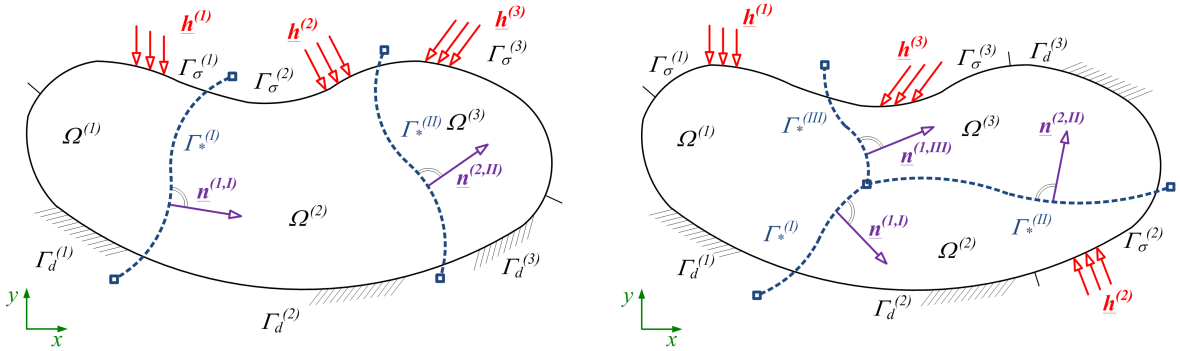

(a) Non intersecting interfaces

(b) Intersecting interfaces

FIGURE 7.1: More grains and interfaces in a domain

clear, each normal vector needs a further index, since there might be more than one normal belonging to a grain. Also, the interfaces get indices. With more than one interface, the variational forms, given in sections 4.2, 5.2 and 6.3 have to be generalized by replacing the integrals over the interface Γ_* with a sum over all interfacial integrals:

$$\int_{\Gamma_*} \bullet \, \mathrm{d}\Gamma \rightarrow \sum_{M=1}^{numint} \int_{\Gamma_*^{(M)}} \bullet \, \mathrm{d}\Gamma \tag{7.1}$$

where M is the index for the *numint* interfaces in the domain. The basic idea to handle more than one interface from an implementational point of view is to loop over all interfaces. The equations and methods of the problem with two grains and one interface can be used, where only the grain indices have to be adapted. The idea to treat each interface independently from the other interfaces results not only in the variational and implementational treatment. It also provides additional freedom to design a problem. The constraints of each interface can be chosen individually and do not have to be the same for all interfaces. Of course, all grains can have different material properties.

Numerical examples with more than one interface for the fully tied problem can be found in [33]. Section 9.2.3 provides an example with two triple junctions and five interfaces with frictionless sliding. The same example is solved with plasticity in section 9.3.3. An example containing several grains with plasticity at the interfaces is presented in section 9.3.4. For more algorithmic and implementational details, see section 8.5.

Following [38], additional sets of enriched degrees of freedoms are introduced. The new numbering scheme is depicted in figure 7.2. The only difference to the simple case with only

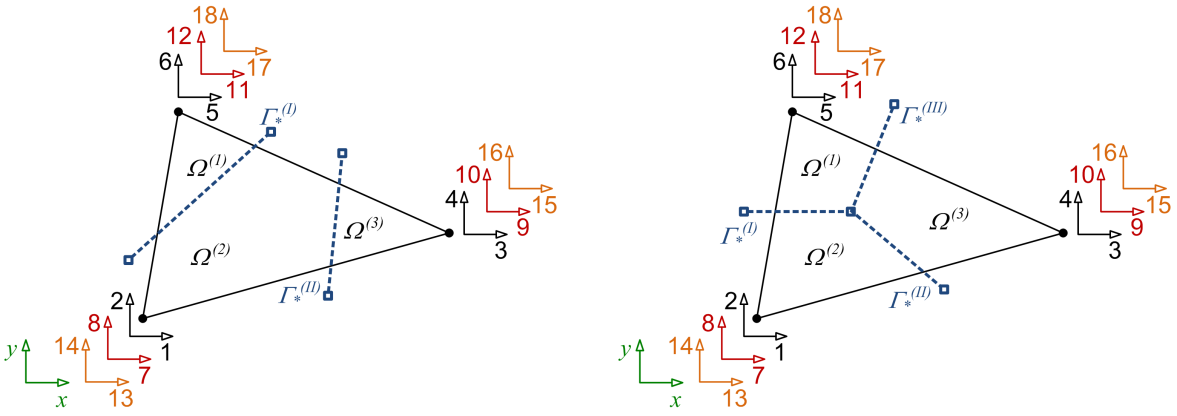

(a) Two non intersecting interfaces in an element (b) Three intersecting interfaces in an element

FIGURE 7.2: Two admissible cases for more grains and interfaces in a single element. The base degrees of freedom comprise numbers 1 to 6, while the first set of enriched degrees of freedom comprise numbers 7 to 12 and the second set the numbers 13 to 18.

two grains and one interface is, that one has to pick the right enriched degree of freedom, if a node is enriched twice. Hence, the bookkeeping of the degrees of freedom is a bit more complicated, but the principles remain the same. Using a second set of enriched degrees of

freedom, the discretization of the displacement field (3.7) has to be extended, too:

$$\underline{\boldsymbol{u}} \approx \boldsymbol{u}^h = \hat{\boldsymbol{N}}\ \hat{\boldsymbol{d}} + \sum_m \left(H^{(m)} \tilde{\boldsymbol{N}}^{(m)} \right) \tilde{\boldsymbol{d}} + \sum_m \left(H^{(m)} \tilde{\tilde{\boldsymbol{N}}}^{(m)} \right) \tilde{\tilde{\boldsymbol{d}}} \in \mathcal{U}^h \subset \mathcal{U} \tag{7.2}$$

where $\tilde{\tilde{\boldsymbol{N}}}$ represents the shape function matrix for the second enrichment. It takes the same structure as $\tilde{\boldsymbol{N}}$. The displacements in the second enriched degrees of freedom are denoted as $\tilde{\tilde{\boldsymbol{d}}}$. Using this discretization, the residual and its linearization can be derived again. This is not done here explicitely, since it follows the same procedures as in the previous sections. However, the size of the elementary quantities changes. For example, the element stiffness matrix for a linear triangular element, which is intersected by one interface, is 12×12, whereas the element stiffness matrix for a linear triangular element, which is intersected by two interfaces, is 18×18, since there are 6 more enriched degrees of freedom. After these general remarks, the two cases depicted in figure 7.1 will be discussed in detail. In order to reduce the implementational effort, some assumptions are made in this work:

- The maximum number of non intersecting interfaces, that cut one element, is two, whereby each grain has to contain one node.
- The maximum number of interfaces, that intersect in one point, is three, whereby each grain has to contain one node.
- The number of *triple junctions* in one element is limited to one.
- The number of triple junctions in the entire domain is not restricted, unless the previous assumption is violated.

These assumptions make sure, that a node has either no, one or two enrichments.

Remark 7.1. *The methods presented here are general enough to be applied to any kind of elements. Though, since the code, developed for this work, uses linear triangular elements, all graphics are shown for this type of elements. The size of elementary quantities is computed based on this element type, too.*

7.2 Non intersecting interfaces

The case of non intersecting interfaces can be divided into two subcases, where the mesh size h plays an important role. If the minimal distance between the interfaces is greater than

the mesh size h, which means, that all nodes in the domain are either not enriched or only once. This case is very similar to the problem with only two grains and one interface. Due to the large distance between the two interfaces, grain $\Omega^{(1)}$ does not interact with grain $\Omega^{(3)}$, where notations from figure 7.1 are used. Since there is no element, which is enriched by two grains, the modification from (7.1) is the only one, that has to be considered. The reason for this is, that the enrichment influences only the elements near the interface. Referring to the example given above, this case results in 12×12 element stiffness matrices for cut elements. But if the minimal distance between the interfaces is so small, that two interfaces will cut the same element (see figure 7.2a), some additional issues have to be considered. The total number of degrees of freedom of the element is now $2 \times \mathit{nodes} \times 3$, where 2 is the number of degrees of freedom per node, *nodes* the number of nodes per element and 3 refers to the number of sets of degrees of freedom. This number is based on the base degrees of freedom and the two enrichments. For a linear triangular element, then the element stiffness matrix has the dimensions 18×18 for example.

7.3 Intersecting interfaces

When there are intersecting interfaces, at least one element is cut by three interfaces (see figure 7.2b). In this case, each node is enriched twice. The element stiffness matrix has contributions based on all three grains. The determination of its size is similar to the case with non intersecting interfaces in an element and results also in a 18×18 matrix. In this case, the integration along the interfaces might be interesting. Using the looping-scheme from algorithm 8.3, even this case can be handled very easily.

8 Implementational details

The implementation that was done parallel to this work is presented briefly in this section. The code is written in MATLAB *R2010a - Student*. First of all, the current status of the code is compared to the one at the beginning of the work, followed by some remarks on the ordering scheme of the degrees of freedom in the global system of equations. Then, the load stepping scheme and the nested Newton-Raphson-scheme that are used to solve the nonlinear equations are presented in detailed algorithmic notation. Afterwards, the algorithmic framework for the return-mapping algorithm is presented, which uses the equations provided in section 6.2. Finally, an implementational framework to handle more than one interface is discussed.

8.1 Comparison between original and current implementation

The routines for computational geometry and structured meshing were written by John E. Dolbow, Duke University. The preprocessing routines to create the mesh and interfaces were restricted such that it is not possible, that an interface intersects a node. The reason lies only in the implementation, whereas the method itself is capable of that [38]. An implementation of the equations presented in [33] was done by Jessica D. Sanders, Duke University. This code could solve three pure elastic problems with stabilized interfacial constraints for the fully tied problem. It had some trouble to handle triple junctions like the ones described in section 7.3 correctly. For postprocessing, some routines to plot the deformed mesh without considering the displacement jump at the interface were available. The stress computation had trouble with triple junctions, too. All these parts of solving a problem had to be executed by hand whereby the user had to take care of copying data from one directory to another.
First steps were to modify the code such that examples are not part of the code itself but are given in separate input files. Dirichlet and Neumann boundary conditions are defined in separate files now, which are included during the preprocessing. A control routine manages the geometry configuration, preprocessing, solving and postprocessing and handles the data exchange between these steps. The routines to create the geometry were modified since some of the geometric data is needed to describe the interface properly. Unfortunately, the restriction of interfaces, that are not allowed to lie on nodes, could not be removed. The use of unstructured meshes which are created with GMSH [15] is possible. The purely linear computation was dropped and a load stepping scheme with a nested Newton-Raphson-

scheme is implemented. It is possible to use different load curves. The types of interfacial constraints were extended to the ones described in this work. Postprocessing routines to evaluate stresses in the bulk field and tractions at the interface are available. Visualization of the enriched displacement field, stresses and tractions as well as the stick-slip-zones is possible with MATLAB figures or with PARAVIEW *3.8.0* using the VTK *Version 4.2* file format. Movies can be generated.

8.2 Ordering of degrees of freedom

The ordering of the degrees of freedom in the global displacement vector, $\boldsymbol{D}$, influences the bandwidth of the tangent stiffness matrix. Often, a small bandwith is desired. The displacement vector, used to derive the expressions for the residuals and the stiffness matrices, is not the best choice regarding the bandwidth of the stiffness matrix. Instead of appending the enriched degrees of freedom at the end of the base degrees of freedom, they should be inserted in between. An example can be given as:

$$\boldsymbol{d} = \left[\hat{d}_{1x}\ \hat{d}_{1y}\ \tilde{d}_{1x}\ \tilde{d}_{1y}\ \hat{d}_{2x}\ \hat{d}_{2y}\ \tilde{d}_{2x}\ \tilde{d}_{2y}\ \hat{d}_{3x}\ \hat{d}_{3y}\ \tilde{d}_{3x}\ \tilde{d}_{3y}\right]^T \tag{8.1}$$

where the number denotes a node in a triangular element and the letters x and y correspond to the x- and y-direction of the reference frame. Hence, the bandwith of the resulting stiffness matrix can be reduced for structured meshes.

8.3 Load stepping scheme and nested Newton-Raphson-scheme

Since problems with plasticity at the interface give rise to a nonlinear system, a proper solution technique has to be applied. Here, the external load, either tractions or prescribed displacements, is increased stepwise using a *load stepping scheme* with the load step indes k. For each load step, the system of equations that has to be solved can be written as a residual:

$$\boldsymbol{R}(\boldsymbol{D}_{k+1}) = 0 \tag{8.2}$$

This system of equations is solved using a Newton-Raphson-technique which is a standard iterative method to solve systems of nonlinear equations. Thus, (8.2) is solved iteratively such that the unknown solution at iteration $j+1$ can be computed based on the known

solution at iteration j. It can be derived by introducing a Taylor expansion of (8.2):

$$\boldsymbol{R}(\boldsymbol{D}_{k+1}^{j+1}) = \boldsymbol{R}(\boldsymbol{D}_{k+1}^{j}) + \frac{\partial \boldsymbol{R}(\boldsymbol{D}_{k+1}^{j})}{\partial \boldsymbol{D}} \Delta \boldsymbol{D}_{k+1}^{j+1} + \mathcal{O}(\Delta \boldsymbol{D}^2) \doteq 0 \tag{8.3}$$

In order to compute the displacement increment, $\Delta \boldsymbol{D}_{k+1}^{j+1}$, the following linear system has to be solved:

$$\frac{\partial \boldsymbol{R}(\boldsymbol{D}_{k+1}^{j})}{\partial \boldsymbol{D}} \Delta \boldsymbol{D}_{k+1}^{j+1} = -\boldsymbol{R}(\boldsymbol{D}_{k+1}^{j}) \tag{8.4}$$

This can be done using several types of solvers. A detailed description is omitted here. The global displacement vector, $\boldsymbol{D}_{k+1}^{j}$, as well as the global displacement increment for the current load step, $\delta \boldsymbol{D}_{k+1}^{j}$, can be updated:

$$\begin{aligned} \boldsymbol{D}_{k+1}^{j+1} &= \boldsymbol{D}_{k+1}^{j} + \Delta \boldsymbol{D}_{k+1}^{j+1} \\ \delta \boldsymbol{D}_{k+1}^{j+1} &= \delta \boldsymbol{D}_{k+1}^{j} + \Delta \boldsymbol{D}_{k+1}^{j+1} \end{aligned} \tag{8.5}$$

Since it is an iterative procedure, some criteria help to decide, when the approximation of the solution is sufficiently accurate. One of them is the Euclidian norm of the residual, $\|\boldsymbol{R}_{k+1}^{j}\|$. Also, the Euclidian norm of the displacement increment, $\|\Delta \boldsymbol{D}_{k+1}^{j+1}\|$, might be of interest. A third often used criterion is the energy norm, $|\boldsymbol{R}_{k+1}^{j^T} \Delta \boldsymbol{D}_{k+1}^{j+1}|$. For a practical computation, it makes sense to limit the number of Newton-Raphson-iterations to a maximum number, j_{max}. For further remarks on these norms, see [6]. The norms and the number of iterations have to be checked in each iteration step. If the norms are smaller than given tolerances, $tol_{(\bullet)}$, the solution is assumed to be converged. In order to make the tolerances independent of the physical problem, they are normalized with the norms of the first iteration. The load stepping scheme with nested Newton-Raphson-scheme used in the code for this work is given in algorithm 8.1.

Algorithm 8.1 Load stepping scheme with nested Newton-Raphson-scheme

for $k = 0$ **to** $k = K$ **do**
  compute: $\boldsymbol{F}_{k+1}^{ext} = \frac{k+1}{K+1}\boldsymbol{F}_{total}^{ext}$
  set: $\boldsymbol{D}_{k+1}^{0} = \boldsymbol{D}_{k}^{converged}$
  set: $\delta\boldsymbol{D}_{k+1}^{0} = \boldsymbol{0}$
  repeat
    assemble residual: $\boldsymbol{R}_{k+1}^{j}$
    assemble tangent matrix: $\boldsymbol{K}_{k+1}^{j}$
    solve: $\boldsymbol{K}_{k+1}^{j}\Delta\boldsymbol{D}_{k+1}^{j+1} = -\boldsymbol{R}_{k+1}^{j}$
    update: $\delta\boldsymbol{D}_{k+1}^{j+1} = \delta\boldsymbol{D}_{k+1}^{j} + \Delta\boldsymbol{D}_{k+1}^{j+1}$
    update: $\boldsymbol{D}_{k+1}^{j+1} = \boldsymbol{D}_{k+1}^{j} + \Delta\boldsymbol{D}_{k+1}^{j+1}$
    update iterator: $j = j + 1$
    if $j > j_{max}$ **then**
      error: Newton did not converge in j_{max} iterations.
    end if
  until $\frac{\|\boldsymbol{R}_{k+1}^{j}\|}{\|\boldsymbol{R}_{k+1}^{0}\|} < tol_{res}$ **and** $\frac{\|\Delta\boldsymbol{D}_{k+1}^{j}\|}{\|\Delta\boldsymbol{D}_{k+1}^{0}\|} < tol_{dis}$ **and** $\frac{|\boldsymbol{R}_{k+1}^{j^T}\Delta\boldsymbol{D}_{k+1}^{j+1}|}{|\boldsymbol{R}_{k+1}^{0^T}\Delta\boldsymbol{D}_{k+1}^{0}|} < tol_{en}$
end for

8.4 Return-mapping algorithm

In order to compute the residual, the integrations, that have to be carried out, are done by Gauß quadrature. The return-mapping algorithm has to be applied at every Gauß point. Since the return-mapping algorithm is displacement driven [36], a *given* displacement increment is needed to compute the trial state. This displacement increment is the difference between the current displacement vector and the displacement vector at the end of the previous converged load step. Since a Newton-Raphson-technique is used to solve the nonlinear system of equations, the current displacement vector changes in every Newton step. The displacement increment which has to be considered for the return-mapping algorithm can be identified as the current displacement increment for the current load step, $\delta\boldsymbol{D}_{k+1}^{j+1}$, where k refers to the load steps and j to the Newton iterations. The increment is zero in the first Newton step of each load step and is unequal to zero in all other iterations. During the Gauß quadrature, the following *return-mapping algorithm* is applied at every Gauß point:

Algorithm 8.2 Return-mapping algorithm

Compute elastic trial state: $\underline{\boldsymbol{h}}^{*,trial}_{t,k+1}$, $[\![\underline{\boldsymbol{u}}]\!]^{pl,trial}_{t,k+1}$
Evaluate yield condition for trial state: Φ^{trial}_{k+1}
if $\Phi^{trial}_{k+1} \leq 0$ **then**
  Elastic step:
    $\underline{\boldsymbol{h}}^{*}_{t,k+1} = \underline{\boldsymbol{h}}^{*,trial}_{t,k+1}$
    $[\![\underline{\boldsymbol{u}}]\!]^{pl}_{t,k+1} = [\![\underline{\boldsymbol{u}}]\!]^{pl,trial}_{t,k+1}$
else
  Plastic step:
    $\xi = \frac{\Phi^{trial}_{k+1}}{\alpha_t}$
    $\underline{\boldsymbol{h}}^{*}_{t,k+1} = \left(1 - \frac{\alpha_t \, \xi}{\|\underline{\boldsymbol{h}}^{*,trial}_{t,k+1}\|}\right) \underline{\boldsymbol{h}}^{*,trial}_{t,k+1}$
    $[\![\underline{\boldsymbol{u}}]\!]^{pl}_{t,k+1} = [\![\underline{\boldsymbol{u}}]\!]^{pl}_{t,k} - \xi \frac{\underline{\boldsymbol{h}}^{*,trial}_{t,k+1}}{\|\underline{\boldsymbol{h}}^{*,trial}_{t,k+1}\|}$
end if

Using this algorithm guarantees, that the tangential traction always satisfies the yield condition $\Phi \leq 0$. In order to prepare the assembly of the stiffness matrix, one should store, whether the trial state at a Gauß point is admissible or not since this information is needed to decide which stiffness contribution has to be assembled.

8.5 Handling of more than one interface

In order to handle more than one interface in the domain, the following method is used: A data structure stores some information about each cut element like the connectivity between all cut elements and all interfaces, coordinates of intersection points or the inner state variables used for plasticity. The following looping scheme is applied to assemble contributions to the residual or the tangent matrix due to constraints or to evaluate tractions at the interface:

Algorithm 8.3 Looping-scheme for more interfaces

for all interfaces i **do**
  for all elements e that are cut by interface i **do**
    ...
  end for
end for

The interfaces are treated independently. The only problem to take care of is to pick the

right enriched degrees of freedom, when an element is intersected by more than one interface. This framework can be applied for an arbitrary number of interfaces in the domain.

9 Numerical examples

Some numerical examples are provided to show features of the presented methods. First, some general remarks are given, that are common for all examples. Afterwards, examples with frictionless sliding at the interface are given in section 9.2, followed by examples with perfect plasticity at the interface in section 9.3.

9.1 General remarks

Here, some general remarks, which are valid for all numerical examples in this work, are presented. All examples are modelled with linear triangular elements [19]. Structured and unstructured meshes are used. The unstructured meshes are generated via GMSH [15]. The properties of meshes are often summarized in a table, where the following notations are used: *Mesh ID* is an ID to refer to the mesh later. The characteristic mesh size h is given by *Mesh size h*, which is computed as the circumradius of the greatest element in the entire mesh. *Elements* gives the number of elements in the entire discretization. The number of base degrees of freedom is given by *Base DOFs*, the number of all degrees of freedom, including base and enriched degrees of freedom, is given by *All DOFs*. *Cut elements* indicates, how many elements are intersected by interfaces. The material in each grain is assumed to be linear elastic, but may have different properties in different grains. A plane stress state is assumed. No example contains any body forces. Dirichlet boundary conditions along the embedded interface are imposed using the methods which are described in this thesis. Dirichlet boundary conditions to support the domain along the Dirichlet boundary, Γ_d, are imposed using a collocation method. The convergence of the Newton-Raphson-scheme is controlled by a relative tolerance, which is generally chosen as 10^{-10} for all types of convergence criteria. Different choices are mentioned explicitely.
To show the accuracy of the presented methods, some examples compare simulation results to analytical solutions or results which are obtained with very fine meshes when no analytical solution could be found. Therefor, errors are computed as a norm of the difference between the simulation result and the "reference" solution and are normalized with the norm of the reference solution:

$$error_{(\bullet)} = \frac{\|(\bullet)^h - (\bullet)^{ref}\|}{\|(\bullet)^{ref}\|} \tag{9.1}$$

where $(\bullet)^h$ denotes a discretized quantitiy and $(\bullet)^{ref}$ the reference solution. The error in the displacement field and in the traction field is measured in the $\mathbb{L}_2$-norm which is defined as [6]:

$$\|(\bullet)\|_{\mathbb{L}_2} = \sqrt{\int_\Omega (\bullet)^2 \, d\Omega}, \tag{9.2}$$

If $(\bullet)$ is defined only on a boundary Γ, the domain of integration in (9.2) has to be adapted properly. Also, the energy norm is computed which is defined as [6]:

$$energy\ norm: \sqrt{\int_\Omega \varepsilon_{ij} C_{ijkl} \varepsilon_{kl} \, d\Omega} \tag{9.3}$$

Here, the error in the energy norm is also normalized with the energy norm of the reference solution.

9.2 Numerical examples for frictionless sliding

First, it will be shown, that all three methods, presented in section 5, pass the patch test. Then, some convergence and stability properties will be shown for all three methods. Finally, a free grain boundary sliding example adopted from [38] is presented. All loads are imposed in a single step.

9.2.1 Modified Patch test

An adaptation of the well-known patch test adopted from [7] is used here to show frictionless sliding at the interface. The numerical results are compared to an analytical solution.
The considered domain is a rectangle with length $l = 16$ and height $h = 4$. The right boundary is loaded with a constant traction $p = -0.25$, such that a constant stress field is expected. A vertical interface with frictionless sliding is introduced at position $x = 5.5$, which divides the domain into two grains $\Omega^{(1)}$ and $\Omega^{(2)}$ such that the length of interfacial subsegments is not the same in every cut element. A schematic is given in figure 9.1. $\Omega^{(1)}$ is fixed at its left boundary. Therefore, the x-displacement is constrained over the entire left boundary. The y-displacement is only constrained at the center node at $y = 0$. Lateral contraction is enabled. To constrain the rigid body mode of $\Omega^{(2)}$ in y-direction, the y-

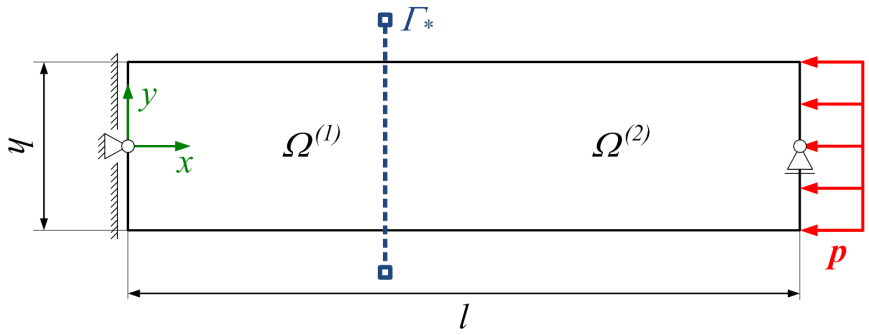

FIGURE 9.1: Schematic of domain for modified patch test: Two grains divided by an embedded interface with a constant line load.

Name	Notation	value
Young's modulus in $\Omega^{(1)}$	$E^{(1)}$	1000.0
Young's modulus in $\Omega^{(2)}$	$E^{(2)}$	1000.0
Poisson's ratio in $\Omega^{(1)}$	$\nu^{(1)}$	0.3
Poisson's ratio in $\Omega^{(2)}$	$\nu^{(2)}$	0.0

TABLE 1: Material properties for modified patch test: Different Poisson's ratios lead to a discontinuous displacement field at the interface as a result of lateral expansion.

displacement of the center node of the right boundary is imposed to be equal to zero, since no displacement in y-direction is expected. In order to demonstrate frictionless sliding, different material properties are assigned to the two grains. They are listed in table 1. Due to a non-zero Poisson's ratio, $\Omega^{(1)}$ is expected to expand in y-direction under compression. $\Omega^{(2)}$ will not have any lateral contraction, so there has to be a jump in the y-displacement at the interface. This jump will be enabled by the frictionless sliding.
First, an analytical solution is presented. Due to the boundary conditions and using Cauchy's theorem $\sigma_{ij} n_j = h_i$ with n_j denoting the normal vector pointing outward of the domain and the external traction vector h_i, the stresses in both grains take the following values:

$$\begin{aligned} \sigma_{xx}^{(1)} &= -0.25,\ \sigma_{yy}^{(1)} = 0,\ \sigma_{xy}^{(1)} = 0 \\ \sigma_{xx}^{(2)} &= -0.25,\ \sigma_{yy}^{(2)} = 0,\ \sigma_{xy}^{(2)} = 0 \end{aligned} \tag{9.4}$$

Due to $\sigma_{xy}^{(1)} = \sigma_{xy}^{(2)} = 0$, the shear strains $\varepsilon_{xy}^{(1)}$ and $\varepsilon_{xy}^{(2)}$ will be zero, too. According to [40], the strains $\varepsilon_{xx}^{(1)}$, $\varepsilon_{yy}^{(1)}$, $\varepsilon_{xx}^{(2)}$ and $\varepsilon_{yy}^{(2)}$ in a two dimensional setting for a plane stress state are given

by:

$$\begin{aligned}
\varepsilon_{xx}^{(1)} &= \frac{1}{E^{(1)}}\left(\sigma_{xx}^{(1)} - \nu^{(1)}\sigma_{yy}^{(1)}\right) = -2{,}5 \cdot 10^{-4} \\
\varepsilon_{yy}^{(1)} &= \frac{1}{E^{(1)}}\left(\sigma_{yy}^{(1)} - \nu^{(1)}\sigma_{xx}^{(1)}\right) = \quad 7{,}5 \cdot 10^{-5} \\
\varepsilon_{xx}^{(2)} &= \frac{1}{E^{(2)}}\left(\sigma_{xx}^{(2)} - \nu^{(2)}\sigma_{yy}^{(2)}\right) = -2{,}5 \cdot 10^{-4} \\
\varepsilon_{yy}^{(2)} &= \frac{1}{E^{(2)}}\left(\sigma_{yy}^{(2)} - \nu^{(2)}\sigma_{xx}^{(2)}\right) = \quad 0
\end{aligned} \tag{9.5}$$

Using the strain values and the geometric quantities, the elongations $\triangle\, l^{(m)}$ in x-direction and $\triangle\, h^{(m)}$ in y-direction compute as:

$$\begin{aligned}
\triangle\, h^{(1)} &= \quad 3 \cdot 10^{-4} \\
\triangle\, h^{(2)} &= \quad 0 \\
\triangle\, l^{(1)} &= -1.375 \cdot 10^{-3} \\
\triangle\, l^{(2)} &= -2.625 \cdot 10^{-3} \\
\Longrightarrow \triangle\, l &= \triangle\, l^{(1)} + \triangle\, l^{(2)} = -4 \cdot 10^{-3}
\end{aligned} \tag{9.6}$$

Using (9.6), the displacement field is given as function of the coordinates x and y:

$$\begin{aligned}
u_x &= \frac{\triangle\, l}{l} x \\
u_y &= \begin{cases} \frac{\triangle h^{(1)}}{h} y & \text{if } x < 5.5 \\ 0 & \text{otherwise.} \end{cases}
\end{aligned} \tag{9.7}$$

The patch test can be passed independently of the mesh density. Here, examples for a coarse structured and a finer unstructured mesh are presented (see figure 9.2 for mesh and interface). An overview over the number of elements and degrees of freedom for both meshes is provided in table 2. For the penalty method, the penalty parameter is chosen as $\alpha = 1.0 \cdot 10^7$ for the coarse structured mesh and as $\alpha = 3.0 \cdot 10^8$ for the finer unstructured mesh. Using Nitsche's method, the patch test can be passed regardless of the choice of the stability parameter α [33], if $\alpha \geq 0$. So, here $\alpha = 0$ is chosen for Nitsche's method. The deformed state for the coarse mesh is shown in figure 9.3, where the deformation is scaled by factor 1000 and the displacement field is shown as a contour plot. The continuity of the x-component as well as the discontinuity of the y-component at the interface is very obvious. For all three methods,

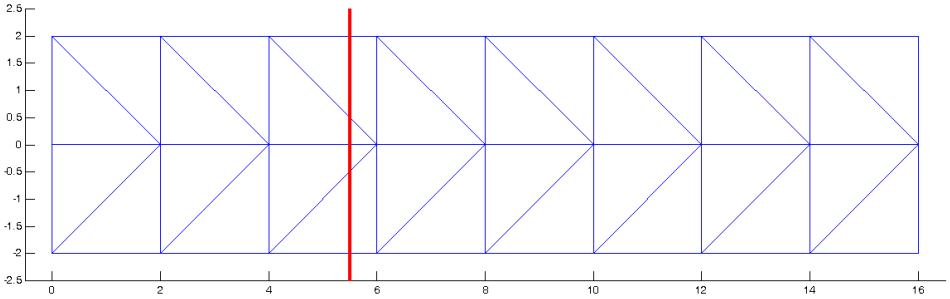

(a) Structured mesh with 32 elements

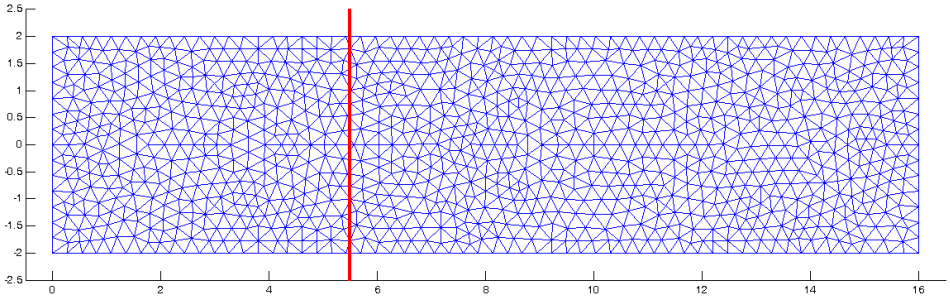

(b) Unstructured mesh with 2020 elements

FIGURE 9.2: Structured and unstructured mesh with embedded interface with frictionless sliding at $x = 5.5$ for modified patch test

the stresses are computed correctly. The stress in x-direction, σ_{xx}, is constant in the entire domain and takes the value $\sigma_{xx} = -0.25$. The stresses σ_{yy} and σ_{xy} are zero to machine precision, as it is expected. The stress field and the displacement field match the analytical solution, provided in (9.4) and (9.6) for both meshes. Since the interface is in an area with a constant stress field, the tractions at the interface show no oscillations for all methods. So, the patch test is passed for all three methods.

	structured mesh	unstructured mesh
Mesh size h	1.414	0.208
Number of elements	32	2020
Number of base DOFs	54	2168
Number of all DOFs	66	2236
Number of cut elements	4	32

TABLE 2: Summarized data for structured and unstructured mesh for the modified patch test

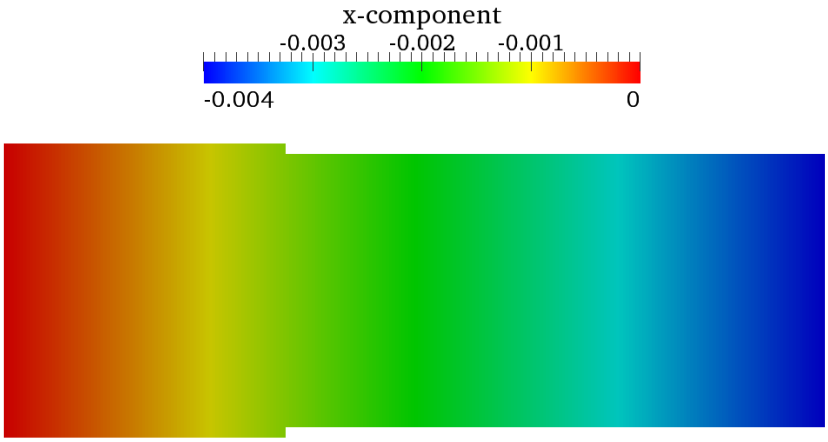

(a) x-component

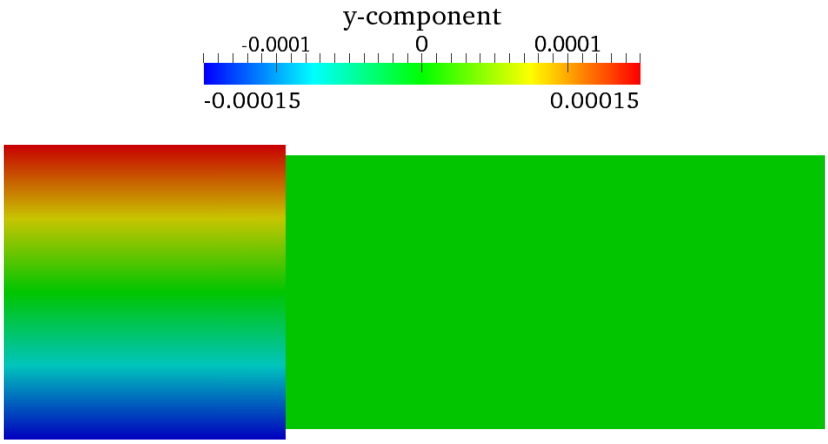

(b) y-component

FIGURE 9.3: Contour plot of the displacement field in deformed state for modified patch test with frictionless sliding. Deformation is scaled by factor 1000. The x-component is continuous, the y-component is discontinuous at the interface.

9.2.2 Stability and convergence analysis using an analytical solution

In order to show some properties of convergence and convergence rates of the presented methods for frictionless sliding, simulation results are compared to an analytical solution. A special focus is drawn on the stability of the methods. If the interface with frictionless sliding resides in a part of the domain, where the stress field is not constant, oscillations will occur, when Lagrange multipliers are used to enforce the constraints at the interface. This does not happen for interfaces in constant stress fields like a patch test as it can be seen in the previous example or in [33]. In order to trigger stability problems, the interface has to be located in an area with a stress field that is at least linear. Due to the frictionless sliding, there are no shear stresses allowed in the part of the domain which is intersected by the interface. The problem considered here is set up as follows: A straight beam with length $l = 16$ and height $h = 4$ is loaded with bending moments, M, at both ends. These are applied as linear distributed tractions, h_x, in x-direction, such that:

$$M = \int_{-\frac{h}{2}}^{\frac{h}{2}} h_x y \, \mathrm{d}y \tag{9.8}$$

A schematic is given in figure 9.4. The interface with frictionless sliding is located at the

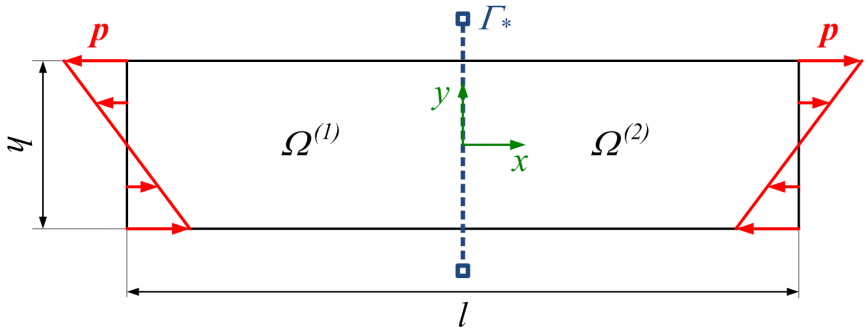

FIGURE 9.4: Schematic of domain and loading for pure bending example: Two grains divided by an embedded interface with linear line loads.

center of the rectangle and divides the domain into two grains, $\Omega^{(1)}$ and $\Omega^{(2)}$. The loads are applied by prescribing the analytical displacement solution on the left and right boundary. Thus, the bending is modelled as well as all rigid body modes are constrained without limiting the possibility of sliding at the interface. According to [40], the analytical solution

for the stress field can be obtained by introducing a stress function, $\varphi(x, y)$:

$$\varphi(x,y) = \frac{a}{6}x^3 + \frac{b}{2}x^2y + \frac{c}{2}xy^2 + \frac{d}{6}y^3 \tag{9.9}$$

The stresses are computed as derivatives of the stress function:

$$\begin{aligned} \sigma_{xx} &= \quad \varphi_{,yy} = \quad cx + dy \\ \sigma_{yy} &= \quad \varphi_{,xx} = \quad ax + by \\ \sigma_{xy} &= -\varphi_{,xy} = -bx - cy \end{aligned} \tag{9.10}$$

A pure bending case is obtained, if only d is unequal to zero. Here, d is chosen as $d = 2p/h$ with $p = 1$. Hence, there are no shear stresses in the system. The problem is a pure beam bending problem. Setting the parameters as indicated above, the Cauchy stress tensor becomes:

$$\underline{\boldsymbol{\sigma}} = \begin{bmatrix} \sigma_{xx} & \sigma_{xy} \\ \sigma_{xy} & \sigma_{yy} \end{bmatrix} = \begin{bmatrix} \frac{2p}{h}y & 0 \\ 0 & 0 \end{bmatrix} \tag{9.11}$$

A linear distribution of the stress σ_{xx} over y is expected everywhere in the domain and hence at the interface, too. The absolute maximum value is $|\sigma_{xx,max}| = |2p/h \cdot y_{max}| = |p| = 1$. Using (9.11), the reader can verify easily, that the Neumann boundary conditions are fullfilled, since $\sigma_{ij}n_j = h_i$ with n_j denoting the normal vector pointing outwards from the domain. Assuming a linear elastic constitutive law for a plane stress state, the strain tensor becomes [40]:

$$\underline{\boldsymbol{\varepsilon}} = \begin{bmatrix} \varepsilon_{xx} & \varepsilon_{xy} \\ \varepsilon_{xy} & \varepsilon_{yy} \end{bmatrix} = \begin{bmatrix} \frac{2p}{Eh}y & 0 \\ 0 & -\frac{2p\nu}{Eh}y \end{bmatrix} \tag{9.12}$$

where E denotes the Young's modulus and ν the Poisson's ratio. After integration of the strain field, using the compatibility equation, given by the shear strain, and including the boundary conditions, the displacement field can be written as:

$$\underline{\boldsymbol{u}} = \begin{bmatrix} u_x \\ u_y \end{bmatrix} = \begin{bmatrix} \frac{2p}{Eh}xy \\ -\frac{p}{Eh}(x^2 + \nu y^2) \end{bmatrix} \tag{9.13}$$

Name	Notation	Value
Young's modulus	E	1000.0
Poisson's ratio	ν	0.0

TABLE 3: Material properties for both grains for pure bending example for stability and convergence analysis

Mesh ID	Mesh size h	Elements	Base DOFs	All DOFs	Cut elements
1	0.506	252	308	336	12
2	0.279	820	924	968	20
3	0.141	3240	3444	3528	40
4	0.094	7260	7564	7688	60
5	0.070	12880	13284	13448	80
6	0.035	51360	52164	52488	160

TABLE 4: Different meshes for pure bending example for stability and convergence analysis

The stress tensor $\underline{\boldsymbol{\sigma}}$, the strain tensor $\underline{\boldsymbol{\varepsilon}}$ and the displacement field $\underline{\boldsymbol{u}}$ are used for error computation. The material properties are the same in both grains and are listed in table 3. The problem is solved using the three methods presented in section 5. Different structured meshes are used, which are listed in table 4. See figure 9.5 for example, where also the interface is drawn. The reference frame, used for simulation, has an offset 8 in x-direction

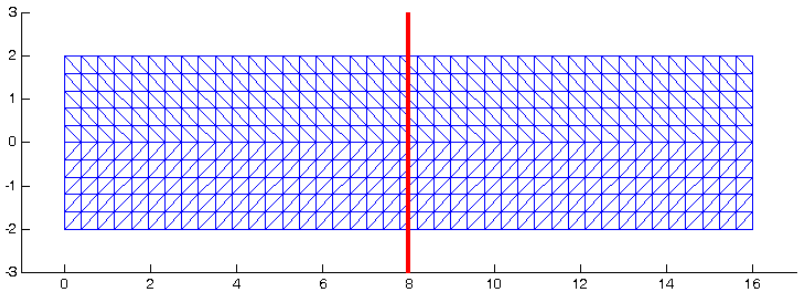

FIGURE 9.5: Meshed domain and interface with 820 triangular elements

compared to figure 9.4 to simplify the mesh generation. Of course, this is considered for the error computations. The order of simulations for the convergence study is as follows: First, all meshes are solved, using Lagrange multipliers. Then, all meshes are solved with Nitsche's method where the stabilization parameter is computed for each element separately using

Mesh ID	penalty parameter	Stabilization parameter
1	$9.00 \cdot 10^4$	$3.50 \cdot 10^3$
2	$2.95 \cdot 10^5$	$6.83 \cdot 10^3$
3	$1.17 \cdot 10^6$	$1.35 \cdot 10^4$
4	$2.62 \cdot 10^6$	$2.02 \cdot 10^4$
5	$4.64 \cdot 10^6$	$2.68 \cdot 10^4$
6	$1.85 \cdot 10^7$	$5.35 \cdot 10^4$

TABLE 5: Penalty parameters and stabilization parameters for each mesh

the estimate (4.88). Hence, the stabilization parameter scales $1/h$. Due to the symmetry of the problem, the estimate gives the same value for each element. Finally, the penalty method is used. The penalty parameter for the coarsest mesh is chosen such that the error in the displacement field takes the same value as for Nitsche's method. According to [4], it is scaled $1/h^2$ with h denoting the mesh size. The penalty parameters and Nitsche parameters used for each mesh are listed in table 5. The penalty parameters and stabilization parameters are plotted versus the mesh size h in figure 9.6, where it becomes obvious that the penalty parameter grows faster than the stabilization parameter for Nitsche's method with ongoing mesh refinement. The displacement field in the deformed state, obtained with Nitsche's

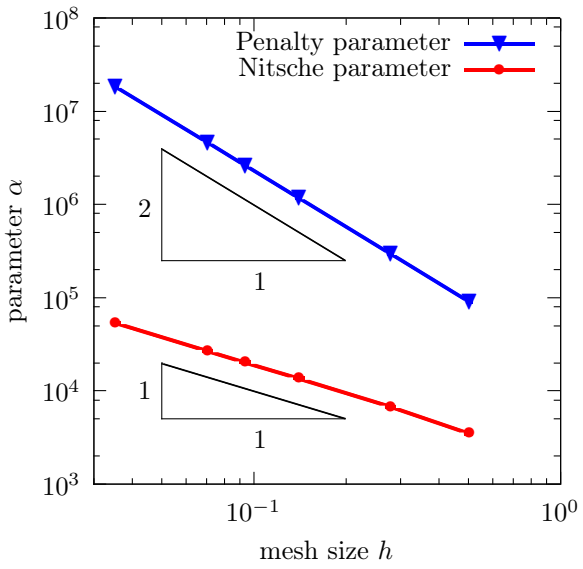

FIGURE 9.6: Penalty parameter and stabilization parameter for Nitsche's method for different mesh sizes: The penalty parameter scales $1/h^2$, the stabilization parameter for Nitsche's method scales $1/h$.

method, is shown in figure 9.7, where the deformation is scaled with the factor 100. The

contour plot is generated with respect to the x- and y-component of the displacement field. A plot of σ_{xx} is given in figure 9.8, obtained with Nitsche's method. The errors in the

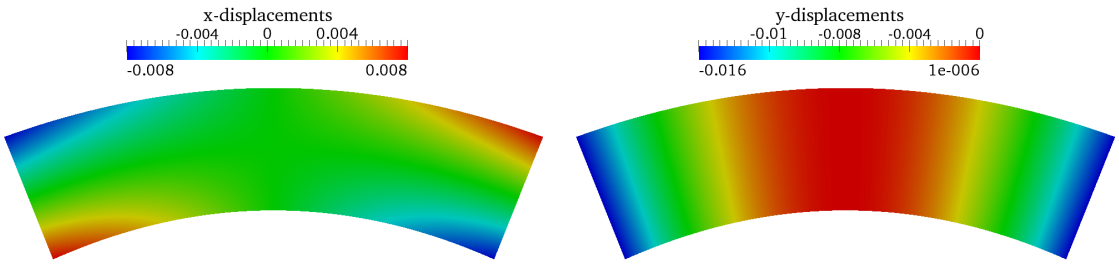

(a) x-component (b) y-component

FIGURE 9.7: Contour plot of displacement field in deformed state for structured mesh with 12880 elements. Deformation scaled by factor 100

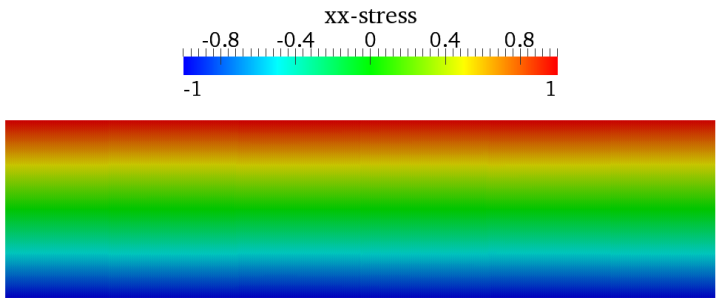

FIGURE 9.8: Distribution of σ_{xx} in the beam for mesh 5

displacement field, the energy norm and the traction field are plotted in figure 9.9. The error in the displacement field decreases for all three methods with the same convergence rate of 2 which is the optimal one. For classical finite elements, see [48], for Lagrange multipliers, see [3], for penalty method, see [4], for Nitsche's method, see [39]. In the energy norm, an optimal convergence rate of only 1 can be expected since the energy norm is based on the derivatives of the displacement field. All three methods converge with the optimal convergence rate in the energy norm. Differences can be seen in the error in the traction field. The Lagrange multiplier method does not converge due to the oscillations in the traction field. The penalty method converges, but not with the optimal convergence rate of 1. This is not suprising since there is no guarantee of optimal convergence rates for the penalty method [4]. However, for Nitsche's method optimal convergence rates are expected. This

Mesh ID	error in displacement field	error in energy norm	error in traction field
1	0.005266	0.329150	4.268300
2	0.001684	0.184540	7.497100
3	0.000504	0.092915	15.32840
4	0.000250	0.062086	23.09930
5	0.000154	0.046618	30.85620
6	0.000049	0.023348	61.85400

TABLE 6: Numerical values for convergence study and error analysis for the Lagrange multiplier method

Mesh ID	error in displacement field	error in energy norm	error in traction field
1	0.005243	0.327790	0.540160
2	0.001656	0.184050	0.358190
3	0.000495	0.092779	0.211960
4	0.000246	0.062023	0.152850
5	0.000152	0.046582	0.122670
6	0.000049	0.023338	0.072650

TABLE 7: Numerical values for convergence study and error analysis for the penalty method

expectation is fullfilled also in the traction field where Nitsche's method converges with the optimal rate of 1. Differences in the accuracy are only identified in the traction field since the penalty parameter was chosen such that there is no difference in the error in the displacement field. As mentioned above, the representation of the traction field with Lagrange multipliers is really bad due to the stability issues. The penalty method represents the traction field quite well but the accuracy is much less than with Nitsche's method. Hence, Nitsche's method has another advantage over the penalty method besides the slower increase of the stabilization parameter: The accuracy is much better in the traction field for the same error in the displacement field. For the sake of completeness, all values are given in tables 6, 7 and 8 where they are rounded to six digits. In order to show the oscillations, the traction fields for all methods are plotted in figure 9.10 for mesh 5. The analytical solution is drawn as a red line. One can see clearly the oscillations for the Lagrange multiplier method. The best approximation of the traction field is done by Nitsche's method.

Mesh ID	error in displacement field	error in energy norm	error in traction field
1	0.005249	0.326620	0.204120
2	0.001667	0.183830	0.112270
3	0.000502	0.092744	0.053135
4	0.000250	0.062012	0.034740
5	0.000154	0.046576	0.025795
6	0.000049	0.023338	0.012701

TABLE 8: Numerical values for convergence study and error analysis for Nitsche's method

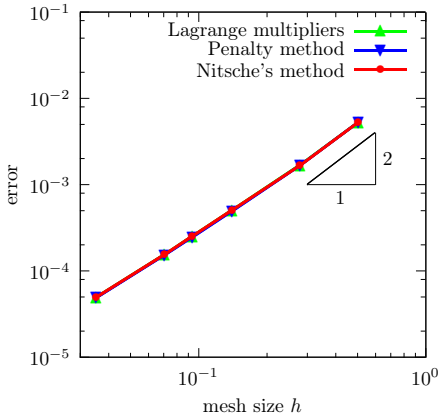

(a) Displacement field

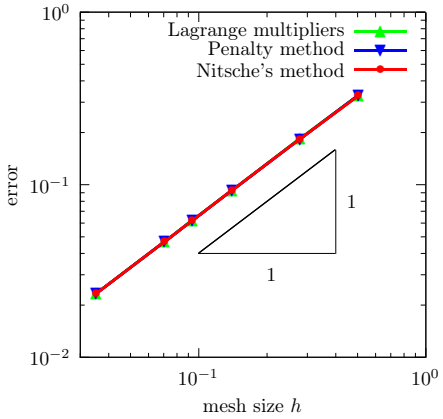

(b) Energy norm

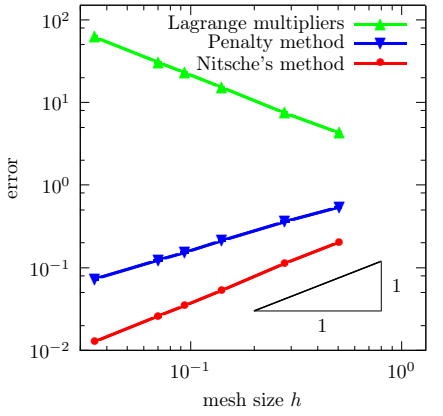

(c) Traction field

FIGURE 9.9: Convergence plots for errors in displacement field, energy norm and traction field for Lagrange multipliers, penalty method and Nitsche's method

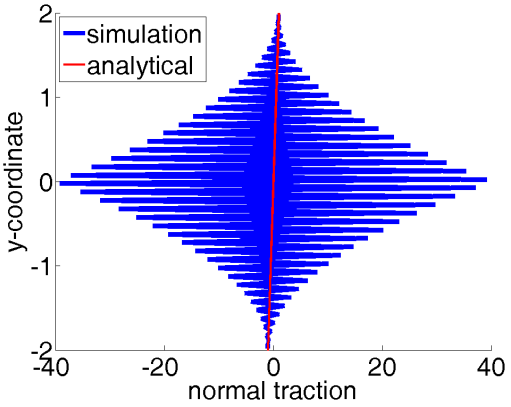

(a) Lagrange multipliers

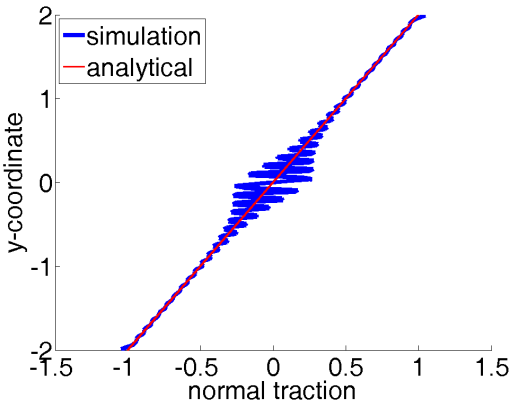

(b) Penalty method ($\alpha = 4.64 \cdot 10^6$)

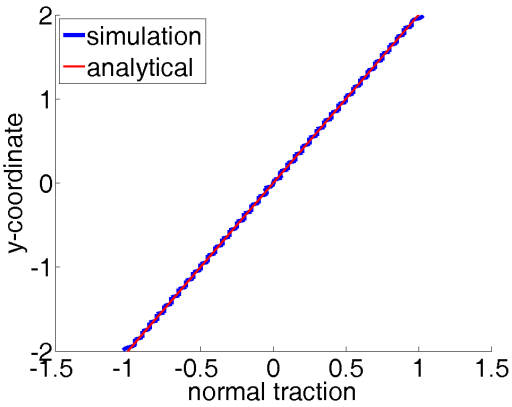

(c) Nitsche's method with stabilization parameter estimated using (4.88)

FIGURE 9.10: Traction field along interface Γ_* for all three methods for mesh 5 for the pure bending example

9.2.3 Free grain boundary sliding in a polycrystal

An often used model to examine inelasticity in polycrystals based on grain boundary sliding is a periodic array of hexagonal grains. It was introduced in [47]. Some finite element analysis has been performed in [16, 42]. The setup of this example is very similar to the one given in [38]. However, the examples in the literature often use dynamic simulations and a viscous law for the grain boundary sliding. This is not the case, here. So, only a qualitative match of the results is expected. Due to the periodicity, the latter authors suggest to restrict the domain to an unit cell, see figure 9.11. The unit cell is supported with loose bearings

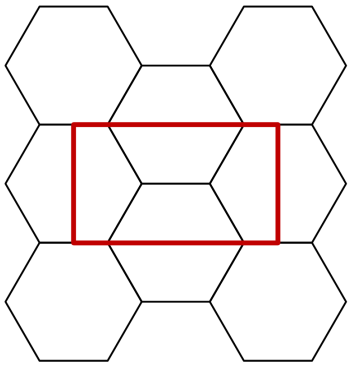

FIGURE 9.11: Hexagonal polycrystals with unit cell as given in [42]

on three sides, whereas the fourth side will be subjected to a small prescribed displacement, g_x. A sketch of the domain and the boundary conditions is provided in figure 9.12. Here,

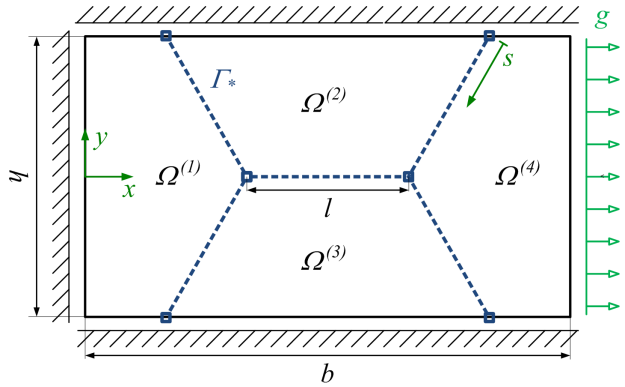

FIGURE 9.12: Schematic of domain, boundary conditions and prescribed displacements for an example with free grain boundary sliding: Four grains divided by five embedded interfaces with prescribed displacements as load.

Mesh size h	Elements	Base DOFs	All DOFs	Cut elements
0.020408	14406	14800	15596	390

TABLE 9: Structured mesh for grain boundary sliding example

the dimensions are chosen as $l = 1$, $b = 3$ and $h = \sqrt{3}$. The prescribed displacement in x-direction is $g_x = 3 \cdot 10^{-6}$, such that the resulting strain in x-direction is $\varepsilon_{xx} = 10^{-6}$. For all grains $\Omega^{(m)}$, $m \in \{1, 2, 3, 4\}$, a linear elastic material with Young's modulus $E^{(m)} = 1000$ and Poisson's ratio $\nu^{(m)} = 0.3$ is used. A structured mesh with 14406 elements is applied to the unit cell, where the mesh density is adopted from [38]. The grain boundaries are represented by embedded interfaces, where the formulation for frictionless sliding is used. Mesh and interfaces are depicted in figure 9.13. To enforce the constraints at the interfaces, a penalty method with $\alpha = 4.25 \cdot 10^6$ is used, which is 10^2 times the biggest value of the elastic stiffnes matrix. The mesh data are summarized in table 9. A contour plot of the absolute

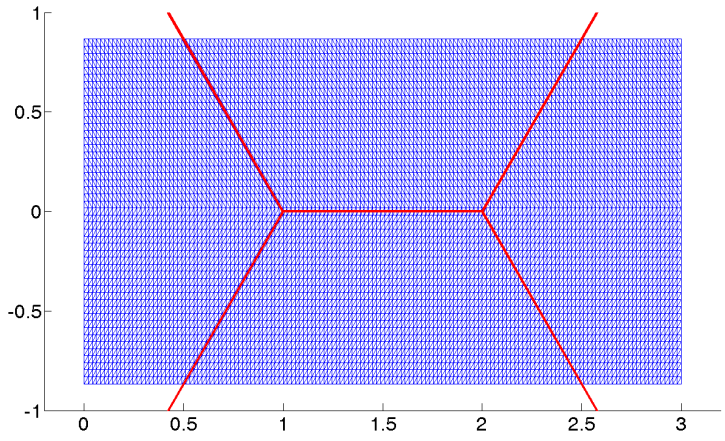

FIGURE 9.13: Meshed domain with interfaces for grain boundary sliding

values of the displacement field is presented in figure 9.14 as well as one of the distribution of the von-Mises-stress. The jumps due to the tangential gap at the interfaces can be seen clearly in the displacement field. Of course, the horizontal interface shows no jump in the displacements, which is expected. The tangential gap along the auxiliary coordinate s (see figure 9.12) is shown in figure 9.15 and takes the same form as in [38]. The distribution of the von-Mises-stress matches the ones provided in [38, 42] very well. The high stress concentrations at the triple junctions are also expected since only these points prevent the grains from totally sliding apart.

The example can also be solved, using Lagrange multipliers or Nitsche's method. Then, the same results are obtained.

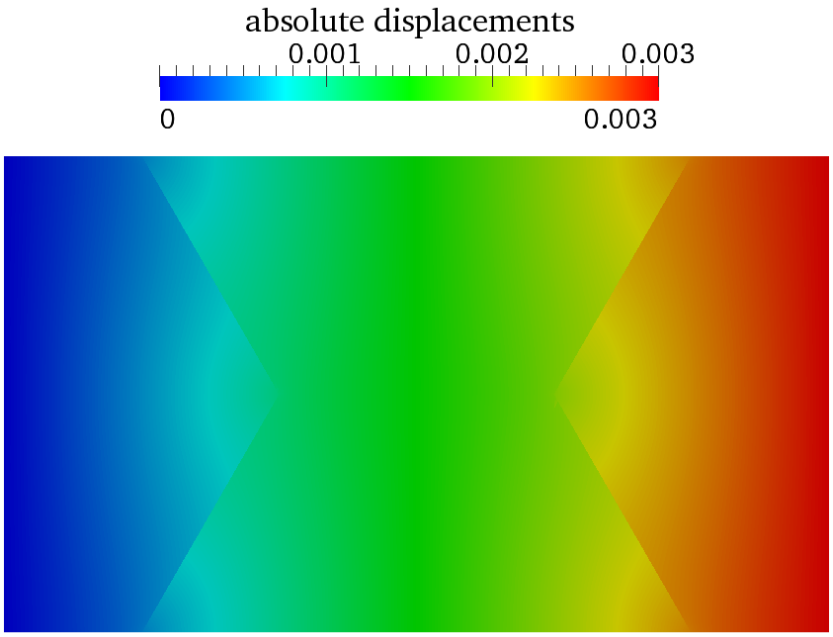

(a) Absolute displacements

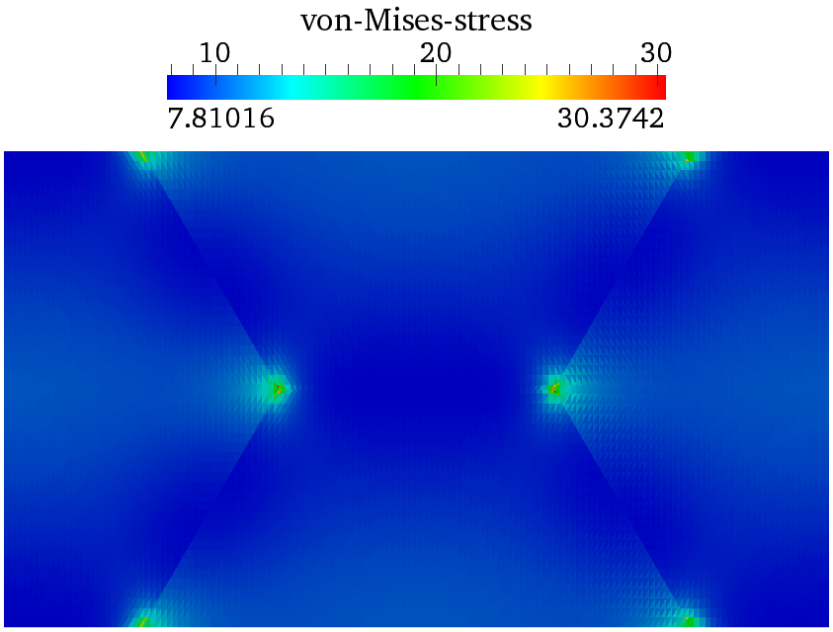

(b) von-Mises-stress

FIGURE 9.14: Contour plots for results of the grain boundary sliding example

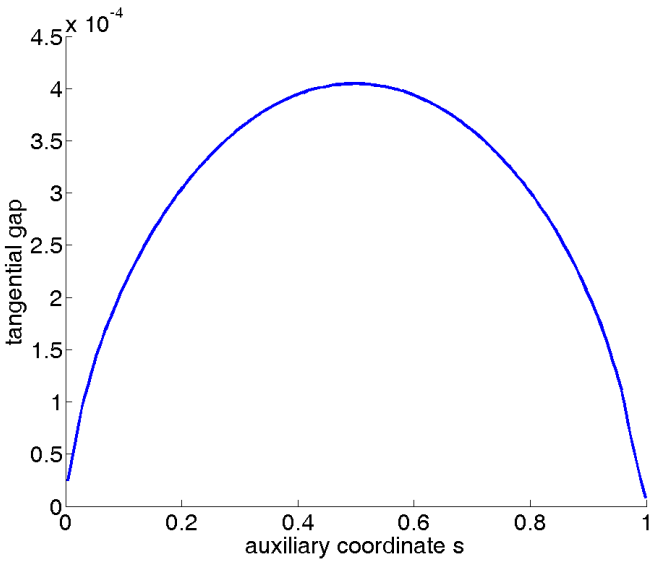

FIGURE 9.15: Tangential gap along the auxiliary coordinate s for free grain boundary sliding

9.3 Numerical examples for perfect plasticity

Some examples with perfect plasticity in tangential direction are presented. They are all solved using the methods described in section 6. First, a model problem for plasticity, similar to the one from section 9.2.1, is investigated. Afterwards, an example similar to frictional contact is considered where the solution can be compared to one obtained with a very fine mesh without interface. Then, the grain boundary sliding example from section 9.2.3 is solved with different yield stresses. Finally, a polycrystalline specimen is modelled, that is subjected to a pure shear load. This example shows the capability of the method to handle many grains and interfaces as well as reproduces some physical properties of polycrystalline material.

9.3.1 Model problem with perfect plasticity

The example from section 9.2.1 is used again. A sketch of the domain is depicted in figure 9.4, the material properties are listed in table 1. It is recalled that both grains have different Poisson's ratios such that transversal contraction is enabled in grain $\Omega^{(1)}$, whereas it is disabeld in grain $\Omega^{(2)}$. The Dirichlet boundary conditions are the same as before, but the load is increased to $p = -25$. Using a similar procedure as for the example with frictionless sliding, the total elongation can be determined to $\triangle l = -0.4$. A structured mesh is used. The mesh data is summarized in table 10. The mesh with interface is shown in figure 9.16. The penalty parameter for normal direction chosen as $\alpha_n = 5.0 \cdot 10^4$, the one for the tangential direction as $\alpha_t = 8 \cdot 10^3$, such that the traction in the elastic regime does not show severe oscillations. The external load is applied in 20 equally sized load steps and decreased to zero in 20 equally sized steps, afterwards. The example is solved with six different yield tractions, $h^y_{t,i}$, listed in table 11. The first one is chosen to be equal to zero. It is expected that the results are similar to the ones from the example with frictionless sliding. The other yield tractions are chosen in an increasing order. The last one is chosen so high that the entire interface remains in the elastic regime. These results are expected to match the results, one would obtain for a fully tied problem. Due to plasticity, it is expected that a deformation remains after removing the load. Since the problem is symmetric to the

Mesh size h	Elements	Base DOFs	All DOFs	Cut elements
0.157	2592	2774	2850	36

TABLE 10: Data for structured mesh

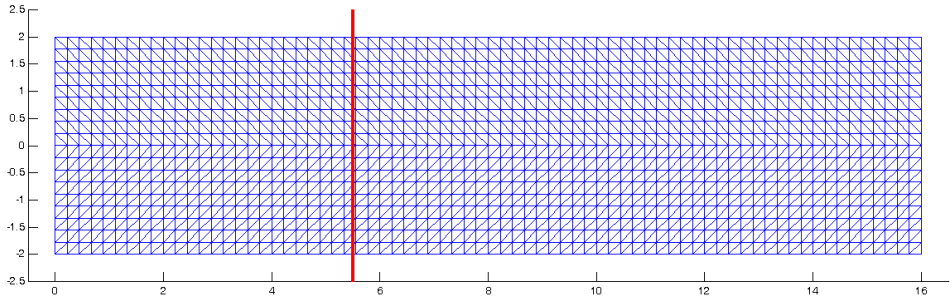

FIGURE 9.16: Structured mesh with interface for model problem for perfect plasticity

$h^y_{t,i}$	Yield traction
$h^y_{t,1}$	0.0
$h^y_{t,2}$	0.5
$h^y_{t,3}$	1.0
$h^y_{t,4}$	2.0
$h^y_{t,5}$	3.0
$h^y_{t,6}$	10^{12}

TABLE 11: Different yield tractions

x-axis, the results are expected to be symmetric to the x-axis, too. The x-components of the displacement fields are plotted as contour plots in the deformed state under the full load in figure 9.17, where the deformation is scaled with the factor 10. The y-components of the displacement field are shown in figure 9.18, respectively. As expected, the displacement fields are symmetric to the x-axis. For the case with $h^y_{t,1} = 0.0$ can be seen, that the y-component of the displacement field in grain $\Omega^{(1)}$ is totally decoupled from the displacement field in $\Omega^{(2)}$ as it was in the modified patch test with frictionless sliding (see figure 9.3). The discontinuities in the displacement field decrease with an increasing yield traction. The evolution of the *stick-slip-zone* during the increase of the load is depicted in figure 9.19 for all the different yield tractions. The vertical interface is plotted at the end of each loadstep. Therefor, each subsegment is divided into two parts, each containing one Gauß point. Each part of a subsegment is colored with respect to the sign of Φ^{trial}_{k+1}. A blue colored part means that the trial state is admissible at this Gauß point, i.e. $\Phi^{trial}_{k+1} \leq 0$. A red colored part means that the trial state is not admissible at this Gauß point, i.e. $\Phi^{trial}_{k+1} > 0$. The horizontal axis corresponds to the normalized pseudo-time. So, the first line on the left belongs to the first load step and the last line on the right shows the stick-slip-zone when the entire load is applied. The stick-slip-zones are symmetric to the x-axis. The tangential traction is plotted

in figure 9.20 for all the different yield tractions for both methods. The penalty method does not show severe oscillations, since the penalty parameter was chosen small enough. The tangential traction field for the stabilized method shows an oscillatory pattern, which does not stem from stability issues at the interface but — according to [33] — from the underlying mesh since linear triangular elements are used.

Remark 9.1. *The oscillatory pattern in the stabilized method can also be seen in the fully tied problem, investigated in [33]. There, results for a cantilever beam problem are compared to an analytical solution. The traction field in the normal direction is represented very well for Nitsche's method, whereas the tangential traction field shows some oscillations around the analytical solution. These oscillations basically occur in the shear field and hence in the traction field for Nitsche's method, since it is directly influenced by the stress field. The oscillatoric behaviour of the shear field can also be seen for classical finite elements without any interfaces with linear triangular elements.*

After removing the load, a plastic deformation remains, if plasticity was activated during the loading process. The remaining plastic deformation in y-direction is depicted in figure 9.21. For the case with $h^y_{t,1} = 0.0$, that is equal to frictionless sliding, and for $h^y_{t,6} = 10^{12}$, that is equal to a fully tied interface, no plastic deformation remains, as expected. For the other cases, the plastic deformation is the greater, the lower the yield traction is since a lower yield traction results in a larger slip zone.

(a) x-component for $h^y_{t,1} = 0.0$

(b) x-component for $h^y_{t,2} = 0.5$

(c) x-component for $h^y_{t,3} = 1.0$

(d) x-component for $h^y_{t,4} = 2.0$

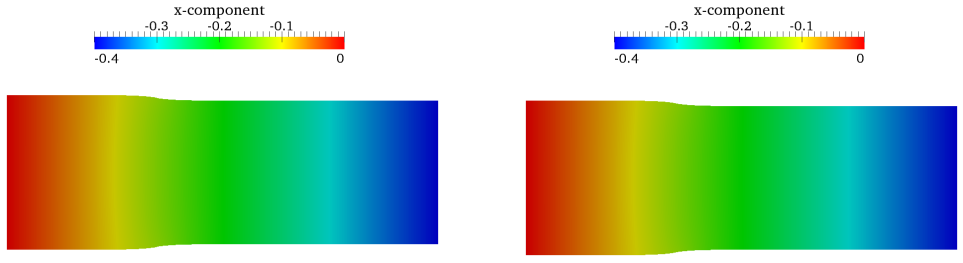

(e) x-component for $h^y_{t,5} = 3.0$

(f) x-component for $h^y_{t,6} = 10^{12}$

FIGURE 9.17: Contour plots for x-components of the displacement fields under the full load for the model problem with different yield tractions. The x-component of the displacement field is continuous at the interface. The deformation is scaled with factor 10.

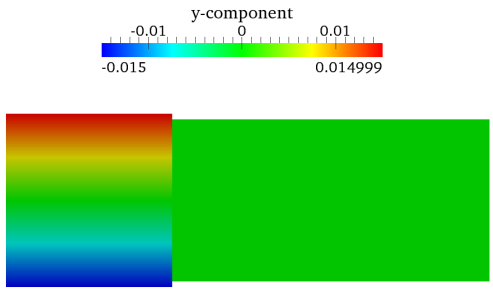

(a) y-component for $h^y_{t,1} = 0.0$

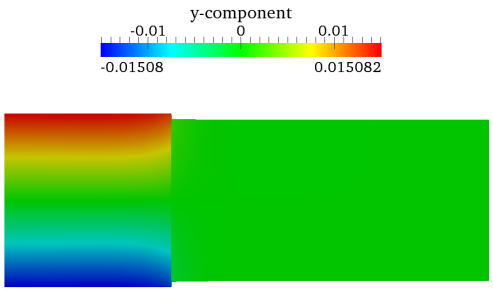

(b) y-component for $h^y_{t,2} = 0.5$

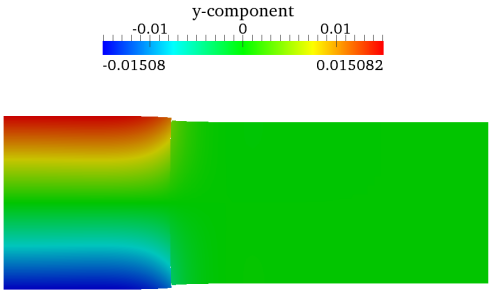

(c) y-component for $h^y_{t,3} = 1.0$

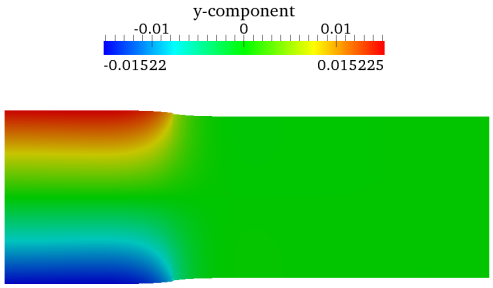

(d) y-component for $h^y_{t,4} = 2.0$

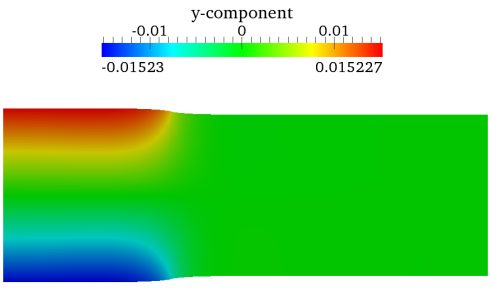

(e) y-component for $h^y_{t,5} = 3.0$

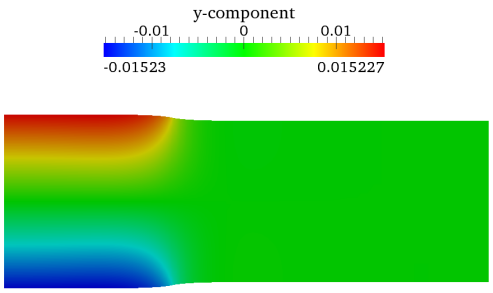

(f) y-component for $h^y_{t,6} = 10^{12}$

FIGURE 9.18: Contour plots for y-components of the displacement fields under the full load for the model problem with different yield tractions. The y-component of the displacement field can be discontinuous at the interface, depending on the yield traction. The deformation is scaled with factor 10.

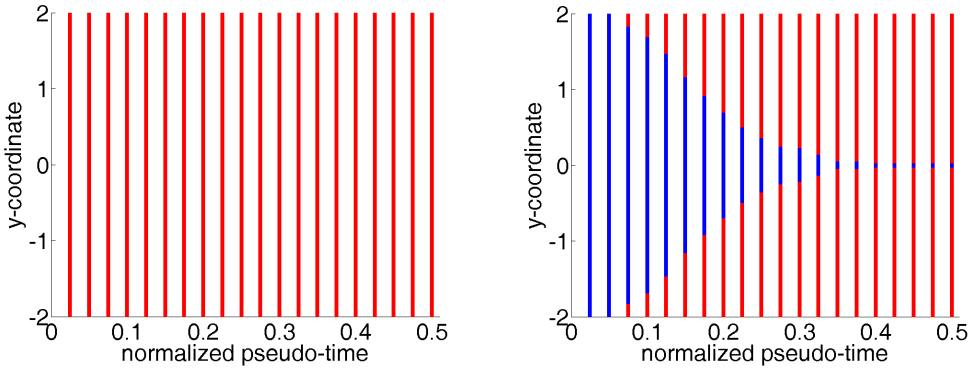

(a) $h^y_{t,1} = 0.0$

(b) $h^y_{t,2} = 0.5$

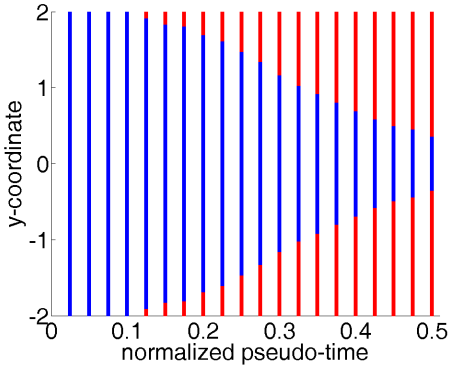

(c) $h^y_{t,3} = 1.0$

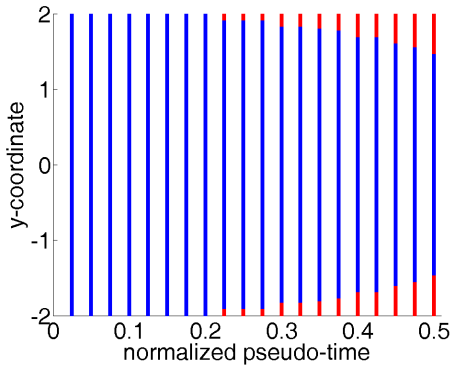

(d) $h^y_{t,4} = 2.0$

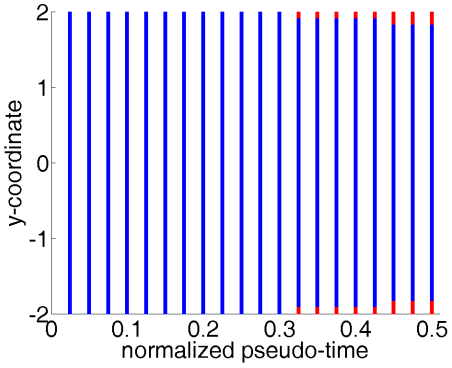

(e) $h^y_{t,5} = 3.0$

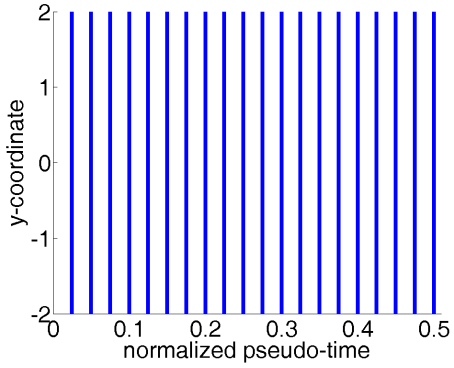

(f) $h^y_{t,6} = 10^{12}$

FIGURE 9.19: Evolution of the stick-slip-zone during loading process for the model problem with different yield tractions. The horizontal axis shows the normalized pseudo-time, the vertical axis the y-coordinate of the interface. Subsegments in stick are colored blue, subsegments in slip are colored red.

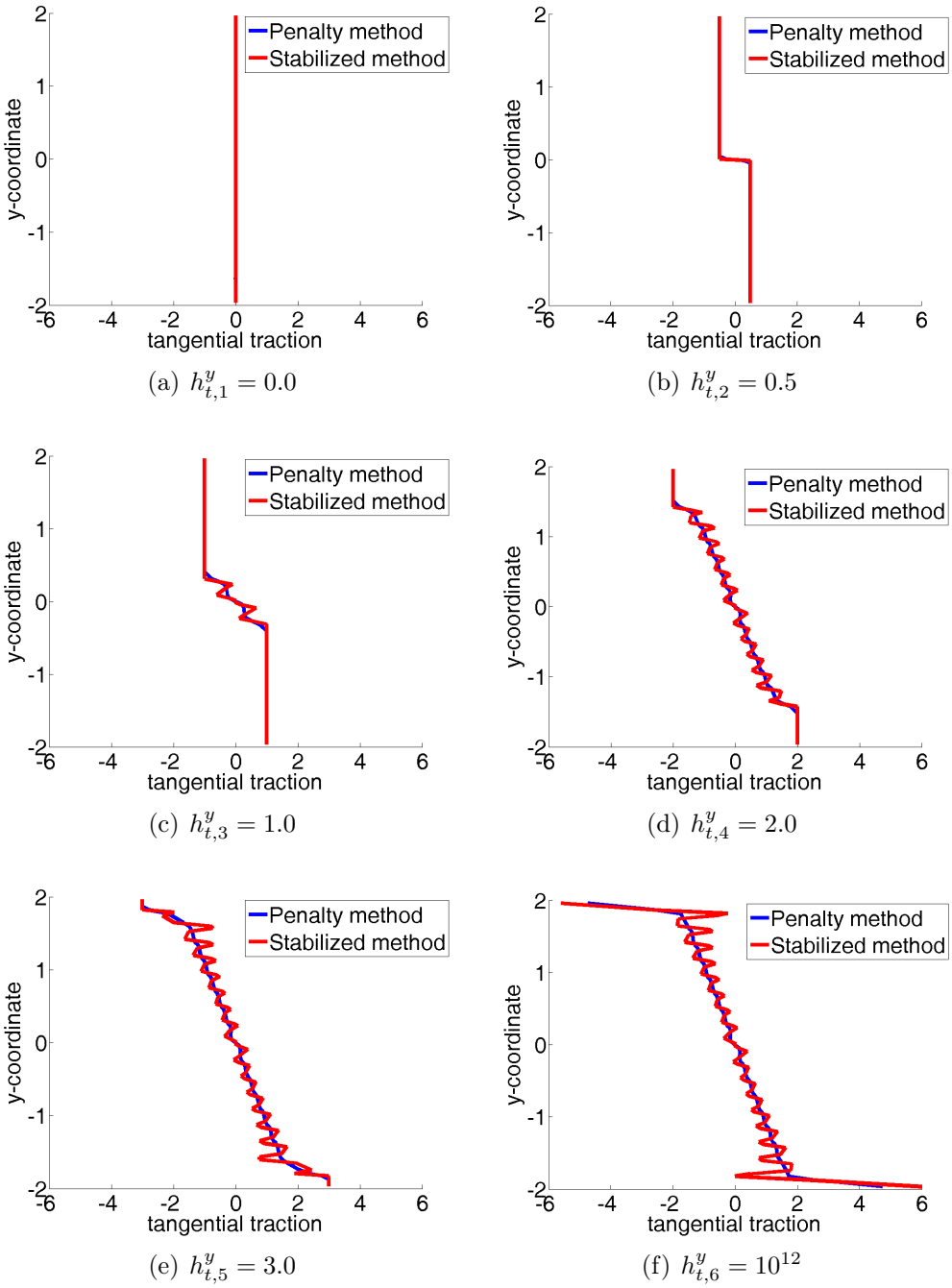

(a) $h^y_{t,1} = 0.0$ (b) $h^y_{t,2} = 0.5$

(c) $h^y_{t,3} = 1.0$ (d) $h^y_{t,4} = 2.0$

(e) $h^y_{t,5} = 3.0$ (f) $h^y_{t,6} = 10^{12}$

FIGURE 9.20: Tangential traction at the interface for different yield tractions. For an detailed explanation for the oscillations of the stabilized method, see [33].

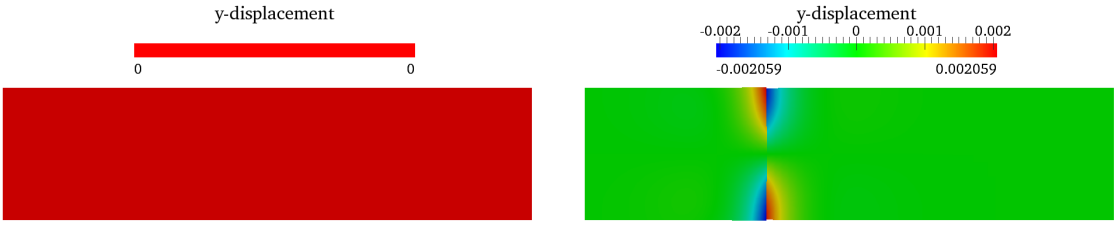

(a) y-component for $h^y_{t,1} = 0.0$

(b) y-component for $h^y_{t,2} = 0.5$

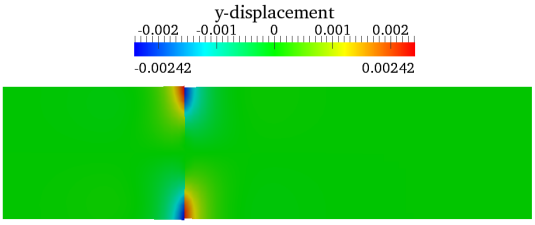

(c) y-component for $h^y_{t,3} = 1.0$

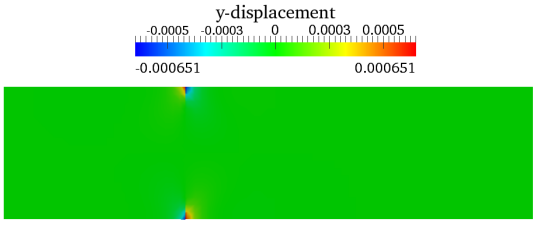

(d) y-component for $h^y_{t,4} = 2.0$

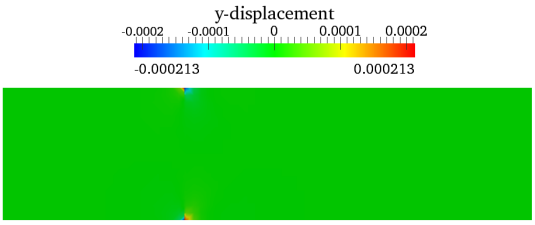

(e) y-component for $h^y_{t,5} = 3.0$

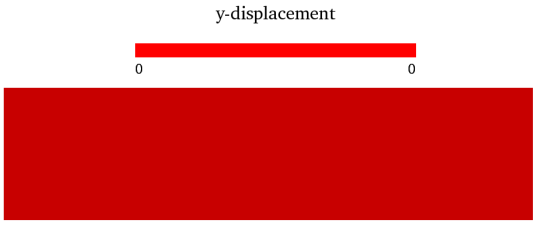

(f) y-component for $h^y_{t,6} = 10^{12}$

FIGURE 9.21: Contour plots for remaining plastic deformation in y-direction after the unloading process for the model problem with different yield tractions. The deformation is scaled with factor 10.

9.3.2 "Frictional" sliding of an elastic block on a rigid surface

In this example, an elastic block is pressed on a rigid surface with a prescribed displacement, $g_1 = -0.01$, and then moved transversal with a prescribed displacement, $g_2 = 0.005$. A sketch of the domain and its loads is given in figure 9.22. The vertical displacement is imposed within 5 load steps, the tangential displacement within 20 load steps. The load curves are shown in figure 9.23, where the horizontal axis shows the load steps. The rigid surface is represented by grain $\Omega^{(2)}$, whose Young's modulus is chosen very high in comparison to the one in the elastic block. In addition, all degrees of freedoms of not enriched nodes in $\Omega^{(2)}$ are fixed by Dirichlet boundary conditions. Grain $\Omega^{(1)}$ represents the elastic block with Young's modulus $E^{(1)} = 1000$. All material data are summarized in table 12. The yield traction is chosen as $h_t^y = 0.25$. Since the bottom block in figure 9.22a is assumed to be rigid, the displacement field is knwon *a priori*. Hence, one is only interested in the solution for the elastic block. If the prescribed horizontal displacement is large enough, so that the entire interface is in slip, a reference solution can be constructed, using a domain as depicted in figure 9.22b. For the reference solution, the elastic block is fixed at its upper boundary. At

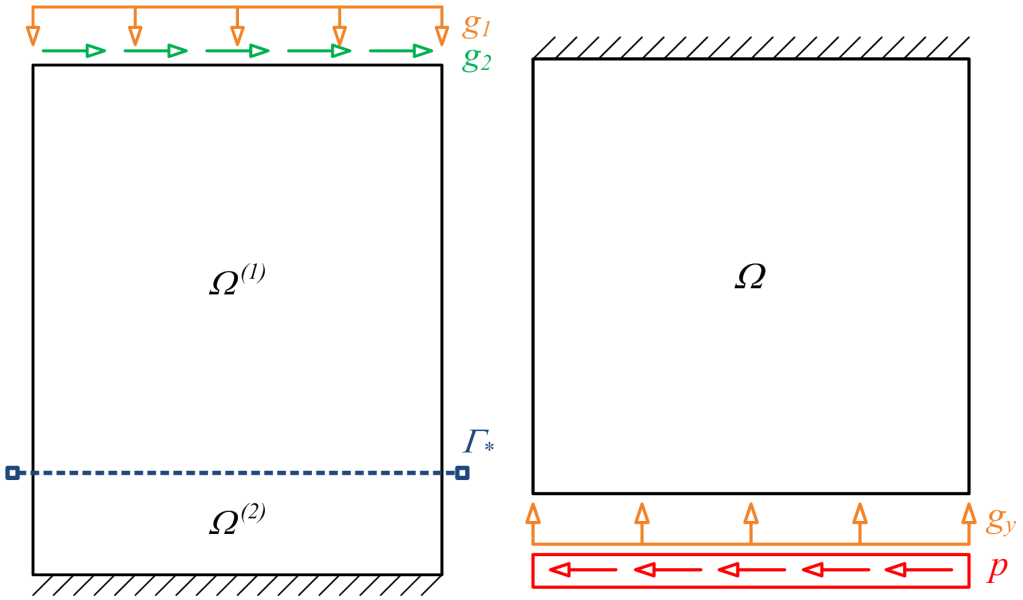

(a) Domain with emebedded interface with perfect plasticity

(b) Domain for reference solution

FIGURE 9.22: Domain, boundary conditions and prescribed displacements for a "frictional" sliding problem and the corresponding domain to compute a reference solution with classical finite elements

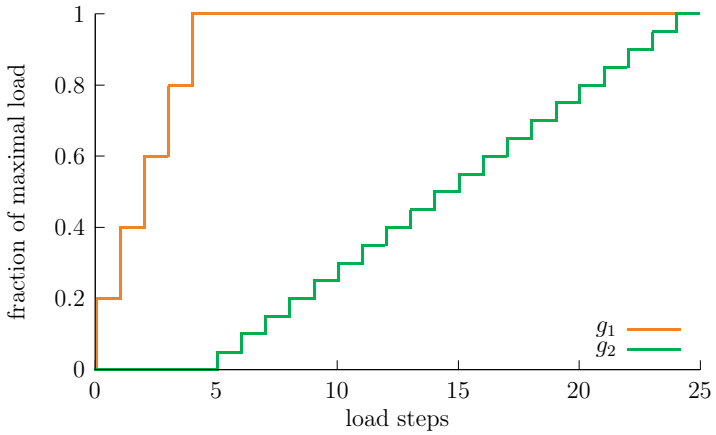

FIGURE 9.23: Load curves for prescribed displacements. First, the vertical displacement g_1 is imposed, then the horizontal displacement g_2.

Name	Notation	value
Young's modulus in $\Omega^{(1)}$	$E^{(1)}$	$1.0 \cdot 10^3$
Young's modulus in $\Omega^{(2)}$	$E^{(2)}$	$1.0 \cdot 10^{15}$
Poisson's ratio in $\Omega^{(1)}$	$\nu^{(1)}$	0.0
Poisson's ratio in $\Omega^{(2)}$	$\nu^{(2)}$	0.0

TABLE 12: Material properties for frictional sliding with Tresca friction

first, the bottom boundary is moved in positive y-direction, corresponding to the prescribed y-displacement, $g_y = -g_1 = 0.01$. Then, a horizontal external traction is applied at the bottom boundary representing the yield traction in a fully sliding interface. So, its value is chosen equal to the yield traction: $|p| = h_t^y = 0.25$. Of course, there is an offset in the displacement field which equals the prescribed horizontal displacement which can be respected with a translation of the reference frame. The domain for the reference solution does not contain any interface. So, it can be solved with classical finite elements. Optimal convergence rates are expected. A mesh with 51842 elements is used to compute the reference solution. A brief convergence study shows, that this is sufficiently fine in the sense, that the absolute value of the x-displacement does not change significantly with further refinement. This is shown in figure 9.24, where the absolute value of the x-displacement of both corners is plotted versus the inverse of the mesh size h. The finest mesh shown in figure 9.24 is chosen to compute the reference solution[1]. The problem, that contains an embedded interface, can be solved for different meshes and for the penalty method and the stabilized method with

[1]In this study, it is not possible to use a finer mesh due to limitations in the computational resources, but this one seems to be sufficiently fine.

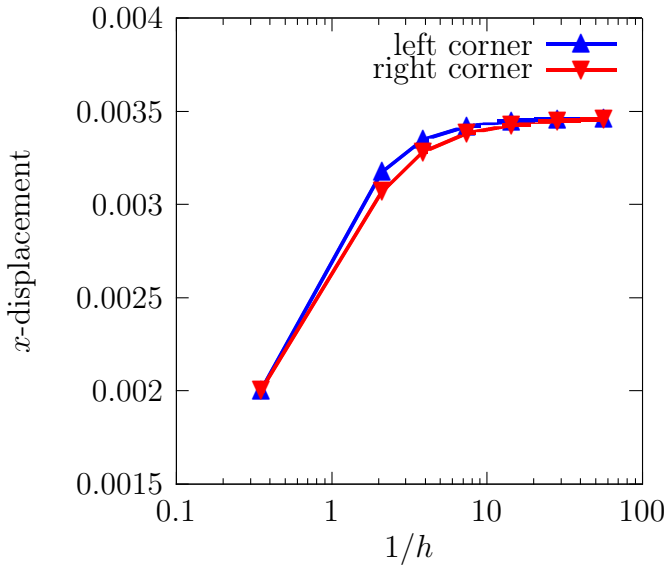

FIGURE 9.24: Convergence plot for absolute values of x-displacements of the two bottom corners of the reference problem

Mesh ID	Mesh size h	Elements	Base DOFs	All DOFs	Cut elements
1	0.13283	1134	1232	1320	42
2	0.06916	4182	4368	4536	82
3	0.03496	16362	16728	17056	162
4	0.02803	25452	25908	26316	202

TABLE 13: Data for structured meshes for the "frictional" sliding example

plasticity. The accuracy of both methods can be analysed by computing the $\mathbb{L}_2$-norm of the error in the displacement field, whereby the reference solution is used. Data about the meshes to solve the plasticity problem are summarized in table 13. According to [4], the penalty parameter has to be scaled by $1/h^2$. The normal penalty parameter is chosen as high as possible, but such, that no oscillations appear in the normal traction field. It takes the value $\alpha_n = 5.00 \cdot 10^4$ for the coarsest mesh. In order to choose a tangential penalty parameter for the coarsest mesh, a parameter study is done, which shows, that the error in the displacement field does not depend on the tangential penalty parameter as soon as it is high enough that the entire interface is in slip. The error in the displacement field is plotted over the tangential penalty parameter in figure 9.25. Higher parameters as used in figure 9.25 prevent the Newton scheme from converging. Hence, the tangential penalty parameter for the coarstest mesh is chosen as $\alpha_t = 5.00 \cdot 10^4$. The penalty parameters for all meshes are listed in table 14. For the stabilized method, the estimate (4.88) is used to determine

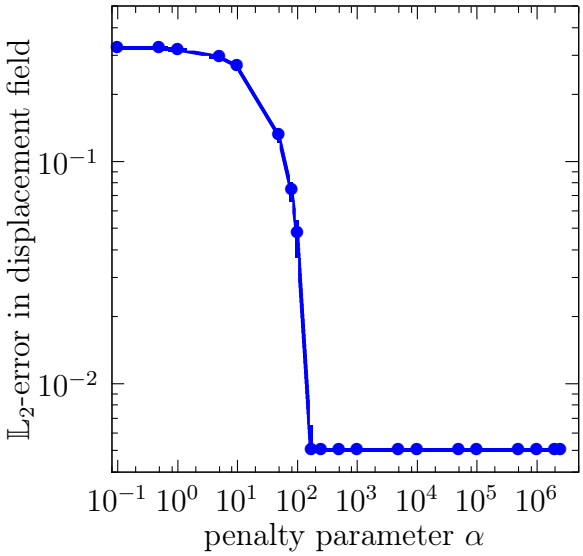

FIGURE 9.25: Parameter study to chose the tangential penalty parameter for the coarsest mesh. Penalty parameter varies between 0.1 and $2.6 \cdot 10^6$.

Mesh ID	normal penalty parameter α_n	tangential penalty parameter α_t
1	$5.00 \cdot 10^4$	$5.00 \cdot 10^4$
2	$1.84 \cdot 10^5$	$1.84 \cdot 10^5$
3	$7.22 \cdot 10^5$	$7.22 \cdot 10^5$
4	$1.12 \cdot 10^6$	$1.12 \cdot 10^6$

TABLE 14: Normal and tangential penalty parameters for different meshes

the stabilization parameter for both normal and tangential direction. Since one grain is much stiffer than the other, the average operator (4.29) has to be modified. In addition, the influence of the stiffer grain is removed from the estimate. A contour plot of the x- and y-component of the displacement field is given in figure 9.26. The error in the displacement field, measured in the $\mathbb{L}_2$-norm, is plotted in figure 9.27 for the different meshes and both methods. The slightly higher convergence rate with the fine mesh is purely artificial since the mesh size takes almost the same magnitude of the one, used to compute the reference solution. Both methods reach the same optimal convergence rate, but the stabilized method is more accurate. The accuracy of the penalty method cannot be improved as shown in figure 9.25.

In this particular example, the influence of the penalty parameter is not that important but in genereal the results for the penalty method is sensitive to the coice of the penalty parameter [4]. The stabilization parameter can be estimated using (4.88). This estimate is

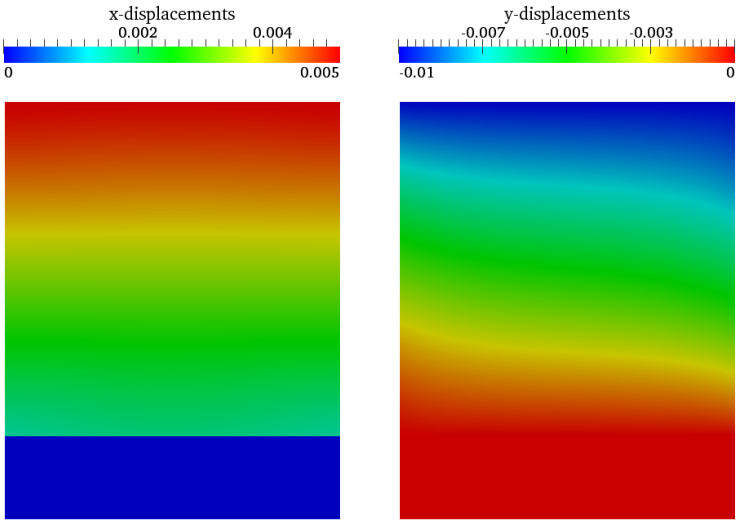

(a) x-component (b) y-component

FIGURE 9.26: Contour plot of x- and y-component of the displacement field for the stabilized method using mesh 3.

based only on the mesh and the material properties. It is determined by the problem and the user cannot choose a "bad" parameter. Bottom line, this example showes two advantages of the stabilized method: Firstly, it is more accurate than the penalty method. Secondly, there is no free parameter that has to be chosen by the user.

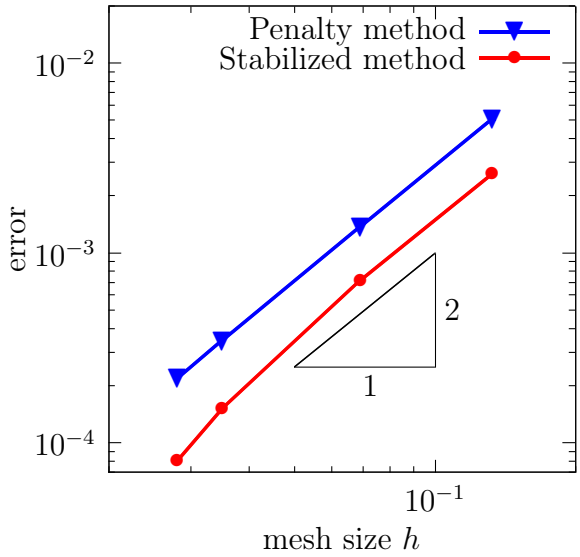

FIGURE 9.27: Error in the displacement field for penalty and stabilized method. The stabilized method is shown to be more accurate than the penalty method. The slightly higher convergence rate at finer meshes is artificial due to comparison to a solution obtained with a fine mesh.

9.3.3 Grain boundary sliding with perfect plasticity

The grain boundary sliding example from section 9.2.3 is revisited. Perfect plasticity in tangential direction is introduced at all interfaces. The penalty method as well as the stabilized method are used to enforce the constraints at the interfaces. The normal and tangential penalty parameters are chosen as $\alpha_n = \alpha_t = 4.25 \cdot 10^6$, again. The stabilization parameter is estimated, using (4.88). The problem is solved with different yield tractions, listed in table 15. The results for $h^y_{t,1} = 0.0$ are the same as in the frictionless sliding case from section 9.2.3. For $h^y_{t,5} = 5.0$, no plasticity occurs. The stress field is constant throughout

$h^y_{t,i}$	Yield traction
$h^y_{t,1}$	0.0
$h^y_{t,2}$	1.0
$h^y_{t,3}$	2.0
$h^y_{t,4}$	3.0
$h^y_{t,5}$	5.0

TABLE 15: Different yield tractions for the grain boundary sliding example with perfect plasticity

the entire domain. There is no discontinuity in the displacement field. For $h^y_{t,2} = 1.0$ and $h^y_{t,4} = 3.0$, the von-Mises-stress in the domain is plotted in figure 9.28 whereby the simulations are done using the stabilized method. The higher the yield traction is chosen, the

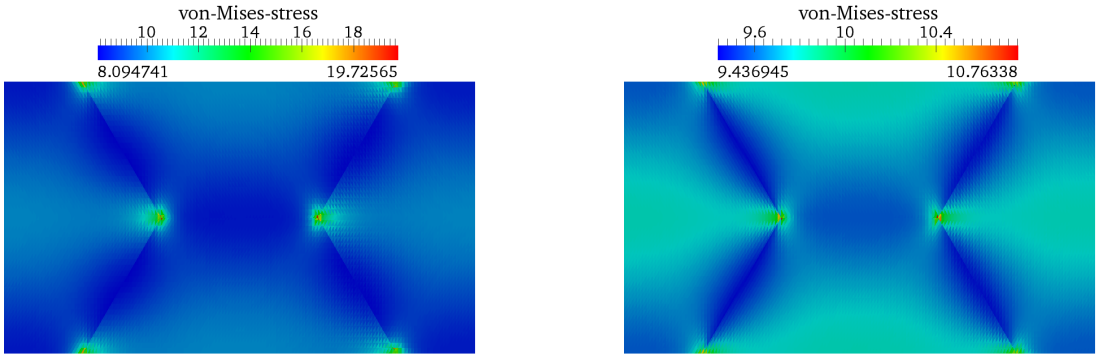

(a) $h^y_{t,2} = 1.0$ (b) $h^y_{t,4} = 3.0$

FIGURE 9.28: Distribution of the von-Mises-stress for different yield tractions. The peaks at the triple junctions are reduced with higher yield tractions.

smaller the stress peaks at the triple junctions are. The tangential gap along the auxiliary coordinate s, defined in figure 9.12, is plotted for all yield stresses in figure 9.29 where the penalty method is used. It can be seen, that the results for $h^y_{t,1} = 0.0$ are the same as in figure 9.15. For the highest yield traction $h^y_{t,5} = 5.0$, there is no tangential gap, anymore. The tangential gap for yield tractions in between decreases with an increasing yield traction.

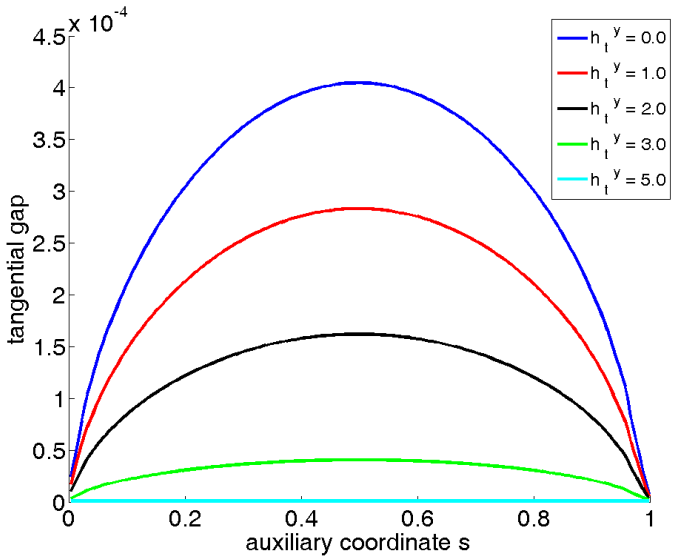

FIGURE 9.29: Comparison of the tangential gap along the auxiliary coordinate s for different yield tractions: The tangential gap decreases with an increasing yield traction.

9.3.4 Polycrystalline specimen under shear load

The classical J_2 flow theory for rate-independent plasticity uses the decomposition of the Cauchy stress tensor $\underline{\boldsymbol{\sigma}}$ into a *hydrostatic* and a *deviatoric* part [35]. The hydrostatic part represents the stress, that leads to a change in volume. The deviatoric part contains all shear contributions and is responsible for distortion. Experiments show, that plasticity in metals often occurs under a shear load. Hence, it suggests itself to investigate the behaviour of a polycrystalline material under shear loading. In order to derive the effective properties of heterogeneous materials, often homogenization techniques are applied. Several of these theories propose estimates for material properties for specimens with an infinite extension. They can be seen as asymptotic estimates. In opposite to the infinite extension of these techniques, one can also apply numerical simulations to samples of the microstructure. There, only a small specimen is modelled. The boundary conditions on these specimens have to be imposed properly, such that the macroscopic behavior is modelled correctly. Such boundary conditions are the *kinematic uniform boundary conditions*, described in [22] and references therein. Only a brief summary is given here: On the Dirichlet boundary, the displacement field $\underline{\boldsymbol{u}}$ is prescribed at each point $\underline{\boldsymbol{x}}$ such that

$$\underline{\boldsymbol{u}} = \underline{\boldsymbol{E}}\,\underline{\boldsymbol{x}} \qquad \forall \underline{\boldsymbol{x}} \in \Gamma_d \tag{9.14}$$

with the symmetric tensor $\underline{\boldsymbol{E}}$, representing a mean strain at the macroscopic scale. The local strain and stress tensors $\underline{\boldsymbol{\varepsilon}}$ and $\underline{\boldsymbol{\sigma}}$ may be different at every point $\underline{\boldsymbol{x}} \in \Omega$. They are homogenized, such that the strain and stress tensor on the macroscopic scale can be computed. A mean strain tensor is defined as:

$$\underline{\boldsymbol{E}} = \frac{1}{\int_\Omega \mathrm{d}\Omega} \int_\Omega \underline{\boldsymbol{\varepsilon}} \, \mathrm{d}\Omega \tag{9.15}$$

The mean stress is defined, accordingly:

$$\underline{\boldsymbol{\Sigma}} = \frac{1}{\int_\Omega \mathrm{d}\Omega} \int_\Omega \underline{\boldsymbol{\sigma}} \, \mathrm{d}\Omega \tag{9.16}$$

For a pure shear state, the strain tensor $\underline{\boldsymbol{E}}$, needed to impose the Dirichlet boundary conditions, is populated only in the secondary diagonal [22] with the follwoing values for this particular example:

$$\underline{\boldsymbol{E}} = \begin{bmatrix} 0 & 0.001 \\ 0.001 & 0 \end{bmatrix} \tag{9.17}$$

Here, a square domain with unit length is investigated. Two grain topologies are compared. First, the domain is divided into 15 grains, then into 50 grains. The grains are modelled by a Voronoi tessellation, whose "center" nodes are distributed randomly according to a uniform distribution as also done by [44]. A sketch of the domain as well as the two grain topologies with underlying meshes are depicted in figure 9.30. Following [43], a larger effect in the plastic regime is expected for more grains. The strength in the macroscopic response is expected to be less for 50 grains than for 15 grains. The domain is loaded with prescribed displacements, using the method of kineamtic uniform boundary conditions as described above. The use of (9.14) and (9.17) leads to the absolute value for the prescribed displacement on each boundary, $|g| = 0.0005$. The prescribed displacement is imposed within 100 equally sized load steps. Then, the boundary is forced into its initial position within 100 steps.

Remark 9.2. *It is possible to reduce the number of load steps to* 2×20 *and one will still get the same final results. However, the resolution of the evolution of the stick-slip-zone is finer with a higher number of load steps. Hence, more load steps are used in order to show the evolution of the stick-slip-zone quite accurately.*

Different structured meshes are used for both grain topologies. Their data are summarized

Number of grains	Mesh size h	Elements	Base DOFs	All DOFs	Cut elements
15	0.020203	2450	2592	3598	447
50	0.008838	12800	13122	17672	2061

TABLE 16: Data for structured meshes for two different grain topologies

Number of grains	normal penalty parameter	tangential penalty parameter
15	$1.0 \cdot 10^8$	$1.0 \cdot 10^7$
50	$1.0 \cdot 10^9$	$3.0 \cdot 10^7$

TABLE 17: Penalty parameters for both grain topologies

in table 16. The material properties are assumed to be constant in a grain, but different in each grain. The Young's modulus is distributed randomly in the range of $2.0 \cdot 10^5 \leq E^{(m)} \leq 2.2 \cdot 10^5$ using a uniform distribution. The Poisson's ratio is distributed in the range of $0.29 \leq \nu^{(m)} \leq 0.31$, respectively. The yield traction is chosen as $h_t^y = 50$. The problem is solved with the penalty method. The parameters are listed in table 17. In order to show the evolution of the stick-slip-zone during the loading and unloading, a series of contour plots is shown in figure 9.31 for the 15 grain topology. The same loadsteps are shown for the 50 grain topology in figure 9.32 The plots show the distribution of the shear stress, σ_{xy}. The grain boundaries are drawn. The coloring of the grain boundaries is done according to the same principle as explained in section 9.3.1: Subsegments in stick are colored blue, subsegments in slip are colored red. After reaching the maximal load in loadstep 100, the load is decreased. The decrease will result in elastic deformation at the beginning. Hence, the interfaces in loadstep 101 are mostly in stick. When plotting the mean shear stress, computed with (9.16), versus the imposed shear angle, γ, for both grain topologies, one can see the decrease in strength when plastic effects start working (see figure 9.33). In the elastic regime, the slope of both graphs represents the shear modulus, G. Assuming homogenized material properties with Young's modulus $E_{hom} = 210000$ and Poisson's ratio $\nu_{hom} = 0.3$, the homogenized shear modulus is computed to:

$$G_{hom} = \frac{E_{hom}}{2(1 + \nu_{hom})} \approx 80769 \tag{9.18}$$

For the 15 grain topology, the homogenized shear modulus can be extracted from the graph and takes the value $G_{15} \approx 79100$ whereas the one for the 50 grain topology is $G_{50} \approx 79180$. The slight deviations can be explained with the randomness in the material properties and by using a penalty method to enforce the constraints. Before plasticity starts in loadstep 32,

the stress increases linear with the slope of the shear modulus. As expected, one can see a weakening effect due to grain boundary sliding. This effect starts, when the shear stress reaches the value of the yield traction, $h_t^y = 50$. The weakening effect is greater for a greater number of grains.

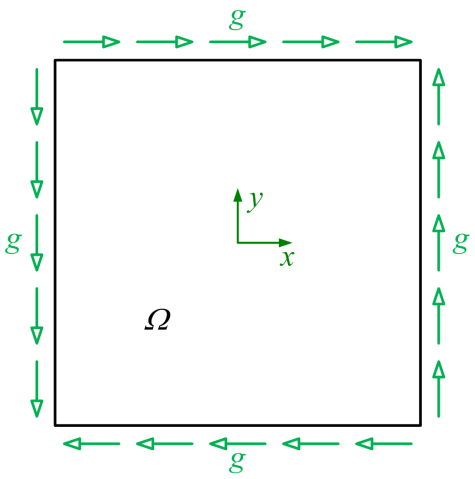

(a) Schematic of the domain using the concept of the *kinematic uniform boundary conditions*

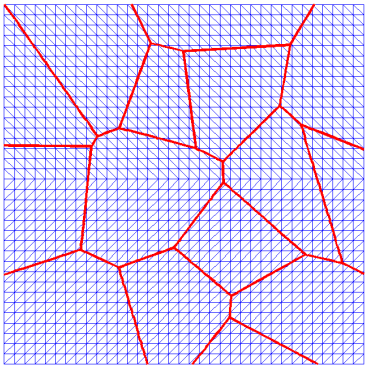

(b) 15 randomly distributed grains

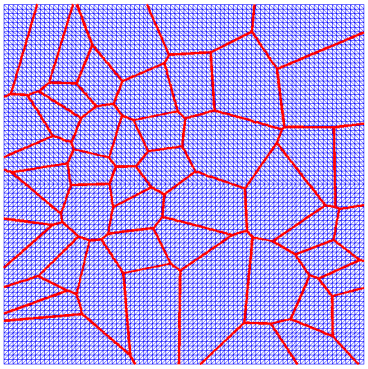

(c) 50 randomly distributed grains

FIGURE 9.30: Schematic of the domain and meshes with two different grain topologies

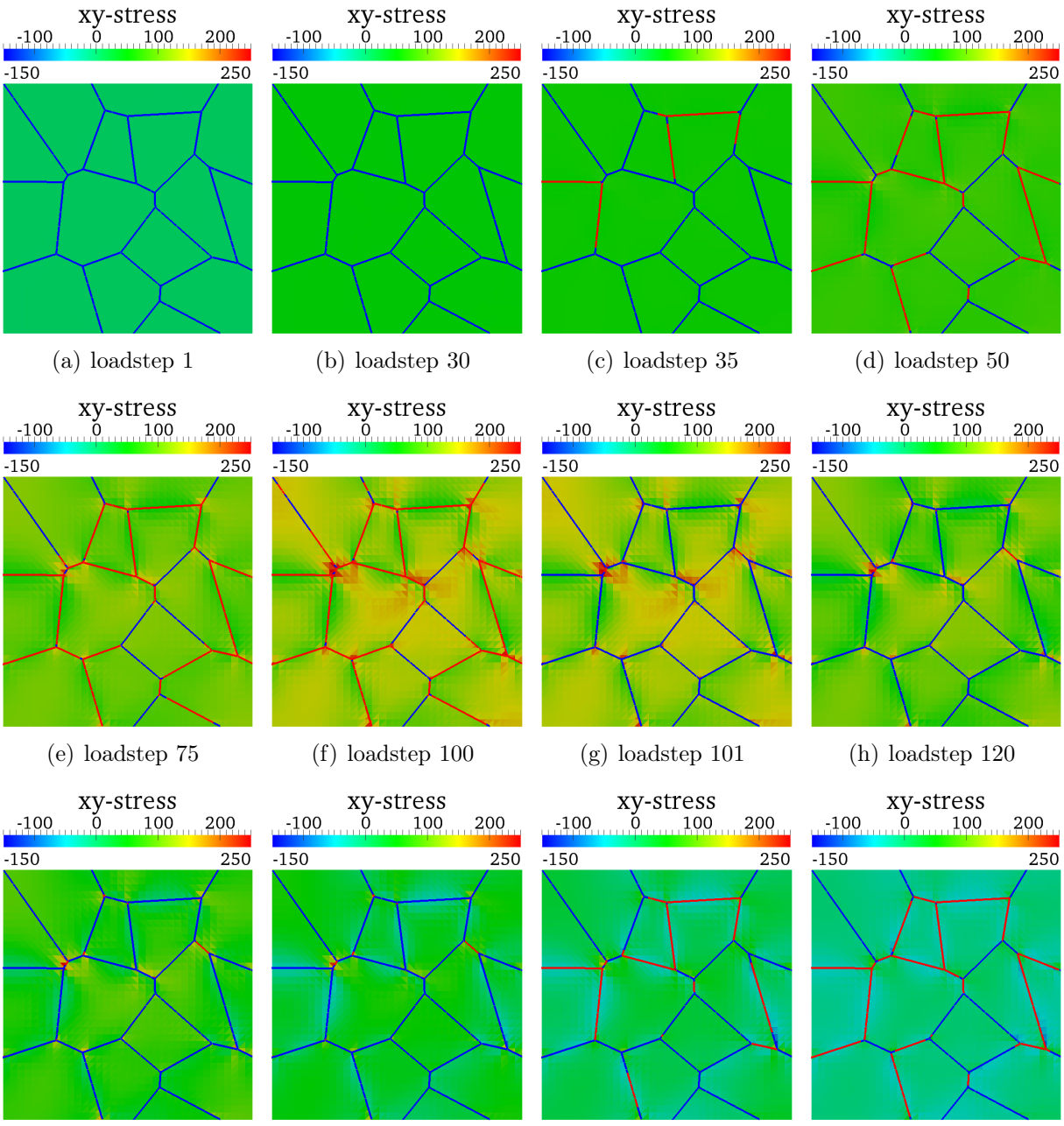

(a) loadstep 1 (b) loadstep 30 (c) loadstep 35 (d) loadstep 50

(e) loadstep 75 (f) loadstep 100 (g) loadstep 101 (h) loadstep 120

(i) loadstep 140 (j) loadstep 160 (k) loadstep 180 (l) loadstep 200

FIGURE 9.31: Shear stress σ_{xy} and evolution of the stick-slip-zone for the 15 grain topology

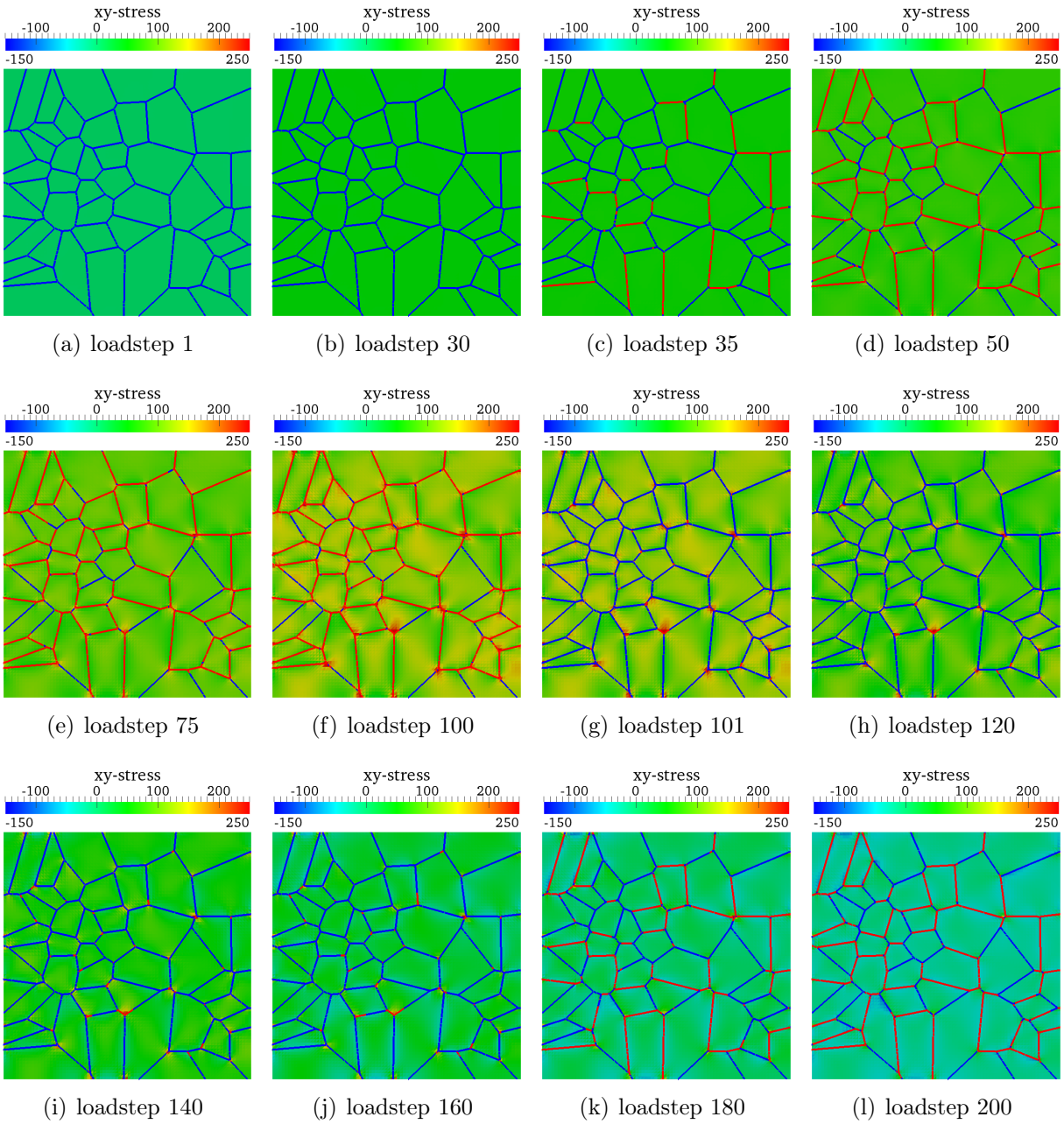

(a) loadstep 1 (b) loadstep 30 (c) loadstep 35 (d) loadstep 50

(e) loadstep 75 (f) loadstep 100 (g) loadstep 101 (h) loadstep 120

(i) loadstep 140 (j) loadstep 160 (k) loadstep 180 (l) loadstep 200

FIGURE 9.32: Shear stress σ_{xy} and evolution of the stick-slip-zone for the 50 grain topology

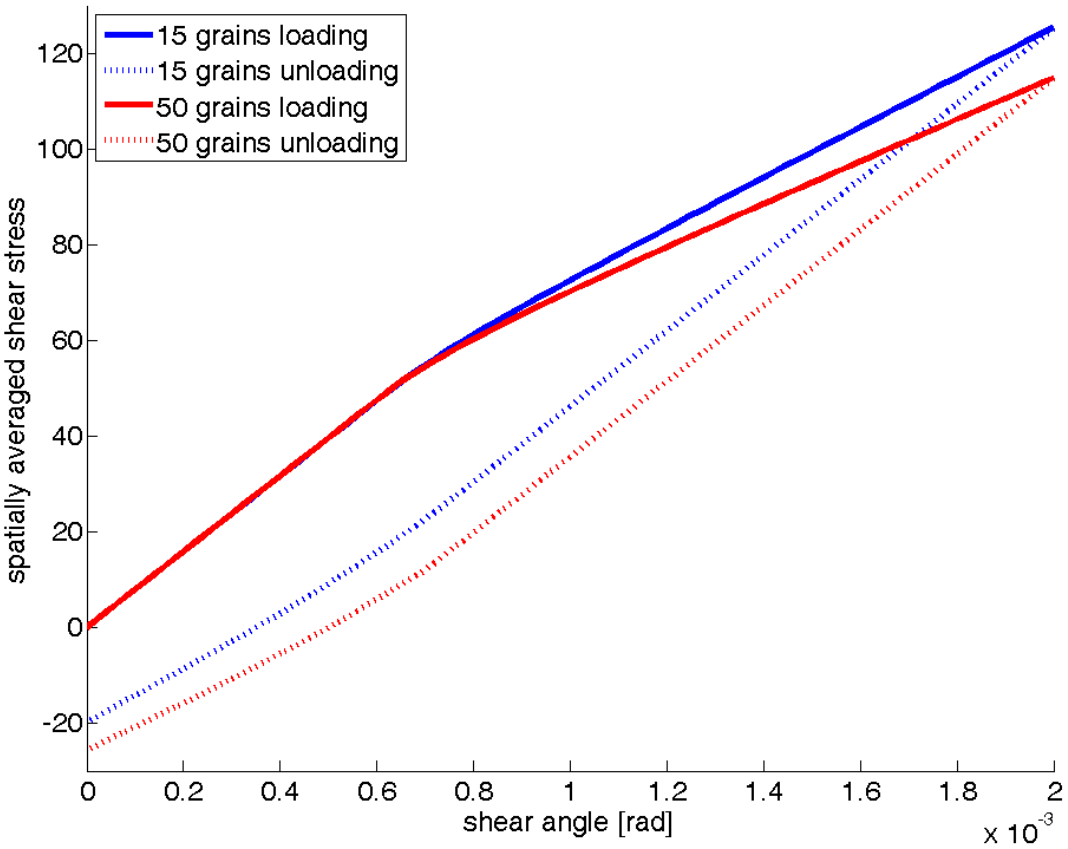

FIGURE 9.33: Mean shear stress Σ_{xy} versus the shear angle γ for both grain topologies. The weakening effect is larger for a higher number of grains. After removing the load, some stress remains since the system is irreversible. The loading curve is drawn as a solid line, the unloading curve as a dotted line.

10 Conclusion and outlook

In this work, various approaches to enforce interfacial constraints weakly over enriched interfaces are compared. The variational forms for each of the three methods were derived, namely: Lagrange multipliers, penalty method and Nitsche's method. Their effectiveness in representing frictionless as well as "frictional" sliding behavior was investigated. A stabilized Nitsche based method was developed to represent perfect plasticity at the interfaces. Each of the variational forms was discretized and expressions for residuals as required by a Newton-Raphson-scheme were presented. An estimate for the stabilization parameter, related to Nitsche's method, was derived. Some remarks on the extension of the approaches to more grains and some implementational and algorithmic details finish the theoretical part. Then, several numerical examples for frictionless sliding and perfect plasticity are presented. They show, that not only problems with two grains, but also polycrystalline examples can be solved. Optimal rates of convergence were observed in the bulk field as well as in the interfacial field with Nitsche based methods in the $\mathbb{L}_2$- and $\mathbb{H}_1$-norms. In contrast, Lagrange multipliers fail to converge and the penalty method converges at sub-optimal rates, considering the interfacial field. This illustrates the advantages of a Nitsche type approach.
Since the stabilized method for perfect plasticity at the interface leads to an unsymmetric formulation, one could be interested in a symmetrization. The inclusion of hardening effects into the plasticity model should be quite straight forward. A further generalization of the interfacial law could involve a traction-separation-law, such that a cohesive law in normal direction is included in order to enable the subdomains to separate from each other. Finally, the step from quasi-static simulations to dynamic simulations could be done. Some applications, like the faulted tectonic plates mentioned at the beginning, deal with large sliding at the interface, so that it is interesting to extend the formulations to a setting with large sliding.

A Alternative derivation of Nitsche's method

Following an approach in [21], an alternative derivation of Nitsche's method is provided which starts with a penalty formulation. The variational inconsistency in the penalty method is resolved and an additional term is added in order to obtain a symmetric formulation. For now, a simplified problem description is used, where body forces b_i are omitted. The equilibrium equation is given by:

$$\sigma_{ij,j}^{(m)} = 0 \text{ in } \Omega^{(m)} \tag{A.1}$$

The displacement field takes prescribed values on the Dirichlet boundary:

$$u_i^{(m)} = g_i^{(m)} \text{ on } \Gamma_d^{(m)} \tag{A.2}$$

On the Neumann boundary, external tractions are prescribed:

$$\sigma_{ij}^{(m)} n_j^{(m)} = h_i^{(m)} \text{ on } \Gamma_\sigma^{(m)} \tag{A.3}$$

The traction at the interface is approximated using a penalty regularization:

$$\sigma_{ij}^{(1)} n_j^{(1)} = -\sigma_{ij}^{(2)} n_j^{(2)} \approx -\frac{1}{\epsilon} [\![u_i]\!] \tag{A.4}$$

where the penalty parameter α is replaced by $1/\epsilon$ in order to show the variational inconsistency of the penalty method. Multiplying (A.1) with weighting functions, $w_i^{(m)}$, integration by parts and applying the divergence theorem results in:

$$\int_{\Omega^{(m)}} w_i^{(m)} \sigma_{ij,j} \, \mathrm{d}\Omega = \int_{\Gamma^{(m)}} w_i^{(m)} \sigma_{ij}^{(m)} n_j^{(m)} \, \mathrm{d}\Gamma - \int_{\Omega^{(m)}} w_{i,j}^{(m)} \sigma_{ij} \, \mathrm{d}\Omega \ , \ m \in \{1, 2\} \tag{A.5}$$

Applying a similar procedure to (A.4) yields:

$$\begin{aligned} \int_{\Gamma_*} w_i^{(1)} \sigma_{ij}^{(1)} n_j^{(1)} \, \mathrm{d}\Gamma &= -\frac{1}{\epsilon} \int_{\Gamma_*} w_i^{(1)} [\![u_i]\!] \, \mathrm{d}\Gamma \\ \int_{\Gamma_*} w_i^{(2)} \sigma_{ij}^{(2)} n_j^{(2)} \, \mathrm{d}\Gamma &= \ \ \frac{1}{\epsilon} \int_{\Gamma_*} w_i^{(2)} [\![u_i]\!] \, \mathrm{d}\Gamma \end{aligned} \tag{A.6}$$

Adding (A.5) and (A.6), splitting the boundary of a grain $\Gamma^{(m)}$ into its three parts $\Gamma_d^{(m)}$, $\Gamma_\sigma^{(m)}$ and Γ_* and using the fact, that the weighting function vanishes on the Dirichlet boundary, yields the weak form for the penalty method:

$$\sum_{m=1}^{2} \int_{\Omega^{(m)}} w_{i,j}^{(m)} \sigma_{ij}^{(m)} \,\mathrm{d}\Omega + \frac{1}{\epsilon} \int_{\Gamma_*} [\![w_i]\!] [\![u_i]\!] \,\mathrm{d}\Gamma = \sum_{m=1}^{2} \int_{\Gamma_\sigma^{(m)}} w_i^{(m)} h_i^{(m)} \,\mathrm{d}\Gamma \tag{A.7}$$

The constraint is satisfied perfectly only if $\epsilon \to 0$. In the limiting case, one would have to divide by zero, which is mathematically not admissible. The variational inconsistency of the penalty method can be seen clearly. To get a stabilized method, (A.6) is rescaled by dividing it by $\epsilon + \beta$. After adding these modified version to (A.5), the integral equation reads:

$$\begin{aligned} &\sum_{m=1}^{2} \int_{\Omega^{(m)}} w_{i,j}^{(m)} \sigma_{ij}^{(m)} \,\mathrm{d}\Omega - \frac{\beta}{\epsilon+\beta} \int_{\Gamma_*} w_i^{(1)} \sigma_{ij}^{(1)} n_j^{(1)} \,\mathrm{d}\Gamma - \frac{\beta}{\epsilon+\beta} \int_{\Gamma_*} w_i^{(2)} \sigma_{ij}^{(2)} n_j^{(2)} \,\mathrm{d}\Gamma \\ &+ \frac{1}{\epsilon+\beta} \int_{\Gamma_*} [\![w_i]\!] [\![u_i]\!] \,\mathrm{d}\Gamma = \sum_{m=1}^{2} \int_{\Gamma_\sigma^{(m)}} w_i^{(m)} h_i^{(m)} \,\mathrm{d}\Gamma \end{aligned} \tag{A.8}$$

Using the traction eqilibrium at the interface and the convention $n_j = n_j^{(1)} = -n_j^{(2)}$ from (2.7) leads to the defintion of the averaged stress $\langle \sigma_{ij} \rangle$, which is also defined in (4.29). Then (A.8) can be rewritten as:

$$\begin{aligned} &\sum_{m=1}^{2} \int_{\Omega^{(m)}} w_{i,j}^{(m)} \sigma_{ij}^{(m)} \,\mathrm{d}\Omega - \frac{\beta}{\epsilon+\beta} \int_{\Gamma_*} [\![w_i]\!] \langle \sigma_{ij} \rangle n_j \,\mathrm{d}\Gamma \\ &+ \frac{1}{\epsilon+\beta} \int_{\Gamma_*} [\![w_i]\!] [\![u_i]\!] \,\mathrm{d}\Gamma = \sum_{m=1}^{2} \int_{\Gamma_\sigma^{(m)}} w_i^{(m)} h_i^{(m)} \,\mathrm{d}\Gamma \end{aligned} \tag{A.9}$$

This weak form is not symmetric, which would result in an asymmetric stiffnes matrix. A term can be added on both sides of (A.9) in order to restore symmetry:

$$\begin{aligned} &\sum_{m=1}^{2} \int_{\Omega^{(m)}} w_{i,j}^{(m)} \sigma_{ij}^{(m)} \,\mathrm{d}\Omega - \frac{\beta}{\epsilon+\beta} \int_{\Gamma_*} [\![w_i]\!] \langle \sigma(\boldsymbol{u})_{ij} \rangle n_j \,\mathrm{d}\Gamma - \frac{\beta}{\epsilon+\beta} \int_{\Gamma_*} [\![u_i]\!] \langle \sigma(\boldsymbol{w})_{ij} \rangle n_j \,\mathrm{d}\Gamma \\ &+ \frac{1}{\epsilon+\beta} \int_{\Gamma_*} [\![w_i]\!] [\![u_i]\!] \,\mathrm{d}\Gamma = \sum_{m=1}^{2} \int_{\Gamma_\sigma^{(m)}} w_i^{(m)} h_i^{(m)} \,\mathrm{d}\Gamma + \frac{\epsilon\beta}{\epsilon+\beta} \int_{\Gamma_*} \langle \sigma(\boldsymbol{u})_{ij} \rangle n_j \langle \sigma(\boldsymbol{w})_{ij} \rangle n_j \,\mathrm{d}\Gamma \end{aligned} \tag{A.10}$$

In opposite to (A.7), this weak form is well defined also for $\epsilon \to 0$. Hence, it is capable of satisfying the continuity requirements at the interface perfectly. According to [21], Nitsche's

method can be obtained by setting $\epsilon = 0$:

$$\begin{aligned}&\sum_{m=1}^{2} \int_{\Omega^{(m)}} w_{i,j}^{(m)} \sigma_{ij}^{(m)} \,\mathrm{d}\Omega - \int_{\Gamma_*} [\![w_i]\!] \langle \sigma(\boldsymbol{u})_{ij} \rangle n_j \,\mathrm{d}\Gamma - \int_{\Gamma_*} [\![u_i]\!] \langle \sigma(\boldsymbol{w})_{ij} \rangle n_j \,\mathrm{d}\Gamma \\ &+ \frac{1}{\beta} \int_{\Gamma_*} [\![w_i]\!] [\![u_i]\!] \,\mathrm{d}\Gamma = \sum_{m=1}^{2} \int_{\Gamma_\sigma^{(m)}} w_i^{(m)} h_i^{(m)} \,\mathrm{d}\Gamma\end{aligned} \tag{A.11}$$

Replacing $1/\beta$ in the fourth term with the stabilization parameter α yields a formulation, that corresponds to the variational form (4.33) as well as the weak form, provided in [33]. Due to the second term, the weak form is consistent. The third term provides symmetry. The coercivity of the bilinear form is achieved by the stabilization term, if the stabilization paramter α is greater than a minimum value α_{min} [30]. Stability is also proved by [39] and some references therein. For some remarks on choosing the stabilization parameter, see section 4.3.3.

B A note on Young's inequality

The well-known Young's inequality [2] reads for the exponent 2:

$$ab \leq \frac{a^2}{2} + \frac{b^2}{2} \tag{B.1}$$

A modified form can be obtained by choosing:

$$a = \frac{c}{\sqrt{\epsilon}},\ b = \sqrt{\epsilon} d \qquad \forall \epsilon > 0 \tag{B.2}$$

Inserting (B.2) into the original form (B.1) yields *Young's inequality with* ϵ [2]:

$$cd \leq \frac{c^2}{2\epsilon} + \frac{\epsilon d^2}{2} \tag{B.3}$$

This can be used to rewrite the binomial $(c+d)^2$:

$$(c+d)^2 = c^2 + 2cd + d^2 \leq c^2 + \frac{c^2}{\epsilon} + \epsilon d^2 + d^2 = \left(1 + \frac{1}{\epsilon}\right) c^2 + (1+\epsilon) d^2 \tag{B.4}$$

So, an upper bound for the binomial $(c+d)^2$ can be estimated:

$$(c+d)^2 \leq \left(1 + \frac{1}{\epsilon}\right) c^2 + (1+\epsilon) d^2 \qquad \forall \epsilon > 0 \tag{B.5}$$

List of Notations

Notations

A_{ij}	tensor or matrix in index notation
$\boldsymbol{A}$	matrix
$\underline{\boldsymbol{A}}$	tensor
a_i	vector in index notation
$\boldsymbol{a}$	vector in vector notation
$\underline{\boldsymbol{a}}$	vector in tensor notation
$(\bullet)_{i,j}$	partial derivative $\partial(\bullet)_i/\partial x_j$
$\boldsymbol{a}^T\boldsymbol{b}$, $a_i b_i$	scalar product of vectors $\boldsymbol{a}$ and $\boldsymbol{b}$
$\boldsymbol{a}\boldsymbol{b}^T$, $a_i b_j$	dyadic product of vectors $\boldsymbol{a}$ and $\boldsymbol{b}$
$[\![\bullet]\!]$	jump or gap function
$\langle\bullet\rangle$	average operator
$\left\langle \cdot, \cdot \right\rangle$	integration along the interface
$(\cdot, \cdot)$	$\mathbb{L}_2$ inner product
$\lvert\boldsymbol{A}\rvert$	2-norm of matrix $\boldsymbol{A}$
$\lVert(\bullet)\rVert_{\mathbb{L}_2}$	$\mathbb{L}_2$-norm of $(\bullet)$
$\delta(\bullet)$	variation of $(\bullet)$
DOF	degree of freedom
$meas(\bullet)$	measure of $\bullet$
$\Delta(\bullet) = \frac{\partial(\bullet)}{\partial \boldsymbol{D}}\Delta\boldsymbol{D}$	shorthand notation for linearization of $(\bullet)$
$\boldsymbol{I}_{2\times2}$,$\delta_{ij}$	identity matrix
$(\bullet)^{trial}$	trial state
A	assembly operator

Superscripts

h	disretized quantity
(M),(I),(II),(III)	indices for interfaces
(m),(1),(2)	indices for grains
ref	reference quantity (analytical or with very fine mesh)

Parameters and indices

a	index over nodes of an element
C_I	configuration-dependent constant to estimate the stabilization parameter in a Nitsche context
c	real number to derive an estimate for the stabilization parameter
d	real number to derive an estimate for the stabilization parameter
e	index over elements
i	index
j	index, Newton-Raphson-step index
j_{max}	maximum number of Newton iterations
K	total number of load steps
k	index, load step index
l	index
t	projection onto tangential direction
tol_{dis}	tolerance for convergence check in the norm of the displacement increment
tol_{en}	tolerance for convergence check in the energy norm
tol_{res}	tolerance for convergence check in the norm of the residual
α, $\hat{\alpha}$	penalty parameter, stabilization parameter
α_n, $\hat{\alpha}$	penalty parameter, stabilization parameter for normal direction
α_t, $\hat{\alpha}$	penalty parameter, stabilization parameter for tangential direction
γ	absolute value of slip rate, consistency parameter
ϵ	real number to derive an estimate for the stabilization parameter
ξ	algorithmic consistency parameter

Physical field variables

$a(\boldsymbol{u}, \delta\boldsymbol{u})$	bilinear form for internal contributions
b_i	body forces
$\underline{\boldsymbol{C}}$,$C_{ijkl}$	constitutive tensor
$\underline{\boldsymbol{E}}$	homogenized mean strain tensor
E	Young's modulus
g_i	prescribed displacements on Dirichlet boundary

H	Heaviside function
h_i	prescribed tractions on Neumann boundary
$\underline{\boldsymbol{h}}^*$, h_i^*	traction field along the internal interface
h_t^y	yield traction for perfect plasticity in tangential direction
$l(\boldsymbol{u}, \delta\boldsymbol{u})$	linear form for external contributions
M	prescribed bending moment
$\underline{\boldsymbol{n}}$	normal vector of interface
$\underline{\boldsymbol{n}}^{(m)}$, $n_i^{(m)}$	normal vector of interface of grain m
$\underline{\boldsymbol{u}}$, $\boldsymbol{u}$, u_i	displacement field
$\hat{u}_i$	coarse displacement field
$\tilde{u}_i$	enrichments in displacement field
$\delta\underline{\boldsymbol{u}}$,$\delta u_i$	variation of displacement field
$\delta\hat{u}_i$	variation of coarse displacement field
$\delta\tilde{u}_i$	variation of enrichments in displacement field
$\underline{\boldsymbol{w}}$, w_i	test function of displacement field
$\hat{w}_i$	test function of coarse displacement field
$\tilde{w}_i$	test function of enrichments in displacement field
$\underline{\boldsymbol{x}}$, x_i	vector to a point in deformed configuration
$\underline{\boldsymbol{\varepsilon}}$, ε_{ij}	strain tensor
$\delta\underline{\boldsymbol{\varepsilon}}$, $\delta\varepsilon_{ij}$	variation of strain tensor
$\underline{\boldsymbol{\lambda}}$, λ_i	Lagrange multiplier field
ν	Poisson's ratio
Π	entire potential
Π^{AL}	augmented Lagrangian contribution to potential
Π^{ext}	potential of external forces
Π^{int}	internal potential
Π^{Lag}	potential of Lagrange multiplier field
Π^{Nit}	Nitsche contribution to potential
Π^{pen}	penalty contribution to potential
Π^{u}	contribution of the bulk field to potential
$\underline{\boldsymbol{\Sigma}}$	homogenized mean stress tensor
$\underline{\boldsymbol{\sigma}}$, σ_{ij}	Cauchy stress tensor
Φ	yield condition

Discrete quantities

$\hat{\boldsymbol{B}}$	matrix with spatial derivatives of shape functions in base degrees of freedom
$\tilde{\boldsymbol{B}}$	matrix with spatial derivatives of shape functions in enriched degrees of freedom
$cutnumele$	number of cut elements
$\boldsymbol{C}$,$\hat{\boldsymbol{C}}$,$\tilde{\boldsymbol{C}}^{(m)}$	discrete constitutive matrix
$\hat{\boldsymbol{c}}$	nodal value of weight function of displacements in base degrees of freedom
$\tilde{\boldsymbol{c}}$	nodal value of weight function of displacements in first set of enriched degrees of freedom
$\boldsymbol{D}$	global displacement vector
$\Delta\boldsymbol{D}$	global displacement increment in Newton-Raphson-scheme
$\delta\boldsymbol{D}$	global displacement increment in load stepping scheme
$\boldsymbol{d}$, d_i	nodal displacements in an element
$\hat{\boldsymbol{d}}$	nodal displacements in base degrees of freedom
$\tilde{\boldsymbol{d}}$	nodal displacements in first set of enriched degrees of freedom
$\tilde{\tilde{\boldsymbol{d}}}$	nodal displacements in second set of enriched degrees of freedom
$enrnumele$	number of enriched elements in entire discretization
$\boldsymbol{G}$	global stiffnes contribution for Lagrange multipliers
$\boldsymbol{g}^{d,(e)}$,$\boldsymbol{g}^{\lambda,(e)}$	elemental stiffnes contribution for Lagrange multipliers
$\boldsymbol{K}$	global tangent stiffness matrix
$\boldsymbol{K}^{u}$	contributions of bulk field to global stiffness matrix
$\boldsymbol{K}^{Nit}$	Nitsche contributions to global stiffness matrix
$\boldsymbol{K}^{pen}$	penalty contributions to global stiffness matrix
$\boldsymbol{k}^{u,(e)}$	contributions of bulk field to element stiffness matrix
$\boldsymbol{k}^{Nit,(e)}$	Nitsche contributions to element stiffness matrix
$\boldsymbol{k}^{pen,(e)}$	penalty contributions to element stiffness matrix
N_a	shape function at a node
$\hat{\boldsymbol{N}}$	shape function matrices for base degrees of freedom
$\tilde{\boldsymbol{N}}$	shape function matrices for first set of enriched degrees of freedom

$\tilde{\tilde{\boldsymbol{N}}}$	shape function matrices for second set of enriched degrees of freedom
nodes	number of nodes per element
numele	number of elements in entire discretization
$\boldsymbol{R}$	global residual
$\boldsymbol{R}^{u}$	global residual for untied problem
$\boldsymbol{R}^{Lag}$	contribution to global residual due to Lagrange multipliers
$\boldsymbol{R}^{Nit}$	contribution to global residual due to Nitsche's method
$\boldsymbol{R}^{pen}$	contribution to global residual due to penalty method
$\boldsymbol{r}^{u,(e)}$	element residual for untied problem
$\boldsymbol{r}_{b}^{u,(e)}$	element residual due to the bulk field
$\boldsymbol{r}_{f}^{u,(e)}$	element residual due to body forces
$\boldsymbol{r}_{\sigma}^{u,(e)}$	element residual due to external tractions
$\boldsymbol{r}^{Lag,(e)}$	contribution to element residual due to Lagrange mulitpliers
$\boldsymbol{r}^{Nit,(e)}$	contribution to element residual due to Nitsche's method
$\boldsymbol{r}^{pen,(e)}$	contribution to element residual due to penalty method
$\boldsymbol{r}^{stab,(e)}$	contribution to element residual due to stabilized method
$\boldsymbol{\varepsilon}$, $\boldsymbol{\varepsilon}^{h}$	strain tensor in Voigt notation
$\delta\boldsymbol{\varepsilon}$, $\delta\boldsymbol{\varepsilon}^{h}$	variation of strain tensor in Voigt notation
$\boldsymbol{\kappa}_{ij}^{Nit,(e)}$	submatrices for Nitsche element stiffness matrix
$\boldsymbol{\kappa}_{22}^{pen,(e)}$	submatrix for penalty element stiffness matrix
$\boldsymbol{\kappa}_{ij}^{u,(e)}$	submatrices for bulk element stiffness matrix
$\bar{\boldsymbol{\lambda}}$	discrete Lagrange multiplier
$\delta\bar{\boldsymbol{\lambda}}$	variation of discrete Lagrange multiplier
$\boldsymbol{\sigma}$, $\boldsymbol{\sigma}^{h}$	stress tensor in Voigt notation

Geometric entities

$A^{(m)}$	area of part of element overlapping with grain m
h	height
L_s	length of subsegment of interface
l	length
numint	number of interfaces in the entire domain
x	x-coordinate
y	y-coordinate

Γ_{ext}	boundary of the domain Ω
$\Gamma^{(m)}$	boundary of a grain
Γ_d,$\Gamma_d^{(m)}$	Dirichlet boundary
Γ_σ,$\Gamma_\sigma^{(m)}$	Neumann boundary
Γ_*, $\Gamma_*^{(M)}$	internal boundary or embedded interface
$\Gamma_*^{(e)}$	subsegment of internal boundary or embedded interface
Ω	entire domain
$\Omega^{(e)}$	element domain
$\Omega^{(m)}$, $\Omega^{(1)}$, $\Omega^{(2)}$	grains as parts of entire domain

References

[1] D. N. Arnold, F. Brezzi, B. Cockburn, and L. D. Marini. Unified analysis of discontinuous galerkin methods for elliptic problems. *SIAM Journal on Numerical Analysis*, 39(5):1749–1779, 2002.

[2] K. E. Atkinson and W. Han. *Theoretical Numerical Analysis – A Functional Analysis Framework*, volume 39 of *Texts in Applied Mathematics*. Springer, 3rd edition, 2009.

[3] I. Babuška. The Finite Element Method with Lagrangian Multipliers. *Numerische Mathematik*, 20(3):179–192, 1973.

[4] I. Babuška. The Finite Element Method with Penalty. *Mathematics of Computation*, 27(122):221–228, 1973.

[5] E. Béchet, M. Nicolas, and B. Wohlmuth. A stable Lagrange multiplier space for stiff interface conditions within the extended finite element method. *International Journal for Numerical Methods in Engineering*, 78(8):931–954, 2009.

[6] T. Belytschko, W. K. Liu, and B. Moran. *Nonlinear Finite Elements for Continua and Structures*. John Wiley & Sons Ltd., 2000.

[7] M. A. Crisfield. Re-visiting the contact patch test. *International Journal for Numerical Methods in Engineering*, 48(3):435–449, 2000.

[8] J. Dolbow and I. Harari. An efficient finite element method for embedded interface problems. *International Journal for Numerical Methods in Engineering*, 78(2):229–252, 2009.

[9] J. Dolbow, N. Moës, and T. Belytschko. Discontinuous enrichment in finite elements with a partition of unity method. *Finite Elements in Analysis and Design*, 36(3–4):235–260, 2000.

[10] J. Dolbow, N. Moës, and T. Belytschko. An extended finite element method for modeling crack growth with frictional contact. *Computer Methods in Applied Mechanics and Engineering*, 190(51–52):6825–6846, 2001.

[11] J. E. Dolbow and L. P. Franca. Residual-free bubbles for embedded Dirichlet problems. *Computer Methods In Applied Mechanics And Engineering*, 197(45–48):3751–3759, 2008.

[12] C. A. Duarte, I. Babuška, and J. T. Oden. Generalized finite element methods for three-dimensional structural mechanics problems. *Computers and Structures*, 77(2):215–232, 2000.

[13] A. Embar, J. Dolbow, and I. Harari. Imposing Dirichlet boundary conditions with Nitsche's method and spline-based finite elements. *International Journal for Numerical Methods in Engineering*, 83(7):877–898, 2010.

[14] S. Fernández-Méndez and A. Huerta. Imposing essential boundary conditions in mesh-free methods. *Computer methods in applied mechanics and engineering*, 193(12–14):1257–1275, 2004.

[15] C. Geuzaine and J. F. Remacle. Gmsh: a three-dimensional finite element mesh generator with built-in pre- and post-processing facilities. *International Journal for Numerical Methods in Engineering*, 79(11):1309–1331, 2009.

[16] F. Ghahremani. Effect of grain boundary sliding on anelasticity of polycrystals. *International Journal of Solids and Structures*, 16(9):825–845, 1980.

[17] A. Hansbo, P. Hansbo, and M. G. Larson. A finite element method on composite grids based on Nitsche's method. *ESAIM: Mathematical Modelling and Numerical Analysis*, 37(3):495–514, 2003.

[18] I. Harari and J. Dolbow. Analysis of an efficient finite element method for embedded interface problems. *Computational Mechanics*, 46(1):205–211, 2010.

[19] T. J. R. Hughes. *The Finite Element Method – Linear Static and Dynamic Finite Element Analysis*. Dover Publications, Inc., Mineola, New York, 2000.

[20] H. Ji and J. E. Dolbow. On strategies for enforcing interfacial constraints and evaluating jump conditions with the extended finite element method. *International Journal for Numerical Methods in Engineering*, 61(14):2508–2535, 2004.

[21] M. Juntunen and R. Stenberg. Nitsche's method for general boundary conditions. *Mathematics of Computation*, 78(267):1353–1374, 2009.

[22] T. Kanit, S. Forest, I. Galliet, V. Mounoury, and D. Jeulin. Determination of the size of the representative volume element for random composites: statistical and numerical approach. *International Journal of Solids and Structures*, 40(13–14):3647–3679, 2003.

[23] T. A. Laursen. *Computational Contact and Impact Mechanics – Fundamentals of Modeling Interfacial Phenomena in Nonlinear Finite Element Analysis*. Springer, Berlin, 2002.

[24] Laursen, Tod A. *Formulation And Treatment Of Frictional Contact Problems Using Finite Elements*. PhD thesis, Department Of Mechanical Engineering, Stanford University, July 1992.

[25] M. A. Meyers, A. Mishra, and D. J. Benson. Mechanical properties of nanocrystalline materials. *Progress in Materials Science*, 51(4):427–556, 2006.

[26] R. L. Michalowski and Z. Mróz. Associated and non-associated sliding rules in contact friction problems. *Archives of Mechanics*, 30(3):259–276, 1978.

[27] N. Moës, E. Béchet, and M. Tourbier. Imposing Dirichlet boundary conditions in the extended finite element method. *International Journal for Numerical Methods in Engineering*, 67(12):1641–1669, 2006.

[28] N. Moës, J. Dolbow, and T. Belytschko. A finite element method for crack growth without remeshing. *International Journal for Numerical Methods in Engineering*, 46(1):131–150, 1999.

[29] H. M. Mourad, J. Dolbow, and I. Harari. A bubble-stabilized finite element method for Dirichlet constraints on embedded interfaces. *International Journal for Numerical Methods in Engineering*, 69(4):772–793, 2007.

[30] J. Nitsche. Über ein Variationsprinzip zur Lösung von Dirichlet-Problemen bei Verwendung von Teilräumen, die keinen Randbedingungen unterworfen sind. *Abhandlungen aus dem Mathematischen Seminar der Universität Hamburg*, 36(1):9–15, 1971.

[31] J. M. Ortega. *Matrix Theory – A second Course*. Plenum Press, 1987.

[32] R. Raj and M. F. Ashby. Intergranular fracture at elevated temperature. *Acta Metallurgica*, 23(6):653–666, 1975.

[33] J. D. Sanders, J. E. Dolbow, and T. A. Laursen. On methods for stabilizing constraints over enriched interfaces in elasticity. *International Journal for Numerical Methods in Engineering*, 78(9):1009–1036, 2009.

[34] M. Siavelis, M. L. E. Guiton, P. Massin, and N. Moës. 3D X-FEM of frictional fault networks with large sliding and nonlinear kinematics. presentation at ECCM, Paris, 2010.

[35] J. C. Simo and T. J. R. Hughes. *Computational Inelasticity*, volume 7 of *Interdisciplinary Applied Mathematics*. Springer, New York, 1998.

[36] J. C. Simo and T. A. Laursen. An augmented Lagrangian treatment of contact problems involving friction. *Computers & Structures*, 42(1):97–116, 1992.

[37] A. Simone. Partition of unity-based discontinuous elements for interface phenomena: computational issues. *Communications in Numerical Methods in Engineering*, 20(6):465–478, 2004.

[38] A. Simone, C. A. Duarte, and E. Van der Giessen. A Generalized Finite Element Method for polycrystals with discontinuous grain boundaries. *International Journal for Numerical Methods in Engineering*, 67(8):1122–1145, 2006.

[39] R. Stenberg. On some techniques for approximating boundary conditions in the finite element method. *Journal of Computational and Applied Mathematics*, 63(1–3):139–148, 1995.

[40] S. P. Timoshenko and J. N. Goodier. *Theory of Elasticity*. McGraw-Hill, New York, 3rd edition, 1970.

[41] M. M. Vainberg. *Variational Methods for the Study of Nonlinear Operators*. Holden-Day, San Francisco, CA, 1964.

[42] E. van der Giessen. Interaction of cavitating grain boundary facets in creeping polycrystals. *Mechanics of Materials*, 17(1):47–69, 1994.

[43] H. Van Swygenhoven, M. Spaczer, A. Caro, and D. Farkas. Competing plastic deformation mechanisms in nanophase metals. *Physical Review B*, 60(1):22–25, 1999.

[44] Y. J. Wei and L. Anand. Grain-boundary sliding and separation in polycrystalline metals: application to nanocrystalline fcc metals. *Journal of the Mechanics and Physics of Solids*, 52(11):2587–2616, 2004.

[45] P. Wriggers. *Computational Contact Mechanics*. Springer, Berlin, 2nd edition, 2006.

[46] P. Wriggers and G. Zavarise. A formulation for frictionless contact problems using a weak form introduced by Nitsche. *Computational Mechanics*, 41(3):407–420, 2008.

[47] C. Zener. Theory of the Elasticity of Polycrystals with Viscous Grain Boundaries. *Physical Review*, 60(12):906–908, 1941.

[48] O. C. Zienkiewicz and R. L. Taylor. *The Finite Element Method – The Basis*, volume 1. Butterworth-Heinemann, Oxford, 5th edition, 2000.

Declaration of own work

Hiermit versichere ich, die vorliegende Diplomarbeit selbständig und unter ausschließlicher Verwendung der angegebenen Quellen und Hilfsmittel verfasst zu haben.

(Ort, Datum) (Unterschrift)